VILNIUS UNIVERSITY

CENTRE FOR PHYSICAL SCIENCES AND TECHNOLOGY

INSTITUTE OF CHEMISTRY

Artūras Katelnikovas

SYNTHESIS AND CHARACTERIZATION OF LUMINESCENT MATERIALS FOR SOLID STATE LIGHT SOURCES

Doctoral Dissertation

Physical Sciences, Chemistry (03 P)

Vilnius, 2012

The dissertation was carried out in Vilnius University and Münster University of Applied Sciences in the period 2008-2012.

Scientific supervisor:

Prof. Habil. Dr. Aivaras Kareiva

(Vilnius University, Physical Sciences, Chemistry 03P)

Scientific consultant:

Prof. Dr. Thomas Jüstel

(Münster University of Applied Sciences, Physical Sciences, Chemistry 03P)

Contents

List of Abbreviations:

BBL	Black Body Locus
CCT	Correlated Colour Temperature
CIE	Commission Internationale de l’Eclairage
CRI	Colour Rendering Index
CT	Charge Transfer
DTA	Differential Thermal Analysis
DTG	Differential Thermogravimetry
ED	Electric Dipole
EQ	Electric Quadrupole
LE	Luminous Efficacy
LED	Light Emitting Diode
LuAG:Ce	$Lu_3Al_5O_{12}:Ce^{3+}$
MD	Magnetic Dipole
NTSC	National Television Standard Committee
pcLED	phosphor converted Light Emitting Diode
PL	Photoluminescence
QE	Quantum Efficiency
RT	Room Temperature
TG	Thermogravimetry
THMAM	Tris-(hydroxymethyl)-aminomethane
TQ	Thermal Quenching
UV/VIS	Ultraviolet/Visible
VUV	Vacuum Ultraviolet
XRD	X-ray Diffraction
YAG:Ce	$Y_3Al_5O_{12}:Ce^{3+}$

Chapter 1. Introduction

Today we are on the bridge to the age of solid state lighting. The modern society relies heavily on mankind's ability to produce light. The first artificial light sources used to lengthen the day dates back thousands of years. An ancient mankind created light by burning wood. Even though this is rather inefficient way, the produced heat also enabled our predecessors to cook their food, develop metal tools and repel wild animals from their home [1, 2].

The evolution of light sources can be divided into the four parts [3, 4]. The first revolution is everything that is related with open fire, i.e. burning of wood, kerosene, candles, etc. This is rather inefficient way since only a small part of energy is converted into the light and the rest is dissipated as heat. However, this was the longest period when such light sources were used. On the other hand, burning wood or kerosene is still the only way to produce artificial light in many developing countries where electricity is in a short supply [5, 6]. The second generation of light sources has started when the incandescent light bulb was discovered by T. A. Edison in 1879 [7]. The era of incandescent light bulb dates till now, however, it seems that quite soon it might be over, since the EU, USA and Australia decided to ban them in the nearest future in order to save electrical power [8]. The third revolution of light sources began with the introduction of fluorescent tubes by General Electrics (GE) in 1939 [9] (even though the patent was filled by Meyer et al. already in 1927 [10]). It employs the UV radiation emitted by the low pressure mercury plasma to excite the phosphor layer inside of the tube. The fluorescent tubes at present are the most efficient white light sources for general lighting applications [2]. The fourth evolution of light sources starts with the invention of the blue emitting InGaN-based LED by S. Nakamura in 1991 [11]. With years the scientists were able to produce more and more efficient blue LEDs [12-14], which became the basis for white LEDs [15-18]. In other words, the invention of blue LED has started the era of solid state lighting. The white LEDs inevitably will replace incandescent light bulbs and, with enough time, the fluorescent tubes. Moreover, white LEDs are already a dominant technology for backlighting units of LCD displays in mobile phones, handled devices, computer monitors, and TVs [19].

With increasing efficiency of the blue LEDs the new luminescent materials that are able to convert blue light to the green, yellow, orange and red became necessary in order to obtain white light. The first phosphor that was combined with blue-emitting LED to produce white light was YAG:Ce, which was originally developed for flying-spot cathode-ray tubes [20]. However, due to deficiency of intensity in the red spectral region, such white LED possessed low CRI values (poor colour reproducibility) and high CCTs, thus the generated white light looked bluish. Nevertheless, people are used to incandescent bulbs generating the yellowish white light, which creates the pleasant and cosy atmosphere. Therefore, the intensity in the red spectral region needs to be increased to meet the requirements for general illumination. Furthermore, the near-UV LED based white light sources recently emerged as an alternative to the blue ones. The advantage of near-UV LED is that there are much more phosphors that can be excited in near-UV than in the blue spectral region. Thus the "construction" of white light should be relatively easier task. On the other hand, the near-UV LEDs are not that efficient yet, but the progress in efficiency enhancement is significant and even deep UV LEDs recently were reported [21-25].

The motivation of this work was to find new and efficient inorganic phosphors that could be applied in near-UV or blue LED based solid state white light sources. Therefore, the tasks of the present thesis were formulated as follows:

1. Synthesis and investigation of PL properties of $Ba_2(Zr,Hf)_2Si_3O_{12}$ doped with Eu^{2+}.
2. Synthesis and investigation of PL properties of Eu^{3+} substituted $Li_3Ba_2La_3(MoO_4)_8$.
3. Synthesis and investigation of PL properties of $(Y,Lu)_3Al_3MgSiO_{12}$ doped with Ce^{3+}.

4. Synthesis and investigation of PL properties of $CaLu_2Al_4SiO_{12}$ doped with Ce^{3+}.
5. Synthesis and investigation of PL properties of $CaY_2Al_4SiO_{12}$ doped with Ce^{3+}.

Statements for defence:

1) $Ba_{2-x}Eu_x(Zr,Hf)_2Si_3O_{12}$ phosphor powders can be prepared by the solid-state synthesis route employing some boric acid as a flux. It was shown that single phase compounds can be obtained with any Zr/Hf ratio. Upon UV excitation phosphors shows blue emission which is attributed to the $[Xe]4f^65d^1 \rightarrow [Xe]4f^7$ transition of Eu^{2+} ion. An energy transfer from zirconyl groups to Eu^{2+} is observed. The emission maximum of Eu^{2+} shifts towards shorter wavelengths if Zr is substituted by Hf. The photoluminescence decay times become shorter following the same trend. This can be explained by higher transition probability for blue shifted emission.
2) Red emitting $Li_3Ba_2La_{3-x}Eu_x(MoO_4)_8$ photoluminescent materials can be synthesized by a solid-state reaction method at 800 °C for 10 h in air. Measurements revealed that phosphors doped with 70, 80, and 90% of Eu^{3+} possess close to 100% QE if excited at 465 nm. Moreover, the prepared phosphors show little TQ and high colour saturation.
3) Green-orange emitting $(Y,Lu)_3Al_3MgSiO_{12}$ phosphors doped with Ce^{3+} can be synthesized by sol-gel synthesis route employing ethylene glycol as complexing agent. It has been observed that emission maximum of Ce^{3+} ions shifts towards blue spectral region if Y^{3+} is substituted by Lu^{3+}, this is explained by the reduced crystal field strength onto dodecahedral site in the garnet crystal structure.
4) Green-emitting $CaLu_2Al_4SiO_{12}$ garnet powders doped with Ce^{3+} can be synthesized by sol-gel combustion method employing THMAM as both complexing agent and fuel. The emission maximum of Ce^{3+} is blue shifted in comparison to conventional LuAG:Ce. The blue shift of its

emission maximum can be explained by the weaker crystal field strength due to lower effective charge of dodecahedral garnet site caused by substitution of trivalent lutetium by divalent calcium.

5) Yellow-emitting $CaY_2Al_4SiO_{12}$ garnet powders doped with Ce^{3+} can be prepared by sol-gel combustion method employing THMAM as both complexing agent and fuel. The emission maxima of Ce^{3+} is blue shifted if compared with conventional YAG:Ce. This can be explained by the weaker crystal field strength due to the lower effective charge of the dodecahedral garnet site caused by substitution of trivalent yttrium by divalent calcium. Moreover, the shift of emission to the shorter wavelength range is observed if samples are excited upon higher energy photons (shorter wavelength).

Chapter 2. Solid State White Light Sources

2.1. Via Blue LED Chip

There are several ways to produce white light employing blue-emitting LED. The most simple one is applying solely a yellow emitting phosphor, like YAG:Ce, on top of LED chip [26-29]. However, this approach results in rather high CCTs and low CRI values (R_a) due to the lack of intensity in the red spectral region. The CRI defines the ability of a light source to illuminate an object and how its illumination makes the colour appear to the human eye compared to the sun (for 6500 “D65” and 5000 K “D50”) or to black body radiators (for 4200, 3450, 2950, 2700 K) as a light source. The CRI of the sunlight is defined as 100 [2]. Another way is to combine either yellow and red, or green and red phosphors with blue LED. The two phosphor LEDs are superior against single phosphor LEDs, because the CCT and CRI values can be adjusted according to the requirements in different application areas, i.e. in street lighting CRI is not important, however, in museums, for instance, the CRI values should be close or equal to 100 for the best colour reproducibility. The graphical illustration of these three different ways of generating white light is given in *Figure 2.1*.

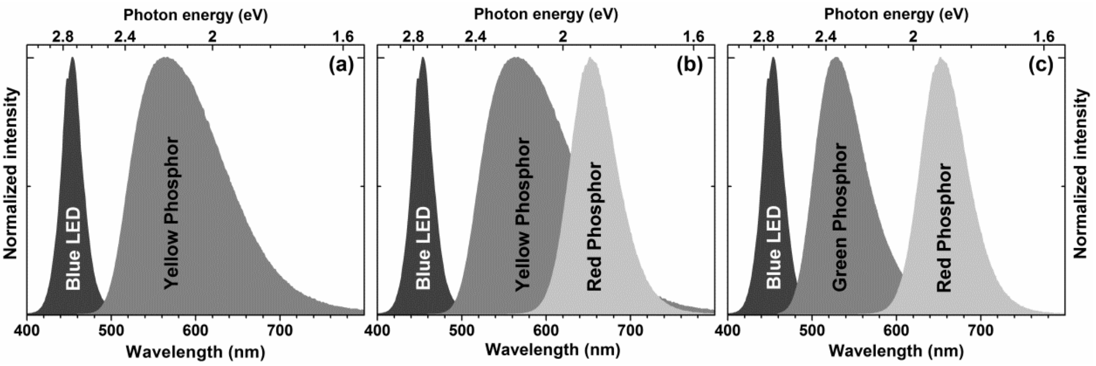

Figure 2.1 *Normalized emission spectra of pcLEDs: (a) blue/yellow, (b) blue/yellow/red, and (c) blue/green/red.*

With the increasing demand for the warm white LEDs the need of materials, that are able to down-convert the blue light to the cyan, green, yellow, orange, and red, arose. However, such materials need to meet quite high requirements in order to be applied in white LEDs. Such requirements are [30]:

1. An emission spectrum, which in combination with the emission of the other components (LED, other phosphors), leads to a pure white emission with a specific colour rendering and colour temperature.
2. Strong absorption overlapping with the emission spectra of pumping LED.
3. High thermal quenching temperatures.
4. High quantum efficiency.
5. Excellent chemical and thermal stability.
6. Absence of emission saturation at high fluxes.

A short overview of some recently developed phosphors for blue-chip based LEDs is given in *Table 2.1*.

***Table 2.1** Characteristics of some recently reported phosphors for blue-LED based pcLEDs [30-32].*

Phosphor	**Emission colour**	**Em$_{max}$ (nm)**	**CIE 1931 (x, y)**	**Problem areas**	**Ref.**
$BaSi_2O_2N_2:Eu^{2+}$	Cyan	495	(0.076; 0.440)	Synthesis	[33]
$BaGa_2S_4:Eu^{2+}$	Green	504	(0.143; 0.506)	Synthesis, TQ	[34]
$Ba_2SiO_4:Eu^{2+}$	Green	505	(0.240; 0.626)	Stability	[35]
$Ca_3Sc_2Si_3O_{12}:Ce^{3+}$	Green	507	(0.310; 0.590)	Narrow aborption band	[36]
$CaAl_2S_4:Eu^{2+}$	Green	516	-	Synthesis, stability	[37]
$CaLu_2Al_4SiO_{12}:Ce^{3+}$	Green	524	(0.329; 0.558)	Narrow aborption band	[38]
$Ba_3Si_6O_{12}N_2:Eu^{2+}$	Green	527	(0.310; 0.625)	Synthesis	[39]
$SrGa_2S_4:Eu^{2+}$	Green	535	(0.270; 0.690)	Synthesis, TQ	[34]
$BaYSi_4N_7:Eu^{2+}$	Green	537	-	Synthesis	[40]
$SrSi_2O_2N_2:Eu^{2+}$	Green	538	(0.337; 0.619)	Synthesis	[33]
$Lu_3Al_5O_{12}:Ce^{3+}$	Green	540	(0.350; 0.575)	Narrow aborption band	[38]
$ZnGa_2S_4:Eu^{2+}$	Green	540	(0.299; 0.673)	Synthesis, TQ	[34]
Ca-α-SiAlON:Yb^{2+}	Green	545	(0.323; 0.601)	Synthesis	[41]
$SrYSi_4N_7:Eu^{2+}$	Green	550	-	Synthesis	[42]
$CaLaGa_3S_7:Eu^{2+}$	Yellow	554	(0.390; 0.580)	Synthesis, TQ	[43]
$Lu_3Al_3MgSiO_{12}:Ce^{3+}$	Yellow	555	(0.429; 0.538)	TQ	[44]
$CaSi_2O_2N_2:Eu^{2+}$	Yellow	555	(0.419; 0.556)	Synthesis	[33]
$Y_3Al_5O_{12}:Ce^{3+}$	Yellow	556	(0.458; 0.530)	Narrow aborption band	[45]
$CaGa_2S_4:Eu^{2+}$	Green	558	(0.410; 0.580)	Synthesis, TQ	[34]
$SrLi_2SiO_4:Eu^{2+}$	Yellow	562	(0.368; 0.515)	Stability	[46]
$Tb_3Al_5O_{12}:Ce^{3+}$	Yellow	562	(0.482; 0.511)	Narrow aborption	[45]

				band, TQ	
$Gd_3Al_5O_{12}$:Ce^{3+}	Yellow	565	(0.496; 0.497)	Narrow aborption band, TQ	[45]
Ca_2BO_3Cl:Eu^{2+}	Yellow	570	(0.493; 0.496)	Stability	[47]
Sr_3SiO_5:Eu^{2+}	Yellow	570	-	Stability	[48]
$Ba_2Si_5N_8$:Eu^{2+}	Yellow	572	(0.521; 0.472)	Synthesis	[49]
	Red	650	(0.668; 0.327)		
$GdSr_2AlO_5$:Ce^{3+}	Yellow	574	(0.475; 0.502)	Efficiency	[50]
$Y_3Al_3MgSiO_{12}$:Ce^{3+}	Yellow	575	(0.488; 0.499)	TQ	[44]
$CaAlSiN_3$:Ce^{3+}	Orange	580	-	Synthesis	[51]
$Ba_2AlSi_5N_9$:Eu^{2+}	Orange	584	-	Synthesis	[52]
$Y_3Mg_2AlSi_2O_{12}$:Ce^{3+}	Orange	600	(0.542; 0.452)	TQ, efficiency	[53]
Ca-α-SiAlON:Eu^{2+}	Orange	603	(0.560; 0.436)	Synthesis	[54]
$Ca_2Si_5N_8$:Eu^{2+}	Orange	605	(0.620; 0.380)	Synthesis	[55]
SrS:Eu^{2+}	Orange	606	-	Stability	[56]
$SrAlSiN_3$:Eu^{2+}	Orange	610	-	Synthesis	[57]
$BaSiN_2$:Eu^{2+}	Red	620	(0.585; 0.410)	Synthesis, stability	[4]
$Sr_2Si_5N_8$:Eu^{2+}	Red	625	(0.621; 0.368)	Synthesis	[58]
$SrAlSi_4N_7$:Eu^{2+}	Red	635	-	Synthesis	[59]
CaS:Eu^{2+}	Red	648	(0.703; 0.297)	Stability	[56]
$CaAlSiN_3$:Eu^{2+}	Red	649	(0.647; 0.347)	Synthesis	[60]
$SrSiN_2$:Eu^{2+}	Red	700	(0.677; 0.322)	Synthesis, stability	[4]

The *Table 2.1* is obviously dominated by phosphors doped with Eu^{2+} or Ce^{3+} ions. Both of them possess optically allowed $[Xe]4f^n \rightarrow [Xe]4f^{n-1}5d^1$ absorption and $[Xe]4f^{n-1}5d^1 \rightarrow [Xe]4f^n$ emission transitions. The optical transitions involve 5d orbitals, which participate in chemical bonds of the activator ions to its chemical surrounding. Therefore, the position of the lowest excited 5d-levels is sensitive to the local environment of the ion and can be tuned by changing the host lattice (e.g. silicates, aluminates, nitrides, etc.) or modifying the host lattice itself (e.g. replacing Y by Lu in YAG:Ce). Thus the absorption band can be shifted to the near-UV or blue spectral region where the ions can be efficiently excited by the respective LED.

2.2. Via Near-UV LED Chip

The first near-UV LEDs were very inefficient. Therefore, there was no interest for practical application of such devices. However, the efficiency of these LEDs in recent years was considerably increased and the possibility of application in solid state light sources emerged. Near-UV LEDs possess one feature that their blue counterparts do not – the wider choice of phosphors. Since the near-UV LEDs usually emit in the range of 380 to 420 nm, the amount of suitable activators, other than Eu^{2+} and Ce^{3+}, considerably increases, e.g. Eu^{3+}, Pr^{3+}, Mn^{4+}, Tb^{3+}, Sm^{2+}, Sm^{3+} [61-70]. Among these ions Eu^{3+} is probably the most promising one, since it features sharp line emission (thus high colour saturation), high luminous efficacy, high stability, and high efficiency [71, 72]. However, like all the other rare earth ions it suffers from the low absorption due to the spin and parity forbidden character of its intraconfigurational $[Xe]4f^n \rightarrow [Xe]4f^n$ transitions. On the other hand, this drawback can be overcome by doping Eu^{3+} ions into those host lattices with a low lying charge transfer band, e.g. molybdates, tungstates, niobates, and vanadates [73-79].

There are two main approaches of generating white light employing near-UV LED as pumping source. Both of them employs RGB concept, i.e. the white light is generated by mixing red, green, and blue colours. The only difference is that one method employs broad band red emitting phosphor and another line emitting red phosphor. The latter one in terms of luminous efficacy of the device is more preferable, since the emission at wavelengths longer than 650 nm, according to Žukauskas et al., is considered as "waste" [80]. The graphical illustration of both mentioned methods is given in *Figure 2.2*.

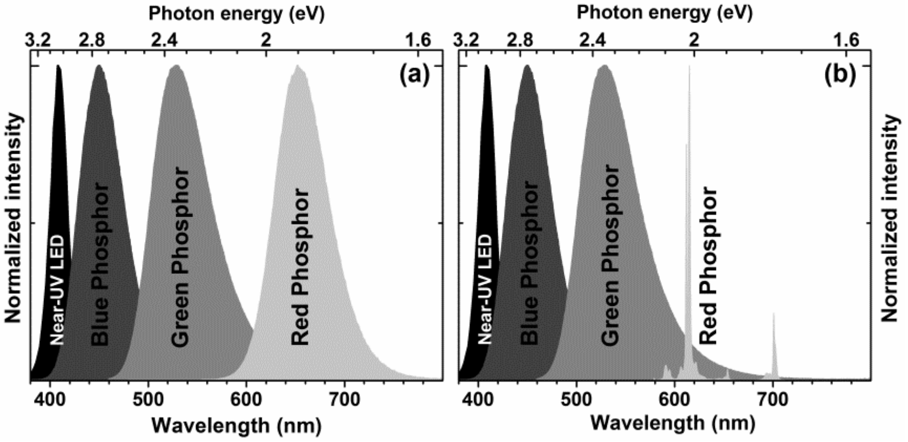

Figure 2.2 *Normalized emission spectra of near-UV chip based pcLEDs employing: (a) broad band and (b) line emitting red phosphor.*

Recently the single phase white emitting phosphors as an alternative to RGB concept emerged. These phosphors possess emission spectra with two or more bands usually resulting from the energy transfer from Eu^{2+}/Ce^{3+} to Mn^{2+}. The host lattices of such phosphors are silicates, borates, aluminates, and phosphates, where Eu^{2+} or Ce^{3+} generally emits in the blue spectral region. A fraction of this blue emission is transferred to the co-activator, like Mn^{2+}, for instance, which in turn emits in the orange or red spectral region, thus resulting in the colour mixture perceived as white. The emission of Mn^{2+} can be adjusted by selecting the appropriate host lattice, similar like Eu^{2+}. The colour point of such phosphors can be adjusted by selecting appropriate concentrations of blue and orange/red emitting ions. The overview of the recently reported single phase white-emitting phosphors is given in *Table 2.2*.

Table 2.2 *Characteristics of some recently reported single-phase white-emitting phosphors for near-UV LED based pcLEDs [31].*

Phosphor	**Excitation (nm)**	**Emission (nm)**	**CIE 1931 (x; y)**	**Ref.**
$Sr_3MgSi_2O_8:Eu^{2+},Mn^{2+}$	375	470, 570, 680	(0.35; 0.33)	[81]
$Ba_3MgSi_2O_8:Eu^{2+},Mn^{2+}$	400	442, 505, 620	-	[82]
$Ca_2MgSi_2O_7:Eu^{2+},Mn^{2+}$	381	528, 602	(0.45; 0.44)	[83]
$CaMgSi_2O_6:Eu^{2+},Mn^{2+}$	365	450, 580, 680	-	[84]
$Ca_5MgSi_3O_{12}:Eu^{2+},Mn^{2+}$	353	430, 500, 548	(0.29; 0.34)	[85]
$CaAl_2Si_2O_8:Eu^{2+},Mn^{2+}$	354	425, 568	(0.33; 0.31)	[86]
$Y_4MgSi_3O_{13}:Bi^{3+},Eu^{3+}$	350	485, 614	(0.31; 0.31)	[87]
$Y_4MgSi_3O_{13}:Ce^{3+},Mn^{2+}$	328	455, 587	(0.36; 0.26)	[88]
$Sr_3B_2O_6:Eu^{2+},Ce^{3+}$	351	434, 574	(0.31; 0.24)	[89]
$Ba_2Ca(BO_3)_2:Ce^{3+},Mn^{2+}$	345	420, 480, 625	(0.33; 0.31)	[90]
	395	505, 625	(0.35; 0.41)	
$Ba_2Ca(B_3O_6)_2:Eu^{2+},Mn^{2+}$	330	459, 608	(0.37; 0.25)	[91]
$Ca_2BO_3Cl:Ce^{3+},Eu^{2+}$	349	421, 575	(0.326; 0.334)	[92, 93]
$Sr_3Al_2O_5Cl_2:Ce^{3+},Eu^{2+}$	330	444, 609	(0.35; 0.32)	[94]
$SrZn(PO_4)_2:Eu^{2+},Mn^{2+}$	365	416, 538, 613	(0.32; 031)	[95]
$Ca_2Al_2SiO_7:Ce^{3+},Tb^{3+}$	352	419, 542	(0.316; 0.336)	[96]
$Ca_{10}K(PO_4)_7:Eu^{2+},Mn^{2+}$	347	467, 634	(0.35; 0.24)	[97]
$Ca_9Y(PO_4)_7:Eu^{2+},Mn^{2+}$	365	486, 638	(0.31; 0.33)	[98]
$(Sr,Ca)P_2O_7:Eu^{2+},Mn^{2+}$	400	430, 610	(0.36; 0.28)	[99]
$Sr_3Gd(PO_4)_3:Eu^{2+},Mn^{2+}$	355	500, 620	(0.401; 0.405)	[100]
$Ca_4Si_2O_7F_2:Ce^{3+},Mn^{2+}$	330	450, 580	(0.35; 0.42)	[101]
$Sr_2Mg_3P_4O_{15}:Eu^{2+},Mn^{2+}$	380	450, 610	-	[102]
$(Sr,Ba)_2B_2P_2O_{10}:Eu^{2+},Mn^{2+}$	371	430, 600	(0.321; 0.333)	[103]

Chapter 3. Fundamentals of the Activator Ions

In this chapter, the properties of lanthanide ions, i.e. Eu^{3+}, Eu^{2+}, and Ce^{3+} used as activators in the materials described within this thesis will be briefly described in order to introduce the reader with their exciting properties.

3.1. Lanthanide Luminescence

Lanthanides are very similar to each other in terms of chemical properties, therefore, it took more than 100 years to efficiently separate them [104, 105]. The lanthanide ions are characterized by gradual filling of the 4f subshell, which is well shielded from the chemical environment by $5s^2$ and $5p^6$ orbitals [106, 107]. Thus 4f orbitals do not participate in bonding and the optical properties of these ions are relatively insensitive to the environment, e.g. solvent, coordinated ligands, host lattice and so on. The incomplete occupation of shielded 4f shell is the reason of interesting luminescence properties of lanthanide ions, with many of them showing very sharp lines. These lines originate from the intraconfigurational $[Xe]4f^n \rightarrow [Xe]4f^n$ transitions and was intensively studied in the last century. The research led to invention of fluorescent tubes, colour television, X-ray phosphors, plasma display panels (PDPs), up-conversion phosphors, phosphors for counterfeiting purposes, afterglow phosphors, fibre amplifiers for telecommunication, solid state lasers and so on [108-115]. Moreover, besides line emission some of the lanthanide ions also possess broad band $[Xe]4f^n \rightarrow [Xe]4f^{n-1}5d^1$, and CT transitions.

3.1.1. Russell – Saunders Spectroscopic Terms

In order to describe the electronic states of atoms or ions the spectroscopic terms were developed. For the characterization of the electronic transitions in an ion the data of the total orbital angular momentum number – $\boldsymbol{L}$, and total spin – $\boldsymbol{S}$ is required. The total spin ($\boldsymbol{S}$) of the electronic state can be written as a vector sum of the spin angular momenta of the individual electrons [116]:

$$\vec{S} = \overrightarrow{s_1} + \overrightarrow{s_2} + \cdots \qquad (Eq. 3.1)$$

where ***s*** is the spin of the individual electron and can be either +½ or -½. Similarly, the total orbital angular momentum (***L***) is the vector sum of the individual orbital momenta of the electrons:

$$\vec{L} = \overrightarrow{l_1} + \overrightarrow{l_2} + \cdots \qquad (Eq. 3.2)$$

where ***l*** is the orbital angular momentum of the individual electron. In spectroscopic notation the first few symbols of ***L*** are:

***L* =**	**0**	**1**	**2**	**3**	**4**	**5**	**6**	**7**
notation	**S**	**P**	**D**	**F**	**G**	**H**	**I**	**K**

and later they are continued alphabetically. By coupling ***S*** and ***L*** the total angular momentum (***J***) is obtained. If the ***S*** and ***L*** values are known, the term symbol of the state can be written and ***J*** values calculated:

$$^{2S+1}L_J \qquad \text{(Eq. 3.3)}$$

The number ***2S+1*** defines the spin multiplicity of the term. ***J*** can be expressed as a vector sum of ***S*** and ***L***:

$$\vec{J} = \vec{L} + \vec{S} \qquad (Eq. 3.4)$$

and *J* can take the integer values:

$$|L - S| \leq J \leq |L + S| \qquad \text{(Eq. 3.5)}$$

By knowing the amount of electrons (***n***) in the 4f orbital one can calculate the number (***N***) of possible electronic configurations that the lanthanide ion can acquire [117]:

$$N = \frac{14!}{n!\,(14-n)!} \qquad 0 \leq n \leq 14 \qquad (Eq. 3.6)$$

The number ***N*** for all Ln^{3+} ions is given in the *Table 3.1*:

Table 3.1 *The number of possible electronic configurations of trivalent lanthanide ions.*

Ln^{3+}	**La^{3+}/ Lu^{3+}**	**Ce^{3+}/ Yb^{3+}**	**Pr^{3+}/ Tm^{3+}**	**Nd^{3+}/ Er^{3+}**	**Pm^{3+}/ Ho^{3+}**	**Sm^{3+}/ Dy^{3+}**	**Eu^{3+}/ Tb^{3+}**	**Gd^{3+}**
n	0/14	1/13	2/12	3/11	4/10	5/9	6/8	7
N	1	14	91	364	1001	2002	3003	3432

The ground state term of the ion is found by applying Hund's rule: it must have the highest spin multiplicity and the highest total orbital angular momentum [118]. The ***J*** value for the ground state term is calculated as follows [119]:

- if $n \leq 6$, then $J = |L - S|$
- if $n = 7$, then $J = S$
- if $n \geq 8$, then $J = L+S$.

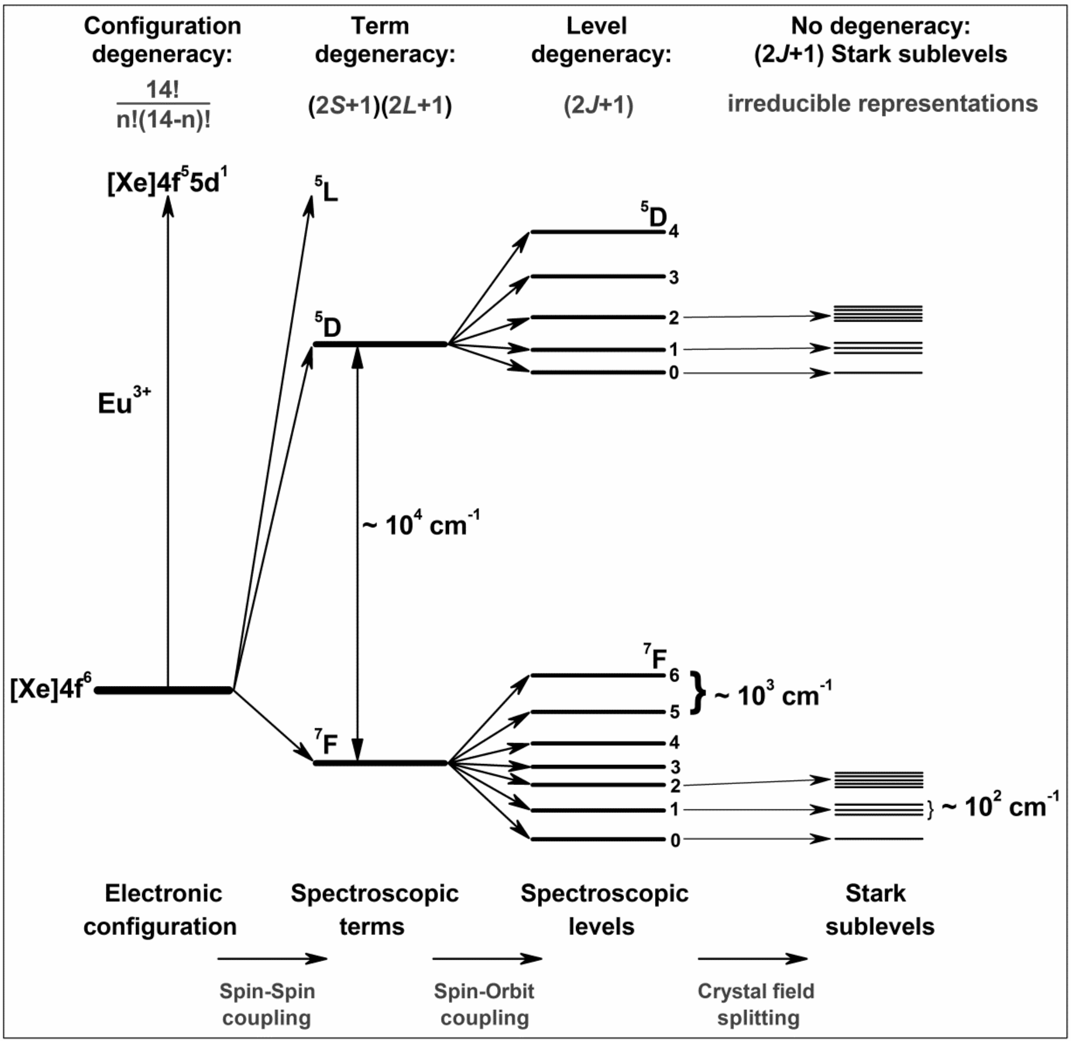

Figure 3.1 *Splitting of the energy levels of the [Xe]4f^6 configuration (Eu^{3+}) (adopted from [120-122]).*

The energies of the terms are determined by a combination of the interelectronic repulsion, spin-orbit coupling and, in a coordination environment, the ligand field [120]. These interactions that split up the levels of the [Xe]4f^n configuration are explained in *Figure 3.1*, where Eu^{3+} ion was taken as an example.

The first perturbation is caused by the electron repulsion (Coulomb interaction) within 4f orbitals resulting in the terms with the energy separation in the order of 10^4 cm^{-1} [123, 124]. The spectroscopic terms split further into several $\boldsymbol{J}$ levels, due to spin–orbit coupling (the second perturbation). The number of the $\boldsymbol{J}$ levels can be calculated employing Eq. 3.5. The spin–orbit coupling leads to $\boldsymbol{J}$ levels separated by the energy in the order of 10^3 cm^{-1} [124, 125]. The obtained $\boldsymbol{J}$ levels can split further to so called Stark sublevels due to ligand field effect from the coordination polyhedron around the lanthanide ion. The splitting of the Stark sublevels is in the order of 10^2 cm^{-1} [120, 124, 126, 127]. The maximum multiplicity of the $\boldsymbol{J}$ levels is $(\boldsymbol{2J + 1})$ and depends on the site symmetry of the lanthanide ion [128]. Therefore, the lanthanide ions possessing [Xe]4f^n → [Xe]4f^n transitions can be used as probes for clarifying the site symmetries. The number of Stark sublevels as a function of the site symmetry can be found in the literature [129, 130]. Moreover, if the ion is affected by the external magnetic field, the spectral lines also split due to Zeeman splitting [118]. All of the mentioned interactions (except Zeeman splitting) are depicted in *Figure 3.1* for better visualization.

3.1.2. Selection Rules of the Intraconfigurational f-f Transitions

Electronic transitions of lanthanide ions occur due to the interaction of their electrons with the electric or magnetic component of the electromagnetic radiation. However, not every possible transition is observed in atomic (ionic) spectra. This is because besides the energy conservation, the conservation of angular momentum and some certain symmetry rules must be obeyed [131]. The initial and final state of [Xe]4f^n → [Xe]4f^n transitions has the same parity. Therefore, the ED transitions are forbidden by the Laporte’s (or parity) selection rule, which requires that the sum of angular momenta of the electrons in the initial and final states must change by an odd integer, i.e. the initial and final states must be of opposite parity (***P***) [128, 129]:

$$P = (-1)^{\Sigma l} \qquad (Eq.\ 3.7)$$

In cases where ED transitions are forbidden, the MD transitions can be observed. However, usually the MD transitions are weaker and thus slower than ED transitions by a factor of 10^5 [132]. The other selection rules that apply to ***S***, ***L***, and ***J*** quantum numbers are listed in *Table 3.2*.

Table 3.2 *Selection rules for f-f transitions between spectroscopic levels [122, 129, 133].*

Transition	**Parity**	$\Delta \boldsymbol{S}$	$\Delta \boldsymbol{L}$	$\Delta \boldsymbol{J}^a$
ED	Opposite	0	≤ 6 ($\Delta \boldsymbol{l} = \pm 1$)	≤ 6 (2, 4, 6 if ***J*** or ***J'*** = 0)
MD	Same	0	0	0, ±1
EQ	Same	0	0, ±1, ±2	0, ±1, ±2
[a] ***J*** = 0 ↔ ***J'*** = 0 transitions are always forbidden.				

The spin selection rule ($\Delta \boldsymbol{S} = 0$) arises from the fact, that light (electromagnetic radiation) does not affect spin. However, the spin selection rule is relaxed to some extent because the heavy atoms have large spin-orbit (***LS***) coupling. The parity ($\Delta \boldsymbol{L}$) selection rule originates from the fact that absorption of light through ED transitions requires a change of ED in the transition state between ground state and excited state. Yet, no change in dipole is induced for transitions between states of the same parity and these transitions are, therefore, forbidden. The same applies for the transitions within the d-shell, and between d and s shells [116].

It was already mentioned that f-electrons are not much affected by the changes in the local environment due to efficient shielding by 5s and 5p orbitals. Therefore, the dipole strength of a particular transition in different matrices will not vary more than a factor of two or three. However, there are several transitions whose intensity can change by a factor of 200 depending on the chemical environment [133-135]. Such transitions were named as *hypersensitive transitions* [136]. As a matter of fact these transitions obey the same selection rules ($\Delta S = 0$, $\Delta L \leq 2$ and $\Delta J \leq 2$) as EQ transitions. Therefore, hypersensitive transitions are also known as *pseudo-quadrupole transitions*.

3.1.3. Interconfigurational [Xe]4f^n ↔ [Xe]4f^{n-1}5d^1 and CT Transitions

The 5d orbitals of lanthanide ions are not shielded like 4f orbitals and, therefore, are more spatially extended. The 5d orbitals also participate in the chemical bonding, thus their energy are greatly influenced by the local surrounding (host lattice). [Xe]4f^n ↔ [Xe]4f^{n-1}5d^1 transitions belong to the interconfigurational transitions and are parity allowed, which results in strong and broad absorption/emission bands. The spectral position of the 5d band is mainly influenced by two factors: the nephelauxetic effect (electron cloud expansion) also called covalency, and crystal field splitting [2, 137]. The nephelauxetic effect can be understood by comparing the electronegativity (EN) between two atoms. For instance, in materials where the EN difference is large (e.g. NaF), the electrons will reside on either Na^+ or F^- resulting in ionic bonding. However, in materials where the EN difference is smaller and the bond is covalent the electron cloud is shared between the atoms. The 5d electrons are thus more delocalized over the ligands what results in the shift of 5d state to the lower energies [2]. The crystal field can be explained as a static electric field resulting from the negatively charged ligand surrounding the lanthanide ion. The strength of the crystal field thus depends on the charge of the ligands, for instance, fluorides (F^-) will generate weaker crystal field than oxides (O^{2-}), and nitrides (N^{3-}) will generate stronger crystal field than oxides. Furthermore, the atomic and oxidation number of the lanthanide ion also influences the crystal field strength, which increases with the increase of both mentioned numbers [107]. The strength of crystal field also depends on the size of the lattice site into which the lanthanide ion is doped. Generally, the large sites generate weaker crystal field and the small ones – stronger [137]. The coordination polyhedron is also important. It is well known that the crystal field splitting decreases in the order given below:

octahedral > *cubic, dodecahedral, square-antiprismatic* > *tetrahedral*.

Moreover, the energy difference is always found between the excitation and emission energy: the so called Stokes' shift (this phenomenon was first observed by Sir. G. G. Stokes in 1852 at the University of Cambridge [138]). One common cause of the Stokes shift is the rapid decay to the lowest vibrational level, from which the emission occurs [139]. The graphical representation of the mentioned three factors influencing the $[Xe]4f^{n} \leftrightarrow [Xe]4f^{n-1}5d^{1}$ transitions is given in *Figure 3.2*.

Another type of allowed optical transitions are charge transfer transitions, which can be expressed as $[Xe]4f^{n} \rightarrow [Xe]4f^{n+1}L^{-1}$, where L is a ligand [137]. In general, CT transitions are found for lanthanide ions that can be reduced (e.g. Eu^{3+}, Sm^{3+}, Yb^{3+}), and $[Xe]4f^{n} \leftrightarrow [Xe]4f^{n-1}5d^{1}$ transitions for ions that can be oxidized (e.g. Ce^{3+}, Pr^{3+}, Tb^{3+}) [119, 137].

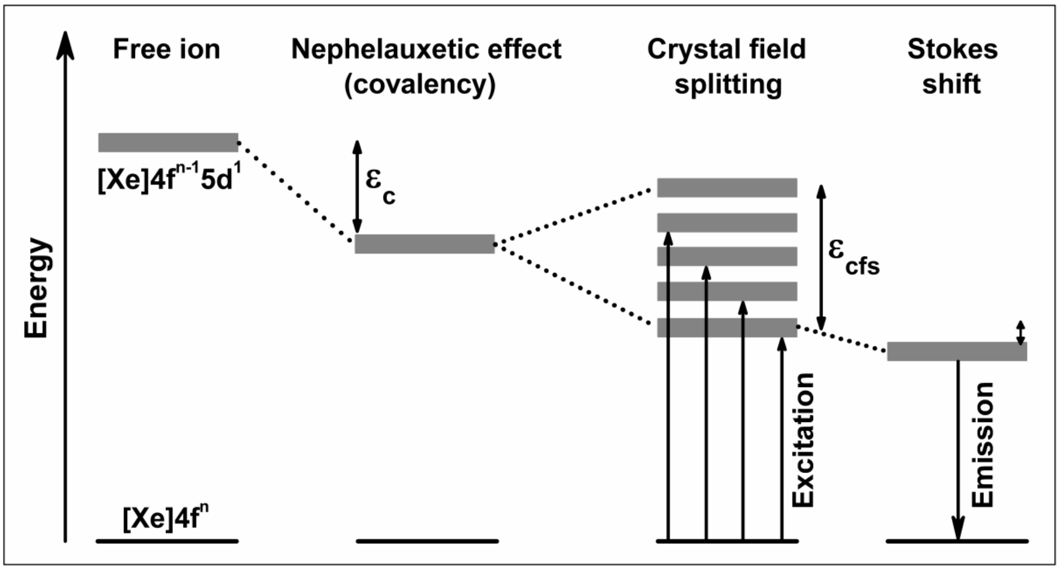

Figure 3.2 *The influence of covalency, crystal field splitting and Stokes shift to the position of 5d states.*

3.2. Characteristics of Eu^{3+}, Eu^{2+}, and Ce^{3+} Ions

3.2.1. Luminescence Properties of Eu^{3+} Ions in Different Host Lattices

The orange/red emission from Eu^{3+} ions in different host lattices is widely applied in various devices, viz. fluorescent tubes, CRTs, PDPs, security pigments and others [32, 109, 140-142]. The emission of Eu^{3+} mainly originates from $^{5}D_{0} \rightarrow {}^{7}F_{J}$ transitions. However, at low Eu^{3+} concentrations the emission lines corresponding to the $^{5}D_{2} \rightarrow {}^{7}F_{J}$ (blue-green spectral region) and $^{5}D_{1} \rightarrow {}^{7}F_{J}$ (green-yellow spectral region) transitions can be observed. At higher

Eu^{3+} concentrations these transitions are quenched due to cross-relaxation process, ($^5D_J \rightarrow {}^5D_0$) → ($^7F_0 \rightarrow {}^7F_J$) [119]. It was already mentioned that 4f orbitals of lanthanide ions are shielded by 5s^2 and 5p^6 orbitals. Therefore, the spectral position of emission lines originating from the intraconfigurational [Xe]4f^n ↔ [Xe]4f^n transitions are relatively independent on the chemical environment of the lanthanide ion. However, the emission spectra still can be tuned. This can be done by selecting the appropriate lattice site, where the lanthanide ion is doped into. Generally, ED transitions are strictly forbidden if lanthanide ions sit in a lattice site with inversion symmetry and in such materials only MD transitions are observed [119, 137].

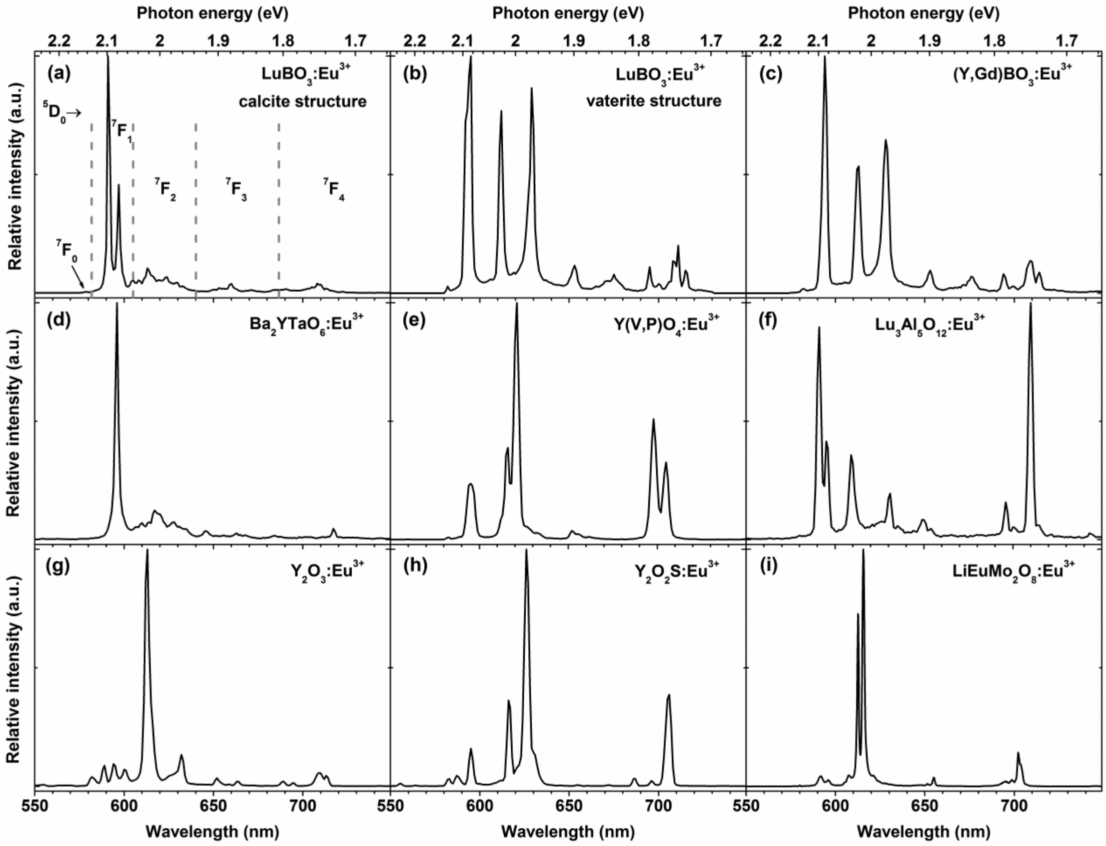

Figure 3.3 *Emission spectra of Eu^{3+} ions in different host lattices (the range of different $^5D_0 \rightarrow {}^7F_J$ transitions were adopted from Bettentrup [143] and Ronda [32]).*

Figure 3.3 demonstrates that Eu^{3+} emission spectra are sensitive to the symmetry of the lattice site where Eu^{3+} is sitting. It can be concluded that if the line emitting phosphor in the orange spectral region needs to be obtained, the choice would be Eu^{3+} in the host lattice with suitable site possessing inversion symmetry. If red emission is desired, the Eu^{3+} sites with low symmetry should be chosen.

3.2.2. Luminescence Properties of Eu^{2+} Ions in Different Host Lattices

Different to its trivalent counterpart (Eu^{3+}), the Eu^{2+} ions feature the parity allowed interconfigurational $[Xe]4f^7 \leftrightarrow [Xe]4f^6 5d^1$ transitions. The emission band of Eu^{2+} ions can be tuned from near UV (≈ 370 nm in $SrB_4O_7:Eu^{2+}$) to near IR (≈ 700 nm in $SrSiN_2:Eu^{2+}$) as illustrated in *Figure 3.4*. The emission bands of all wavelengths in this range can be obtained by selecting the appropriate host lattice and Eu^{2+} concentration (emission band usually shifts to the longer wavelengths if activator concentration is increased). The host lattices with ionic character yields Eu^{2+} emission band at shorter wavelengths, whereas the host lattices with covalent character results in Eu^{2+} emission bands at longer wavelengths. The additional shifting Eu^{2+} emission band to one or other direction is influenced by size and shape of coordination polyhedron. Generally, the crystal field splitting decreases if the size of coordination polyhedron increases, i.e. the emission band shifts to the shorter wavelengths. As an example the isostructural compounds $Sr_2Si_5N_8$ and $Ba_2Si_5N_8$ can be taken. Ba ions are larger than Sr, therefore, the corresponding coordination polyhedron is larger for Ba ions. As a result $Ba_2Si_5N_8:Eu^{2+}$ emits at 572 nm [49] and $Sr_2Si_5N_8:Eu^{2+}$ at 625 nm [58].

Another important feature of phosphors considered for LED application is their emission band width. In this case the narrow bands are preferred, since they give the higher LE values than the broad ones. The line width can be controlled, to some extent, by selecting the host materials with different amount of lattice sites where Eu^{2+} ions can be doped to. The emission band broadens, e.g. with increasing number of Eu sites in the structure and with increasing Stokes shift. This results from the fact, that each site will give its own emission band due to the different coordination polyhedrons. The sum of these bands yields the one broad band. However, at low Eu^{2+} concentrations the separate bands can be distinguished in the emission spectra, especially at low temperatures [145-147].

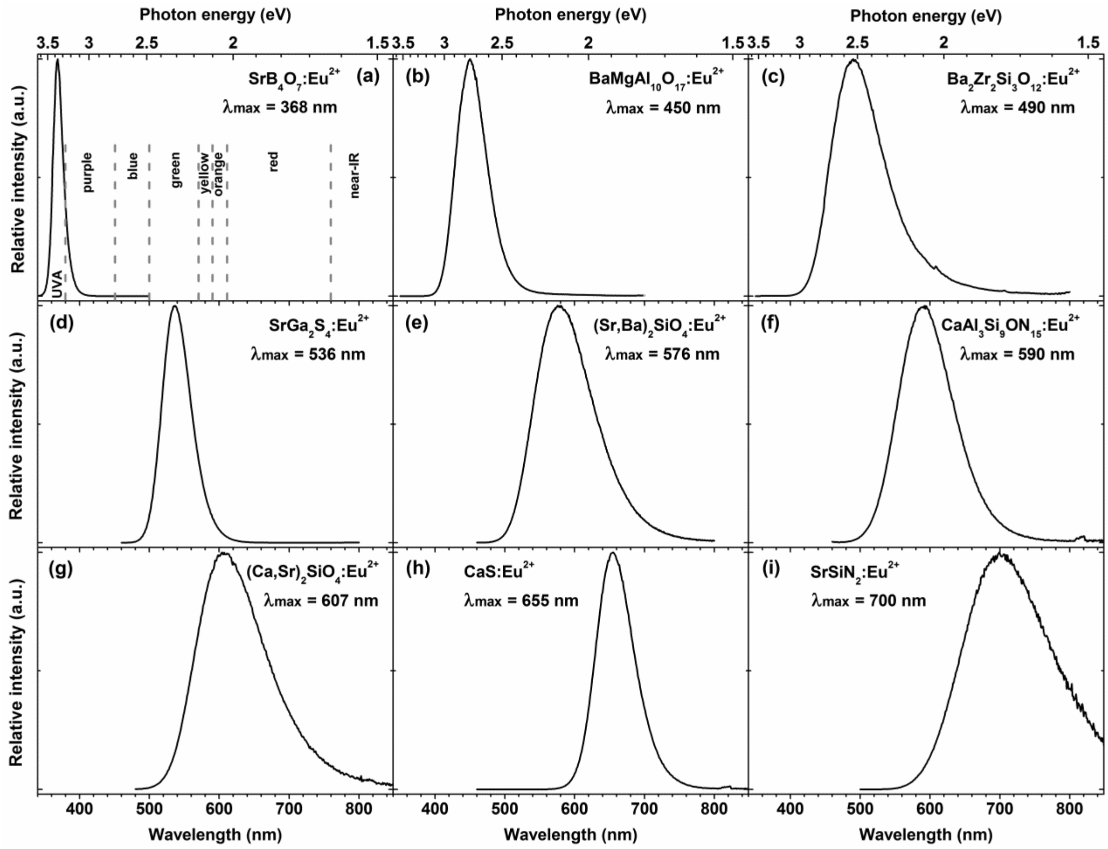

Figure 3.4 *Emission spectra of Eu^{2+} ions in different host lattices (the ranges of colours were taken from ISO 21348:2007(E) [144]).*

Another factor determining the broadness of the Eu^{2+} emission band is the rigidity of the host lattice. The rigidity of the host lattice can be explained as the condensation (cross-linking) of the building blocks, SiN_4 units in the nitride lattices, for instance [148]. The narrow Eu^{2+} bands are obtained in the host lattices with high rigidity. The Eu^{2+} emission in rigid host lattices also quenches at higher temperatures [148], what is an advantage for the LED phosphor.

Finally, Van Uitert in 1984 published the equation, which allows theoretically predict the position of Eu^{2+} emission band originating from $[Xe]4f^65d^1 \rightarrow [Xe]4f^7$ transition [149]:

$$E(cm^{-1}) = Q\left[1 - \left(\frac{V}{4}\right)^{\frac{1}{V}}\right] \times 10^{\frac{-(nE_a r)}{80}} \qquad (Eq. 3.8)$$

where E is the position for the Eu^{2+} emission peak (in cm^{-1}), Q is the position of energy of the lower d-band edge for the free ion ($Q = 34000\ cm^{-1}$ for Eu^{2+}), V is the valence of activator ion ($V = 2$ for Eu^{2+}), n is the number of anions in the immediate shell around activator ion, E_a is the electron affinity (in eV) of the atoms that form the anions, and r is the radius (in Å) of the host cation replaced by Eu^{2+}.

3.2.3. Luminescence Properties of Ce^{3+} Ions in Different Host Lattices

Among the lanthanide ions Ce^{3+} is the simplest one. It possesses $[Xe]4f^1$ ground state configuration which is split to two spectroscopic levels ($^2F_{5/2}$ and $^2F_{7/2}$) separated by ~ 2000 cm^{-1} due to spin-orbit coupling. The excited $[Xe]5d^1$ state is split by the crystal field in 2 to 5 components [137]. The energy of emitted photons depends on the same factors as for earlier described Eu^{2+} ions, i.e. nephelauxetic effect (covalency), crystal field splitting, and the Stokes shift. The emission of Ce^{3+} ions originates from the lowest crystal field component of the $[Xe]5d^1$ configuration to the two terminating levels of the ground state, what gives a characteristic double-band shape of Ce^{3+} emission spectra [137]. Some examples of Ce^{3+} emission spectra in inorganic host lattices are given in *Figure 3.5*. It is obvious that in ionic lattices, viz. halides, phosphates, borates, the Ce^{3+} emission occurs at rather short wavelengths (from UVB to purple). The shortest wavelength emission of Ce^{3+} ions is usually observed in halides, 280 nm in $LiCaAlF_6$:Ce^{3+}, for instance [150]. However, if doped into more covalent lattices Ce^{3+} emit at much longer wavelengths (from blue to even near-IR). The strong emission red shift, on the other hand, is usually accompanied by strong concentration and thermal quenching as was recently reported by several researchers [44, 45, 53, 151-155].

For a prediction of the Ce^{3+} emission band in various materials the same equation (see Eq. 3.8) as for Eu^{2+} can be used. In Ce^{3+} case $Q = 50000\ cm^{-1}$ and $V = 3$. The Q values for other lanthanide ions can be found in reference [156].

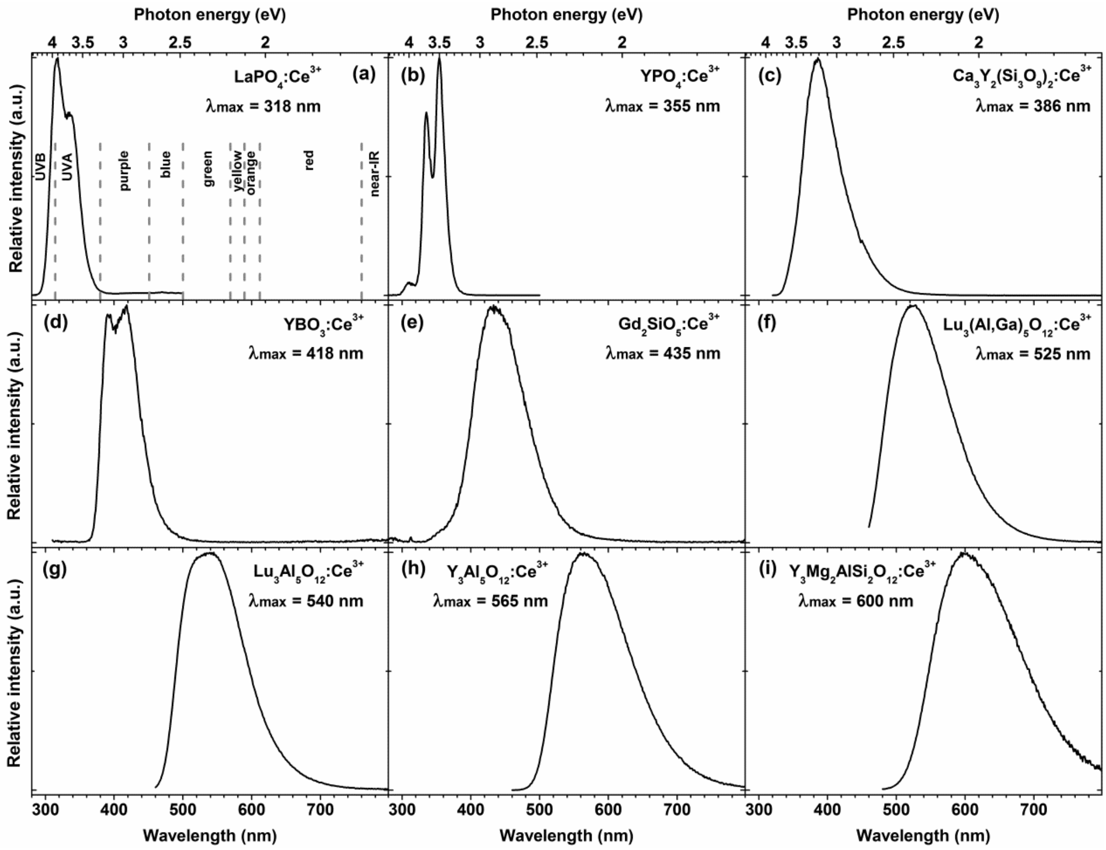

Figure 3.5 *Emission spectra of Ce^{3+} ions in different host lattices (the ranges of colours were taken from ISO 21348:2007(E) [144]).*

Chapter 4. Properties of the Host Materials

4.1. Crystal Structure of $Ba_2Zr_2Si_3O_{12}$

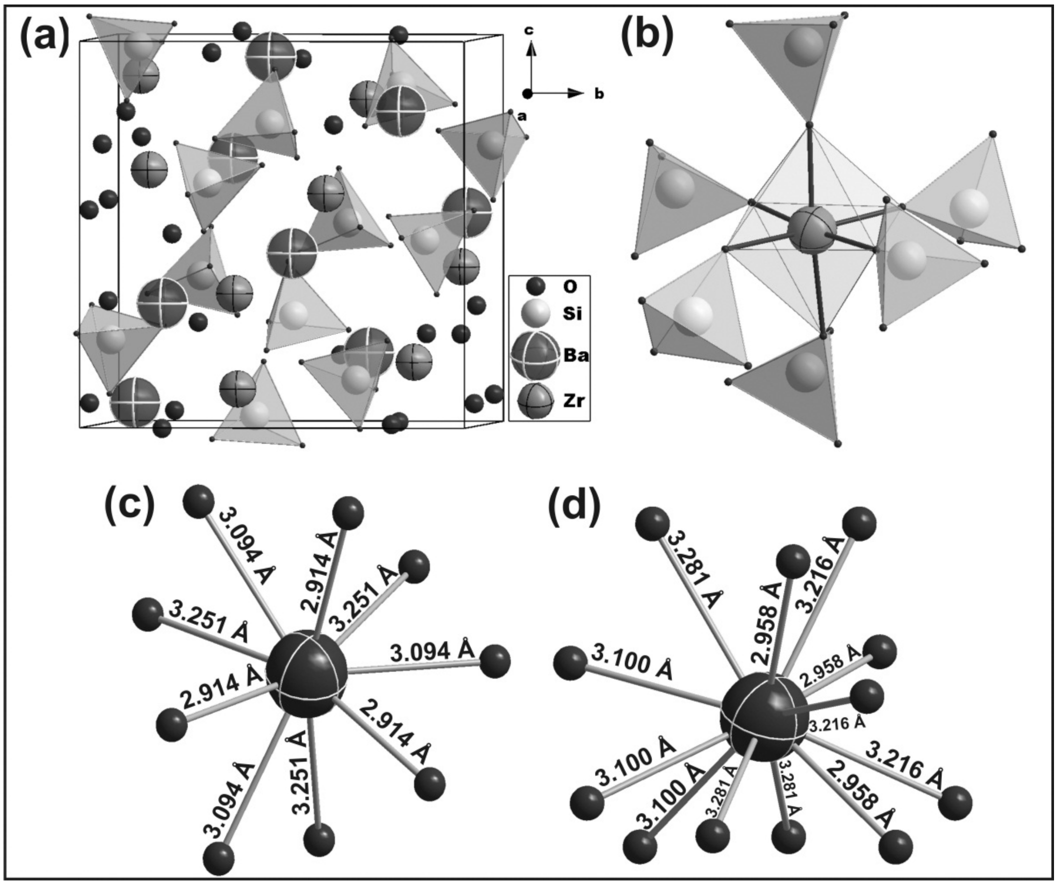

Figure 4.1 *(a) Unit cell of $Ba_2Zr_2Si_3O_{12}$; (b) building block consisting of [ZrO_6] sharing vertexes with [SiO_4]; (c) Ba1 site with CN = 9; (d) Ba2 site with CN = 12.*

The crystal structure of $Ba_2Zr_2Si_3O_{12}$ was first solved by R. Masse and A. Durif in 1973 [157]. $Ba_2Zr_2Si_3O_{12}$ crystallizes in the cubic crystal lattice with the space group $P2_13$ (198). The compound is classified as an orthosilicate, because it contains isolated [SiO_4] units (see *Figure 4.1a*). The structure is built from a framework of [ZrO_6] octahedrons sharing vertexes with [SiO_4] tetrahedrons as depicted in *Figure 4.1b*. Barium ions occupy the voids built by the mentioned network. According to the crystal structure data, there are two non-equivalent barium sites with coordination numbers 9 and 12 in the $Ba_2Zr_2Si_3O_{12}$ (see *Figure 4.1c* and *Figure 4.1d*, respectively). Both barium sites lie in complicated oxygen-polyhedrons with average Ba-O distances ≈ 3.086 and 3.139 Å for nine and twelve coordinated barium ions, respectively.

The ionic radius of Ba^{2+} (1.47 Å for CN = 9; 1.61 Å for CN = 12) is larger than that of Eu^{2+} (1.30 Å for CN = 9) [158]. Unfortunately, the ionic radius for twelve coordinated Eu^{2+} was not available in the literature. However, based on Ba^{2+} example, the radius of Eu^{2+} ion with CN = 12 should be slightly larger than that for CN = 9. Therefore, two types of Eu^{2+} ions in the $Ba_2Zr_2Si_3O_{12}$ structure are expected. This will lead to two different luminescent centres. It can be expected that 9-fold coordinated Eu^{2+} ions interact stronger with surrounding oxygen anions and, therefore, are affected by stronger crystal field and nephelauxetic (covalency) effects.

4.2. Crystal Structure of $Li_3Ba_2Gd_3(MoO_4)_8$

The structure of $Li_3Ba_2Gd_3(MoO_4)_8$ was reported by Klevtsova et al. in 1992 [159]. Since the structure of La derivative was not reported so far, the discussion of crystal structure will be based on $Li_3Ba_2Gd_3(MoO_4)_8$ compound. $Li_3Ba_2Gd_3(MoO_4)_8$ crystallizes in the monoclinic lattice with the space group C2/c (15). The unit cell along a-axis is depicted in *Figure 4.2a*. The crystal structure features two types of molybdenum ions with tetrahedral coordination. The barium ion is found in a special position on the 2-fold axis and is coordinated by 10 oxygen anions (*Figure 4.2b*). 66.7% of Li ions possess distorted octahedral coordination, whereas the rest share the same 8-fold coordinated site with Ba and Gd ions (*Figure 4.2c*). Therefore, the real composition of $Li_3Ba_2Gd_3(MoO_4)_8$ can be specified and written as $Li_2(Ba_{0.85}Gd_{0.15})_2(Gd_{0.675}Ba_{0.075}Li_{0.25})_4(MoO_4)_8$.

The vast majority of Gd^{3+} ions occupy the site with 8-fold coordination. Eu^{3+} and Gd^{3+} ions possess fairly similar ionic radii, 1.066 and 1.053 Å, respectively, for CN = 8 [158]. Therefore, one can assume that a solid solution will be formed at any Gd^{3+}/Eu^{3+} ratio. However, the shift of XRD peaks to smaller 2θ values can also be expected as smaller ions are substituted by larger ones, resulting in lattice expansion.

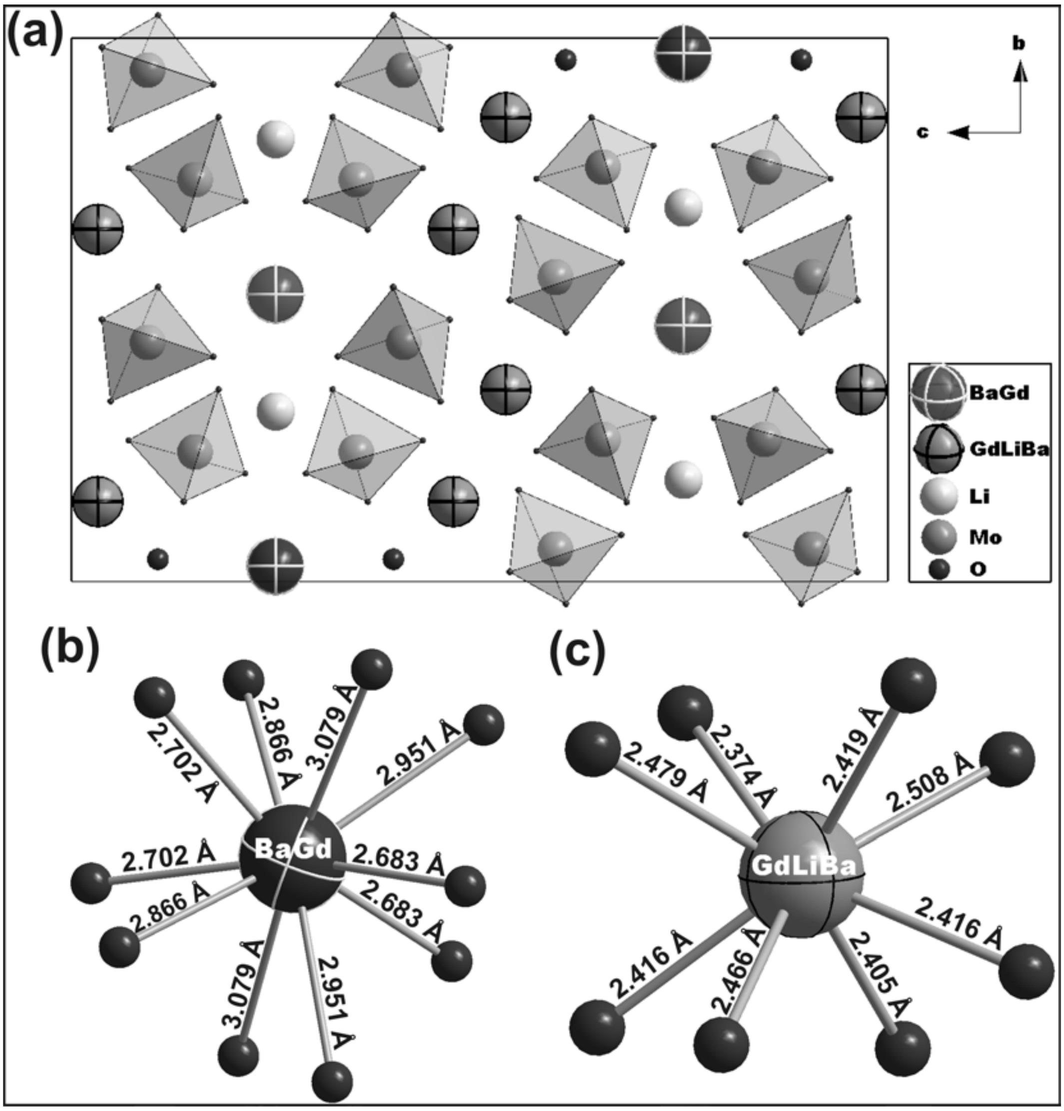

Figure 4.2 *(a) Unit cell* $Li_3Ba_2Gd_3(MoO_4)_8$ *along a-axis; (b) Ba,Gd site with CN = 10; (c) Gd,Li,Ba site with CN = 8.*

4.3. Crystal Structure of the Garnet Type Compounds

Garnet crystal structure (the sample was mineral Grossular, $Ca_3Al_2Si_3O_{12}$) was first solved by G. Menzer in 1926 [160]. He found that garnet type compounds crystallize in the cubic lattice with the space group $Ia\overline{3}d$ (230). The general formula of the garnet type compounds is $\{A_3\}[B_2](C_3)O_{12}$, where {}, [], and () denote dodecahedral, octahedral, and tetrahedral coordination, respectively [161]. All cation positions are fixed by symmetry, whereas anions occupy the general position and thus have three degrees of positional freedom. The unit cell of $Ca_3Al_2Si_3O_{12}$ along c-axis is shown in *Figure 4.3a*. The dodecahedral and tetrahedral sites are marked as dark grey and transparent light grey polyhedrons, respectively. *Figure 4.3b* represents the local environment of the dodecahedral site. Each dodecahedron shares vertexes with four tetrahedrons, and edges with two tetrahedrons, four octahedrons and four other dodecahedrons. In general it can be said that the garnet crystal structure is built from a 3D framework of [BO_6] octahedrons and (CO_4) tetrahedrons and larger ions in 8-coordinated interstices of the framework [162].

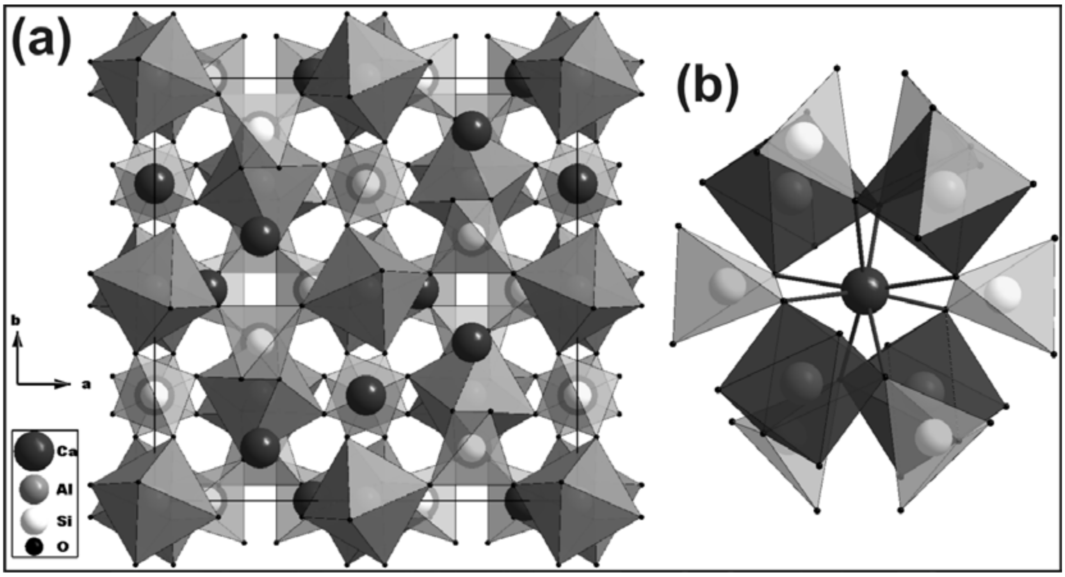

Figure 4.3 *(a) Unit cell of $Ca_3Al_2Si_3O_{12}$ along c-axis; (b) the local environment of the dodecahedral site.*

Chapter 5. Experimental

5.1. Preparation of Samples

5.1.1. Synthesis of $Ba_{2-x}Eu_xZr_{2-y}Hf_ySi_3O_{12}$

$Ba_{2-x}Eu_xZr_{2-y}Hf_ySi_3O_{12}$ powder samples were prepared by conventional high temperature solid-state reaction. The stoichiometric amounts of high purity raw materials ($BaCO_3$, ZrO_2, HfO_2, Eu_2O_3 and nano-scale SiO_2) were thoroughly mixed in the agate mortar employing acetone as grinding media. 0.5 wt-% of boric acid H_3BO_3 was used as a flux. The blends of starting materials were dried, transferred to the alumina crucibles and annealed at 1450 °C for 5 h under CO atmosphere (heating rate 300 °C/h). The second sintering step was performed in the horizontal tube furnace at 1200 °C for 5 h under N_2/H_2 (95%/5%) gas flow (heating rate 300 °C/h). A series of $Ba_{2-x}Eu_xZr_{2-y}Hf_ySi_3O_{12}$ phosphors were prepared with different Eu^{2+} (x = 0, 0.01, 0.02, 0.04, 0.08, 0.016) and Hf^{4+} (y = 0, 0.4, 0.8, 1.2, 1.6, 2.0) concentrations.

5.1.2. Synthesis of $Li_3Ba_2La_{3-x}Eu_x(MoO_4)_8$

$Li_3Ba_2La_{3-x}Eu_x(MoO_4)_8$ phosphor powders were prepared by conventional high temperature solid-state reaction. The stoichiometric amounts of high purity raw materials (Li_2CO_3, $BaCO_3$, La_2O_3, Eu_2O_3 and MoO_3) were thoroughly mixed in the agate mortar employing acetone as grinding media. The mixtures of starting materials were dried, transferred to the porcelain crucibles and annealed at 800 °C for 10 h in air. A series of $Li_3Ba_2La_{3-x}Eu_x(MoO_4)_8$ phosphors were prepared with different Eu^{3+} (x = 0, 0.3, 0.6, 0.9, 1.2, 1.5, 1.8, 2.1, 2.4, 2.7, 3.0) concentrations.

5.1.3. Synthesis of $Y_{3-x}Lu_xAl_3MgSiO_{12}:Ce^{3+}$

The samples with composition of $Y_{3-x}Lu_xAl_3MgSiO_{12}:Ce^{3+}$ were prepared by aqueous sol-gel technique employing 1,2-ethanediol as complexing agent. Firstly, yttrium and/or lutetium oxides were dissolved in hot diluted nitric acid. The solution was evaporated till dryness to remove the excess of nitric acid. The dry residue was again dissolved in distilled water and appropriate amounts of cerium, aluminium, magnesium nitrates and silicon dioxide were added. The resulting mixtures were stirred for 1 h at temperatures between 70 and 80 °C. Then 1,2-ethanediol was added with the molar ratio of 1:2 to all metal ions and the obtained mixtures were stirred for an additional hour at the same temperature. Subsequently, after concentrating the solutions by slow evaporation under stirring the (Y, Lu, Ce)–Al–Mg–Si–O nitrate glycolate sols turned into transparent gels. The oven dried (150 °C) gels became brownish due to initial decomposition of nitrates. The gel powders were powderized in an agate mortar and preheated at 1000 °C for 2 h in air. Since the gels were very combustible a slow heating of 1 °C/min was found to be essential. The obtained slightly yellowish powders were ground and subsequently sintered at 1600 °C for 4 h under CO atmosphere. A series of $Y_{3-x}Lu_xAl_3MgSiO_{12}:Ce^{3+}$ phosphors were prepared with different Lu^{3+} (x = 0, 1, 2, 3) concentrations. For each Lu^{3+} concentration samples with four different concentrations (0.25, 0.5, 0.75, 1.0 mol-% from Y/Lu amount) of Ce^{3+} located on the dodecahedral garnet site were prepared. The undoped samples were prepared in the same manner just without addition of Ce^{3+} source.

5.1.4. Synthesis of $CaLu_2Al_4SiO_{12}:Ce^{3+}$ and $CaY_2Al_4SiO_{12}:Ce^{3+}$

$CaLu_2Al_4SiO_{12}:Ce^{3+}$ phosphor powders were prepared by sol-gel combustion process employing THMAM as both complexing agent and fuel. Firstly, lutetium oxide was dissolved in hot diluted nitric acid. Then the solution was evaporated till dryness to remove the excess of nitric acid. The dry residue was again dissolved in distilled water and appropriate amounts of aluminium, calcium, cerium nitrates and silicon dioxide were added. The resulting mixtures were stirred for 1 h at a temperature between 65–75 °C. Then THMAM was added with the molar ratio of 1:1 to all metal ions and the obtained mixtures were stirred for an additional hour at the same temperature. Subsequently, after concentrating the mixtures by slow evaporation, sols turned into transparent gels. Then the temperature was raised to 250 °C and self-maintaining gel combustion process has started accompanied with evolution of huge amount of gas. The resulting products were dried in the oven overnight at 150 °C and ground to fine powders, which were preheated for 2 h at 1000 °C in air to remove the residual carbon after the combustion process. The obtained white–greenish powders were further sintered for 4 h at 1400, 1450 and 1500 °C under CO atmosphere. Further increase of the sintering temperature resulted in molten samples.

$CaY_2Al_4SiO_{12}:Ce^{3+}$ phosphor powders were prepared in the same way as $CaLu_2Al_4SiO_{12}:Ce^{3+}$, just yttrium was used instead of lutetium. The temperature of the second annealing step was 1400 and 1450 °C. Sintering phosphor powders at temperatures higher than 1450 °C resulted in molten samples.

The concentration of Ce^{3+} located on the dodecahedral garnet site was 0, 0.1, 0.25, 0.5, 0.75, 1.0, 1.5, 2.0, 2.5, and 3.0 mol-% in both systems.

5.2. Chemicals

The starting materials were Eu_2O_3 (99.99% Treibacher), La_2O_3 (99.99% Treibacher), $BaCO_3$ (99.0% AlfaAesar), ZrO_2 (99.5% AlfaAesar), HfO_2 (99.0% ChemPur), nano-scale SiO_2 (99.0% Merck), Li_2CO_3 (99.0% AlfaAesar), MoO_3 (99.5% AlfaAesar), Y_2O_3 (99.99% Treibacher), Lu_2O_3 (99.99% Treibacher), $Ce(NO_3)_3{\cdot}6H_2O$ (99.9% ChemPur), $Al(NO_3)_3{\cdot}9H_2O$ (≥98% Sigma-Aldrich), $Ga(NO_3)_3{\cdot}6H_2O$ (≥99.9% AlfaAesar), $Ca(NO_3)_2{\cdot}4H_2O$ (99.0% Merck), $Mg(NO_3)_2{\cdot}6H_2O$ (≥98% Sigma-Aldrich), H_3BO_3 (99.9% Merck), tris(hydroxymethyl)-aminomethane $H_2NC(CH_2OH)_3$ (99.9% Merck), 1,2-ethandiol $HOCH_2CH_2OH$ (100% BDH Prolabo).

5.3. Materials Characterization

5.3.1. TG/DTA Analysis

TG/DTA measurements of the raw materials blends (in solid-state synthesis) and gels (in sol-gel and combustion synthesis) were recorded on Thermoanalyser Netzsch STA 409. The heating rate was 10 K/min. Sample weight ~50 mg. Crucible material–Al_2O_3. The atmosphere was synthetic air.

5.3.2. Powder X-ray Diffraction

XRD data were collected using Ni-filtered Cu K_α radiation on Rigaku MiniFlex II diffractometer working in Bragg-Brentano ($\theta/2\theta$) geometry. The step width and integration time was 0.02° and 1 s, respectively.

5.3.3. SEM Analysis

SEM images were taken by a FE-SEM Hitachi SU-70 or Jeol JSM 6300F scanning electron microscopes. Before measurements samples were coated by thin chromium film to avoid charging.

5.3.4. VUV Spectroscopic Investigations

The VUV spectrometer (Edinburgh Instruments FS920) was used for exciting phosphor samples. The spectrometer was equipped with VUV monochromator VM504 from Acton Research Corporation (ARC) and deuterium lamp as an excitation source. Sample chamber was flushed with dried nitrogen in order to prevent absorption of VUV by water and oxygen. Excitation (excitation slit 1 mm, emission slit 2 nm) and emission (excitation slit 2 mm, emission slit 1 nm) spectra were recorded in the ranges of 150–375 nm and 200–800 nm, respectively. The emission spectra were corrected by correction file obtained from tungsten incandescent lamp certified by the NPL (National Physical Laboratory, UK). The relative VUV excitation intensities of the samples were corrected by dividing the measured excitation spectra of the samples with the excitation spectrum of sodium salicylate (o-$C_6H_4OHCOONa$)

taken under the same excitation conditions. During the measurements of entire emission spectra and excitation spectra in the range of 150–220 nm the sample chamber was flushed with dried nitrogen in order to avoid absorption of VUV radiation by oxygen and moisture.

The VUV reflection spectra in the range of 150–350 nm were taken on the aforementioned spectrometer equipped with an integration sphere coated with $BaMgAl_{10}O_{17}:Eu^{2+}$ (BAM:Eu). The reflection spectra were obtained as follows: first an excitation spectrum of BAM:Eu was recorded (λ_{em} = 451 nm), then excitation spectrum of the sample was recorded monitoring the same emission wavelength under the same conditions, i.e. emission and excitation slit sizes, step size, integration time, etc. Subsequently, excitation spectrum of the sample was divided by excitation spectrum of BAM:Eu giving reflection spectrum of the sample [163].

5.3.5. UV/VIS Spectroscopic Investigations

Reflection spectra in the UV/VIS range were recorded on Edinburgh Instruments FS920 spectrometer equipped with a 450 W Xe arc lamp, a cooled (-20 °C) single-photon counting photomultiplier (Hamamatsu R928) and an integration sphere coated with barium sulphate. $BaSO_4$ (99% Sigma-Aldrich) was used as a reflectance standard. The excitation and emission slits were set to 10 and 0.06 nm, respectively.

Excitation and emission spectra in the UV/VIS range were recorded on Edinburgh Instruments FLS920 spectrometer equipped with a 450 W Xe arc lamp, mirror optics for powder samples and a cooled (-20 °C) single-photon counting photomultiplier (Hamamatsu R2658P). The photoluminescence emission spectra were corrected by correction file obtained from tungsten incandescent lamp certified by the NPL.

For thermal quenching (TQ) measurements a cryostat “MicrostatN” from Oxford Instruments had been applied to the present spectrometer. Liquid nitrogen was used as a cooling agent. Temperature stabilization time was 60 s. Measurements were carried out from 77 to 500 K in 50 K steps.

5.3.6. Lifetime Measurements

The PL decay kinetics studies were performed on Edinburgh Instruments FSL900 spectrometer equipped with several excitation sources. Eu^{3+}-doped samples were excited with a Xe μs-flash lamp. Eu^{2+}-doped samples were excited with the 375 nm picosecond pulsed laser diode from Edinburgh Instruments (model–EPL375). Ce^{3+}-doped samples were excited with the 445.6 nm picosecond pulsed laser diode from Edinburgh Instruments (model–EPL445). Pr^{3+}-doped samples were excited with the 265 nm picosecond pulsed light emitting diode from Edinburgh Instruments (model–EPLED265).

5.3.7. QE Calculations

QE for the samples with available reference material was measured by indirect method, i.e. comparing the synthesized sample with the reference material with known QE. The QE was calculations were based on the equation [53]:

$$QE = QE_{Ref} \times \frac{\int(I_{Sample})d\lambda - \int(I_{Black})\,d\lambda}{\int(I_{Ref})\,d\lambda - \int(I_{Black})\,d\lambda} \times \frac{1 - R_{Ref}}{1 - R_{Sample}} \qquad \text{(Eq. 5.1)}$$

where QE_{Ref} is the quantum efficiency of the reference material, $\int(I_{Sample})d\lambda$, $\int(I_{Ref})d\lambda$ and $\int(I_{Black})d\lambda$ are emission integrals of the sample, reference material and black standard, respectively. R_{Ref} and R_{Sample} are reflection values of reference material and sample, respectively. The black standard (Flock Paper #55, Edmund Optics) was used to eliminate the dark count rate of the detector.

QE for the samples without available reference material was measured by direct method employing integration (Ulbricht) sphere coated with $BaSO_4$. For QE calculation the emission spectra (including the excitation wavelength) of the sample and $BaSO_4$ are measured. The difference in intensities at excitation wavelength range gives the number of absorbed photons, whereas the difference in intensities at emission range gives the number of emitted photons. The QE then is calculated by [119, 164]:

$$QE = \frac{N_{em}}{N_{abs}} \times 100\% \qquad \text{(Eq. 5.2)}$$

where N_{em} and N_{abs} are the number of emitted and absorbed photons, respectively.

The error of the QE calculations has been found to be ±5% for both methods.

5.3.8. LE Calculations

The LE, in lumen per watt optical, is a parameter describing how bright the radiation is perceived by the average human eye. It scales with the protopic human eye sensitivity curve $V(\lambda)$ and can be calculated from the emission spectrum $I(\lambda)$ of the sample as [30]:

$$LE\left(lm/W_{opt.}\right) = 683\ (lm/W_{opt.}) \times \frac{\int_{360nm}^{830nm} I(\lambda)V(\lambda)d\lambda}{\int_{360nm}^{830nm} I(\lambda)d\lambda} \qquad \text{(Eq. 5.3)}$$

5.3.9. $TQ_{1/2}$ Calculations

For the calculation of $TQ_{1/2}$ values (the temperature, at which phosphor loses half its efficiency) the Boltzmann sigmoidal fit of temperature dependent emission integrals or decay constants was employed. The fit equation is [165]:

$$y(x) = A_2 + \frac{A_1 - A_2}{1 + e^{(x-x_0)dx}} \qquad \text{(Eq. 5.4)}$$

where $y(x)$ is normalized emission integral value at given x, the independent variable x is the temperature, A_1 is initial value (left horizontal asymptote), A_2 is the final value (right horizontal asymptote), x_0 is the centre (point of inflection, $x_0 = TQ_{1/2}$) of the sigmoid, and dx is the change in x corresponding to the most significant change in $y(x)$ values. Fittings were performed on normalized emission integral data, therefore, the A_1 and A_2 values were set to 1 and 0, respectively. When fitting the temperature dependent decay constants A_1 was set as the decay constant at the lowest measured temperature and A_2 was set to 0.

Chapter 6. $Ba_2(Zr,Hf)_2Si_3O_{12}:Eu^{2+}$ Blue Emitting Phosphors

6.1. TG/DTA, XRD, and SEM Data Analysis

The TG/DTA curves of $2BaCO_3$-$2ZrO_2$-$3SiO_2$ and $2BaCO_3$-$2HfO_2$-$3SiO_2$ blends are depicted in *Figure 6.1* and *Figure 6.2*, respectively. The TG and DTG curves reveal that the mass loss happens in two steps (at 806 and 896 °C) for Zr derivative. This can be attributed to the decomposition of barium carbonate. Both steps yielded a mass loss of about 11.5%. The calculated mass loss is 10.7%. The assumption of $BaCO_3$ decomposition is supported by DTA curve showing endothermic processes in this temperature range. The TG/DTA curves of Hf derivative (see *Figure 6.2*) are somewhat different from its Zr counterpart. Hf containing sample shows the mass loss only in one step at around 776 °C. This is also attributed to the decomposition of barium carbonate. The measured and calculated mass loss is 8.7 and 7.1%, respectively. The DTA curve shows the endothermic processes in the temperature range of mass loss. It is obvious, that barium carbonate decomposes at lower temperatures in the blend containing HfO_2. However, the origin of this phenomenon is unclear.

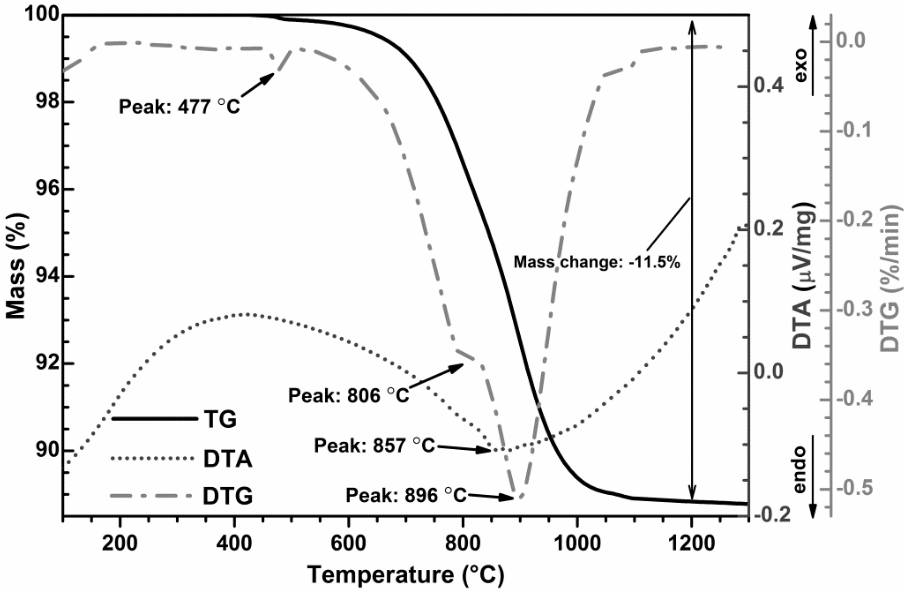

Figure 6.1 *TG/DTA curves of the $2BaCO_3$-$2ZrO_2$-$3SiO_2$ blend.*

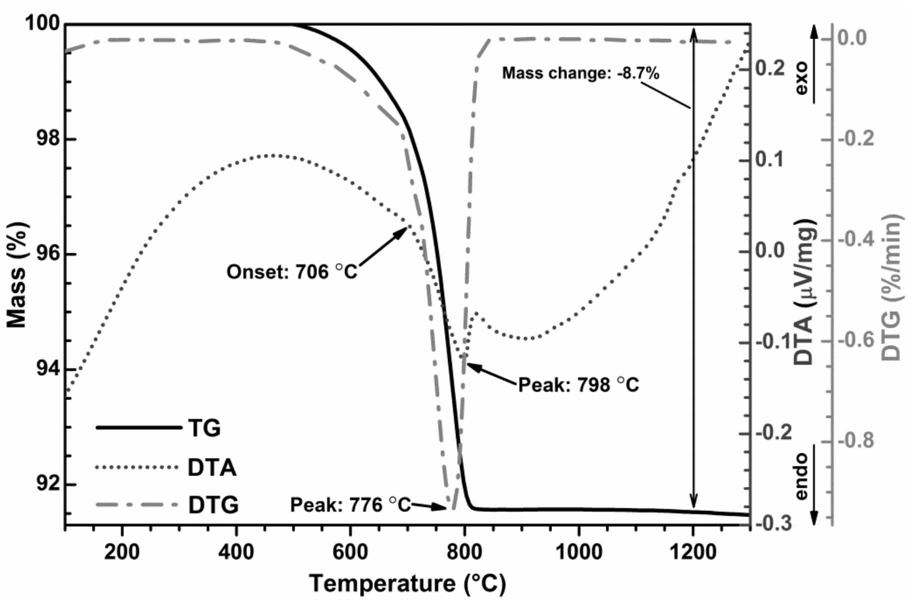

Figure 6.2 *TG/DTA curves of the $2BaCO_3$-$2HfO_2$-$3SiO_2$ blend.*

The XRD patterns of $Ba_2(Zr,Hf)_2Si_3O_{12}$ samples doped with 2 mol-% of Eu^{2+} and sintered at 1450 °C for 5 h under CO atmosphere are shown in *Figure 6.3*. The patterns of synthesized samples match well with the reference pattern of $Ba_2Zr_2Si_3O_{12}$ (PDF4+ (ICDD) 04-002-4880). It was also found out that the solid solutions can be formed at any Zr^{4+}/Hf^{4+} ratio without miscibility gap. This, in fact, is not surprising since the ionic radii of Zr^{4+} and Hf^{4+} in 6-fold coordination are nearly identical, 0.72 and 0.71 Å [158], respectively. It was also observed that the peak $2\theta \approx 19.5°$ intensity increases with increasing Hf^{4+} concentration in the solid solution. This can be explained by the higher X-ray scattering cross section of Hf^{4+} if compared to Zr^{4+} [166].

The particle morphology of the $Ba_2Zr_2Si_3O_{12}$ and $Ba_2Hf_2Si_3O_{12}$ samples sintered at 1450 °C was investigated by taking SEM pictures, which are given in *Figure 6.4*. The particle morphology of both samples is rather similar. The particle size is in the range of 2–5 μm for $Ba_2Zr_2Si_3O_{12}$ specimen. The formation of slightly larger particles was observed for Hf compound. This might be to the lower melting point of $Ba_2Hf_2Si_3O_{12}$.

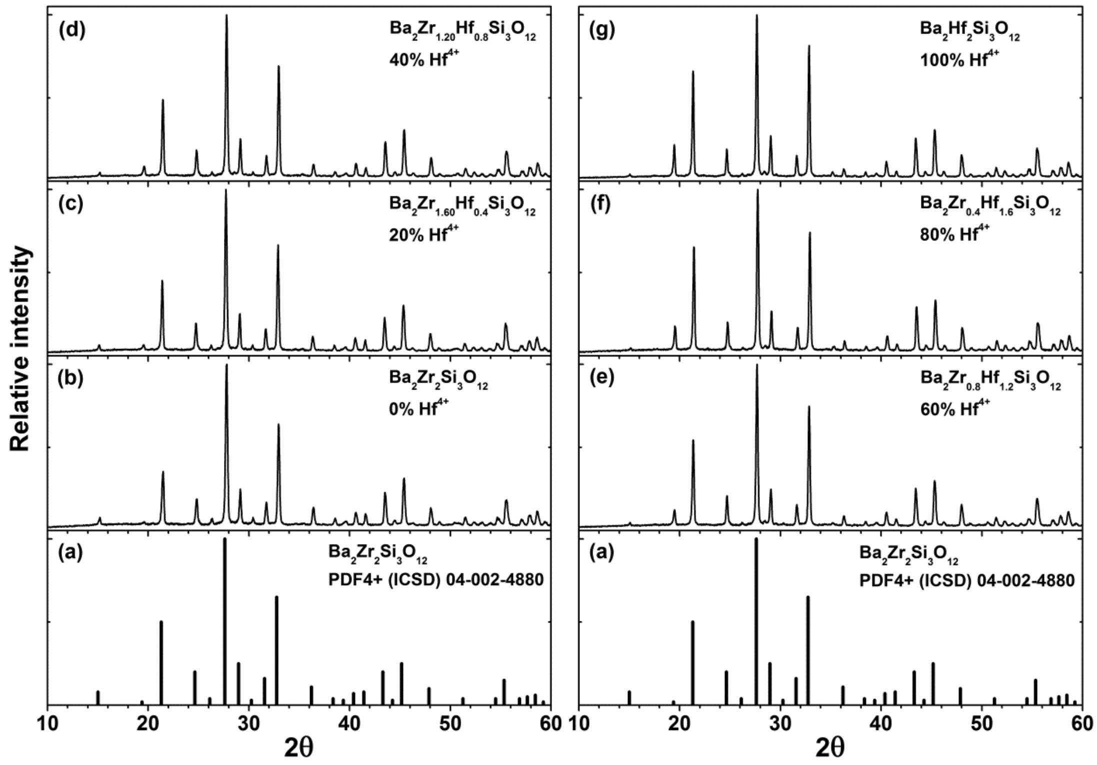

Figure 6.3 *XRD patterns of samples with different Zr/Hf ratios: (a) reference pattern of* $Ba_2Zr_2Si_3O_{12}$*; (b) 0% Hf; (c) 20% Hf; (d) 40% Hf; (e) 60% Hf; (f) 80% Hf; (g) 100% Hf.*

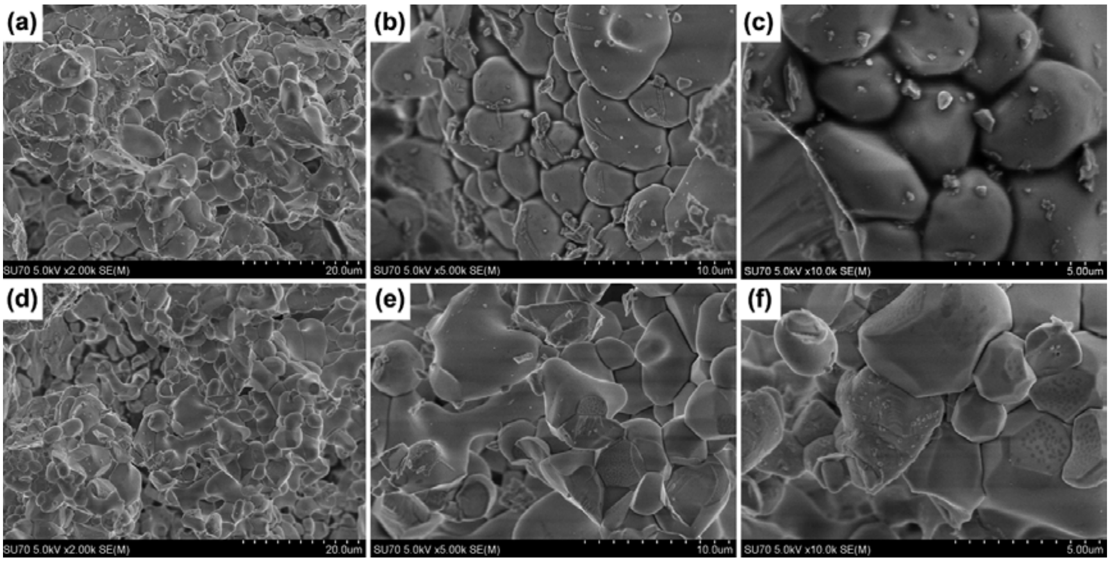

Figure 6.4 *SEM images of* $Ba_2Zr_2Si_3O_{12}$ *sintered at 1450 °C under magnification of (a) ×2.0k, (b) ×5.0k, (c) ×10.0k, and of* $Ba_2Hf_2Si_3O_{12}$ *sintered at 1450 °C (d) ×2.0k, (e) ×5.0k, (f) ×10.0k.*

6.2. Optical Properties

The body colour of undoped samples was white, indicating the absence of absorption in the visible range as shown in Figure 6.5a. The samples containing

Eu^{2+} possessed a yellowish body colour thus indicating absorption in the blue spectral region what is in line with reflection spectra shown in *Figure 6.5b*.

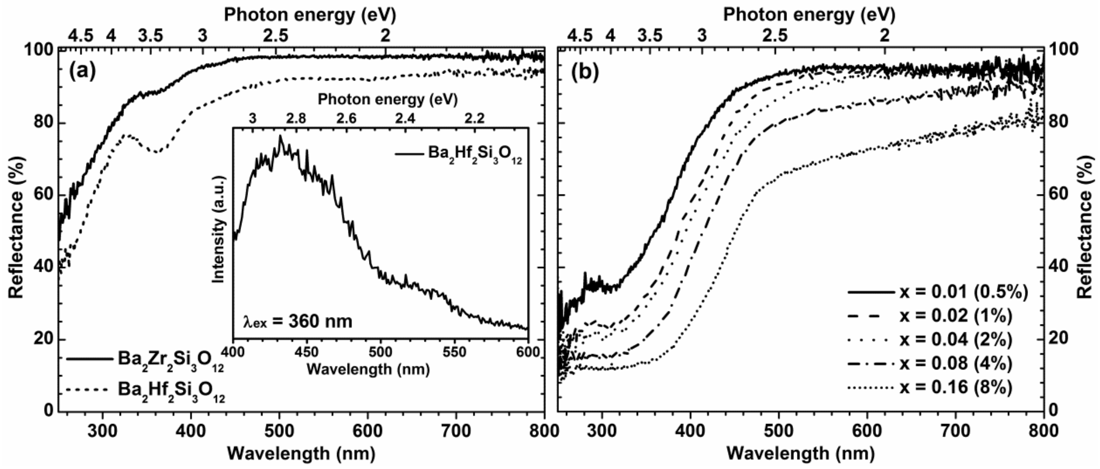

Figure 6.5 *(a) Reflection spectra of undoped $Ba_2Zr_2Si_3O_{12}$ and $Ba_2Hf_2Si_3O_{12}$. Inset shows emission spectrum of $Ba_2Hf_2Si_3O_{12}$ (λ_{ex} = 360 nm). (b) Reflection spectra of $Ba_2Hf_2Si_3O_{12}$ doped with 0.5–8 mol-% of Eu^{2+}.*

Figure 6.5a also shows the increasing absorption at shorter wavelengths (higher energies) of undoped specimens. This can be attributed to the host lattice absorption (band gap). Moreover, the absorption band centred at 360 nm was also observed in the reflection spectrum of $Ba_2Hf_2Si_3O_{12}$. Excitation of the specimen at 360 nm has led to the weak emission band with a maximum around 430 nm. This emission band probably arises from Ti^{4+} impurities which inevitably are present in starting HfO_2 and ZrO_2 materials. However, the absorption band at 360 nm of Zr derivative was much less intense than its Hf counterpart. The similar weak emission was observed when HfO_2 was excited at 160 nm.

Reflection spectra of Eu^{2+} doped samples (*Figure 6.5b*) contain a broad absorption band ranging from 250 to 450 nm and high transmittance at longer wavelengths making target materials interesting for application in near UV emitting pcLEDs. As expected, absorption increases with increasing Eu^{2+} content in the host lattice. However, the transmittance at longer wavelengths decreases following the same trend. This is probably related to the formation of oxygen vacancies due to the reductive synthesis atmosphere and thus colour centre formation, resulting in greyish samples. Furthermore, cluster formation of Eu^{2+} at higher concentrations or segregation of Eu^{2+} for example as EuO is also possible and can explain the decrease in reflectivity, since EuO is dark violet. The absorption band slightly shifted to the shorter wavelengths when Zr^{4+} was substituted by Hf^{4+}.

Excitation spectra of $Ba_2Zr_{2-y}Hf_ySi_3O_{12}$:2%$Eu^{2+}$ are depicted in *Figure 6.6a*. It consist of a structured broad band between 250 and 440 nm attributed to the parity-allowed transitions between the ground state $[Xe]4f^7$ ($^8S_{7/2}$) and the crystal field components of $[Xe]4f^65d^1$ excited state configuration of Eu^{2+} ions. The photoluminescence intensity increased with increasing Hf^{4+} concentration. It is possible that there is a reduced probability of photoionization of the Eu^{2+} ion in the Hf^{4+} containing specimens, since the absorption edge (in the range 160–200 nm) of the Hf^{4+} derivative is at higher energy than Zr^{4+} derivative [167]. The shape of excitation spectra is the same regardless the Zr^{4+}/Hf^{4+} ratio. It turned out that the highest excitation intensity is achieved if the samples are doped with 1 and 2 mol-% of Eu^{2+} for $Ba_2Zr_2Si_3O_{12}$ and $Ba_2Hf_2Si_3O_{12}$, respectively. A further increase of Eu^{2+} concentration resulted in significant decrease in intensity due to concentration quenching.

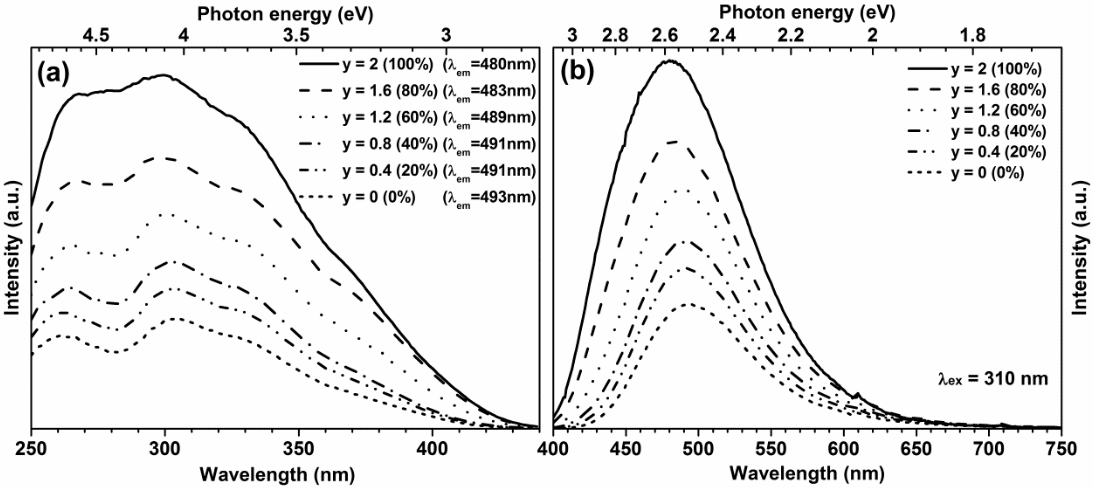

Figure 6.6 *(a) Excitation and (b) emission (λ_{ex} = 310 nm) spectra of $Ba_2Zr_{2-y}Hf_ySi_3O_{12}$:2%$Eu^{2+}$.*

The luminescence of Eu^{2+} activated phosphors originates from the interconfigurational transition between the lowest energy crystal field component of [Xe]$4f^6 5d^1$ excited state and [Xe]$4f^7$ ($^8S_{7/2}$) ground state configuration. Emission spectra of $Ba_2Zr_{2-y}Hf_ySi_3O_{12}$:2%$Eu^{2+}$ phosphor samples as a function of Zr^{4+}/Hf^{4+} ratio in the structure are given in *Figure 6.6b*. It is obvious that emission intensity gradually increases with increasing Hf^{4+} content in the host lattice. Moreover, emission maximum shifts towards the blue spectral range following the same trend (from 493 nm in $Ba_2Zr_2Si_3O_{12}$:2%Eu^{2+} to 480 nm in $Ba_2Hf_2Si_3O_{12}$:2%Eu^{2+}). Furthermore, quantum efficiencies of the phosphors increased with higher Hf^{4+} contents, what could explain the stronger emission intensities for samples containing Hf^{4+} (see *Table 6.1*). Optical measurements also revealed that that emission maximum shifts towards green if more Eu^{2+} is incorporated into the host lattice. This is caused by reabsorption. On the other hand, an increase of Eu^{2+} concentration leads to drop in emission intensity due to concentration quenching. The maximum emission intensity was achieved if samples were doped with 1 and 2 mol-% of Eu^{2+} for $Ba_2Zr_2Si_3O_{12}$ and $Ba_2Zr_2Si_3O_{12}$, respectively. This is in line with excitation spectra discussed earlier. Besides, the traces of Eu^{3+} can still be observed in emission spectra (*Figure 6.6b*) at about 609 nm suggesting about incomplete reduction of europium ions. The higher annealing temperature under N_2/H_2 gas flow might be required for the complete reduction of Eu^{3+} to Eu^{2+}. However, such temperature increase might also result in a higher defect concentration, leading to lower efficiency of the phosphor samples.

The presence of Eu^{3+} in the specimens was confirmed by measuring emission spectra (see *Figure 6.7a*) under VUV excitation (λ_{ex} = 160 nm). The emission spectra consist of a broad band, which maximum shifts towards lower energies with increasing Eu^{2+} concentration, and sharp lines in the range of 580–720 nm, where the Eu^{3+} emission lines are usually located. The intensity of line emission varied randomly with different europium concentration, whereas the intensity of band emission increased with increasing Eu^{2+} concentration. Completely opposite results were obtained if samples were excited at 310 nm, where the maximum of emission intensity was reached if samples were doped with 1 mol-% of Eu^{2+}. Moreover, the emission band peaking at around 330 nm was observed. This band can be attributed to the charge transfer transition of $[HfO_6]^{8-}$ groups. This is in good agreement with the data reported by Schipper et al. [168]. It was also observed that the intensity of $[HfO_6]^{8-}$ charge transfer band decreases with increasing europium concentration suggesting that there might be an energy transfer from $[HfO_6]^{8-}$ groups to Eu^{2+}. This can be found out by comparing emission integrals of $[HfO_6]^{8-}$ groups and Eu^{2+} [167] as a function of europium concentration as shown in *Figure 6.7b* (emission integrals of $[HfO_6]^{8-}$ groups and Eu^{2+} were calculated in the ranges 270–390 nm and 400–580 nm, respectively). It is obvious that lines representing emission integrals are a mirror image of each other, thus confirming the energy transfer from $[HfO_6]^{8-}$ to Eu^{2+}.

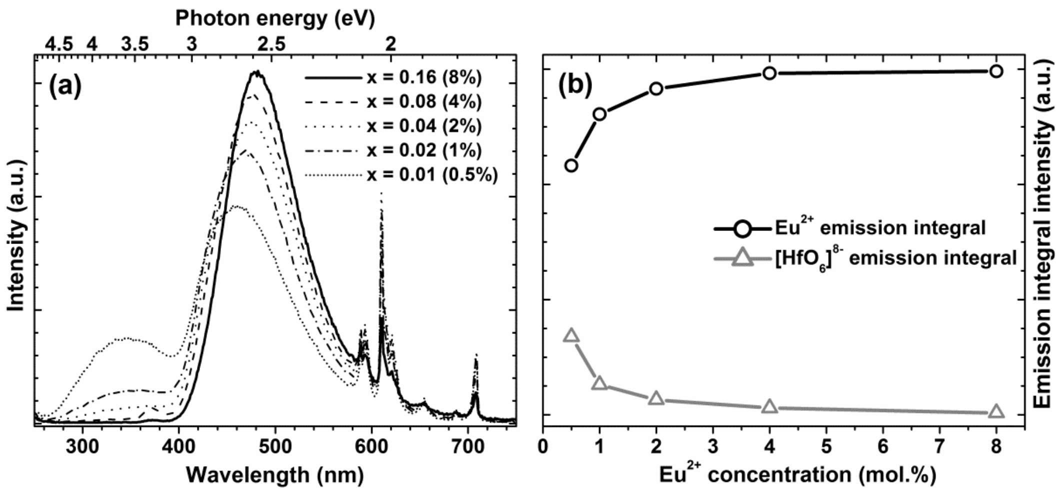

Figure 6.7 *(a) Emission spectra of $Ba_2Hf_2Si_3O_{12}$ doped with 0.5-8% mol-% Eu^{2+} (λ_{ex} = 160 nm). (b) Emission integrals of Eu^{2+} and $[HfO_6]^{8-}$ as a function of Eu^{2+} concentration.*

Coming back to intensive Eu^{3+} line emission under 160 nm excitation there might be several explanations for this phenomenon. One possibility is that $[HfO_6]^{8-}$ transfers some energy to Eu^{3+} like it does to Eu^{2+}. Another possibility is that electron is excited from the valence band to conduction band. Then it can relax either to Eu^{2+} or Eu^{3+} excited states, which finally luminesce. Similar results were recently reported for Pr^{3+} doped garnet phosphors [163]. Both mentioned processes are not possible under 310 nm excitation since the photons possess insufficient energy for $[HfO_6]^{8-}$ group excitation or moving an electron from the valence to the conduction band.

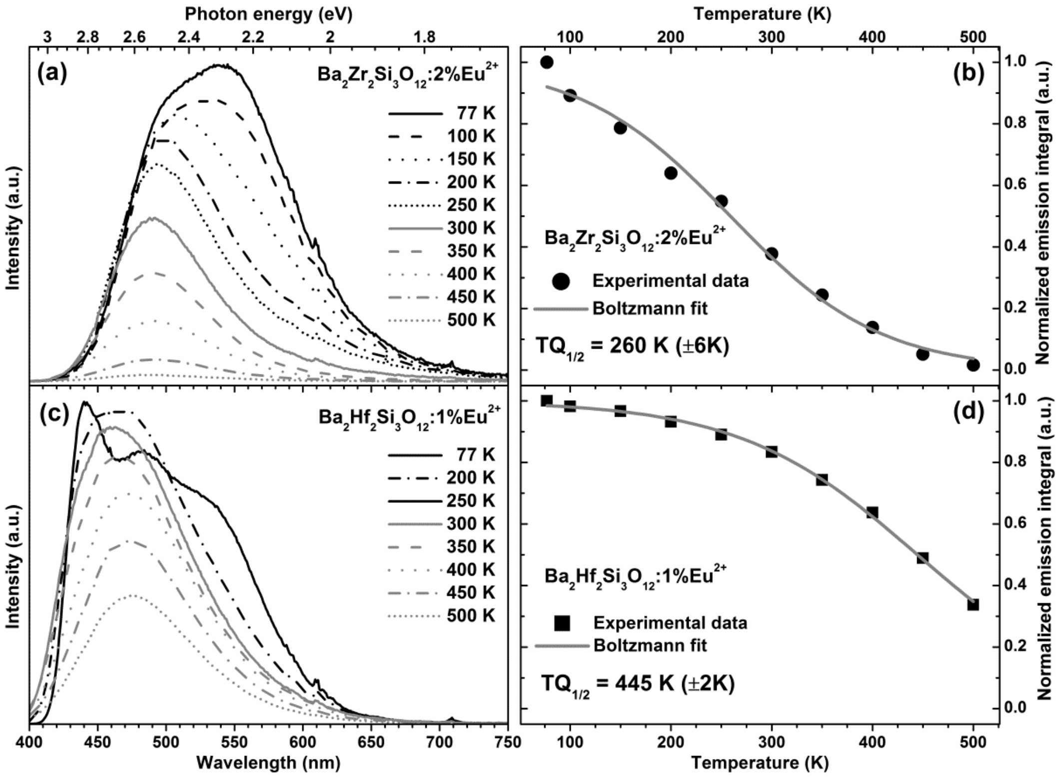

Figure 6.8 *(a) Temperature dependent emission spectra ($\lambda_{ex} = 310$ nm) of $Ba_2Zr_2Si_3O_{12}$:2%Eu^{2+} and its (b) $TQ_{1/2}$ value estimation; (c) temperature dependent emission spectra ($\lambda_{ex} = 310$ nm) of $Ba_2Hf_2Si_3O_{12}$:1%Eu^{2+} and its (d) $TQ_{1/2}$ value estimation.*

Figure 6.8 displays TQ data for $Ba_2Zr_2Si_3O_{12}$:2%Eu^{2+} and $Ba_2Hf_2Si_3O_{12}$:1%Eu^{2+}. Two overlapping emission bands can be observed in the temperature dependent emission spectra (see *Figure 6.8a*) of Zr derivative. It was already discussed in Chapter 4.1 that there are two non-equivalent Ba sites with CN = 9 and CN = 12 in the crystal structure. The emission from Eu^{2+} ions located in nine coordinated site occurs at lower energies (longer wavelengths) than from that located in twelve coordinated site. This is due to stronger crystal field splitting strength generated by smaller coordination polyhedron. It is obvious that low energy emission band is much stronger affected by temperature than its high energy counterpart, i.e. the intensity of both bands decreases with the increasing temperature, but the intensity of the lower energy one decreases much faster. The Boltzmann sigmoidal fit method was employed for the calculation of $TQ_{1/2}$. In fact, two data sets might be applied for the calculation. First is the emission intensity and the second the emission integral. The latter is more preferable since it is proportional to the total light output. Calculations revealed that $Ba_2Zr_2Si_3O_{12}$:2%Eu^{2+} phosphor losses half of its efficiency at around 260 K (≈ −13 °C) if measured from 77 to 500 K (see *Figure 6.8b*).

The TQ behaviour of emission spectra of Hf compound is shown in *Figure 6.8c* and is rather similar to its Zr counterpart. However, at 77 K three emission (λ_{ex} = 310 nm) bands with the maxima at around 440, 470 and 525 nm can be observed whereas emission spectra of the Zr derivative contains only two bands at the same temperature. Since there are only two Ba sites in the host lattice the third band might originate from the exciton. The calculated $TQ_{1/2}$ value for $Ba_2Hf_2Si_3O_{12}$:1%Eu^{2+} specimen (see *Figure 6.8d*) was 445 K (≈ 172 °C) if measured from 77 to 500 K. The estimated $TQ_{1/2}$ value for Hf derivative is much higher if compared to Zr derivative. This indicates that $Ba_2Hf_2Si_3O_{12}$:1%Eu^{2+} possesses better TQ properties and thus is more interesting for possible application in white LEDs.

Luminescence decay curves of Eu^{2+} substituted $Ba_2(Zr,Hf)_2Si_3O_{12}$ were recorded monitoring the wavelength at which maximum emission intensity was observed. The specimens were excited with 375 nm picosecond pulsed laser diode. Since there are two non-equivalent Ba sites in the structure, bi-exponential decay behaviour was expected. The experimental data were fitted by the following function:

$$I(t) = A + B_1 e^{(t/\tau_1)} + B_2 e^{(t/\tau_2)} \qquad (Eq. 6.1)$$

where *I(t)* is an intensity as a given time *t*; *A*, B_1 and B_2 are constants, τ_1 and τ_2 are decay times.

Temperature dependent decay curves of $Ba_2Zr_2Si_3O_{12}$:2%Eu^{2+} and $Ba_2Hf_2Si_3O_{12}$:1%Eu^{2+} are shown in *Figure 6.9a* and *Figure 6.9c*, respectively. The decay curves of Zr derivative become steeper with increasing temperature pointing to the reduction of decay time of Eu^{2+} ions. The shortened decay times usually corresponds to decreased efficiency of the activator ions. These results are in line with temperature dependent emission integrals of $Ba_2Zr_2Si_3O_{12}$:2%Eu^{2+} specimen shown in *Figure 6.8b*, where massive decrease of intensity at elevated temperatures was observed. Furthermore, the decay curves of Hf compound, shown in *Figure 6.9c*, are relatively stable in the given temperature range. Only above 300 K a slight decrease of decay times was observed. However, the corresponding emission integrals, depicted in *Figure 6.8d*, start decreasing already at 100 K. This leads to the conclusion that the quenching process is likely not caused not by reduction of the internal quantum efficiency of Eu^{2+}, but rather some other thermally activated processes, e.g. reabsorption.

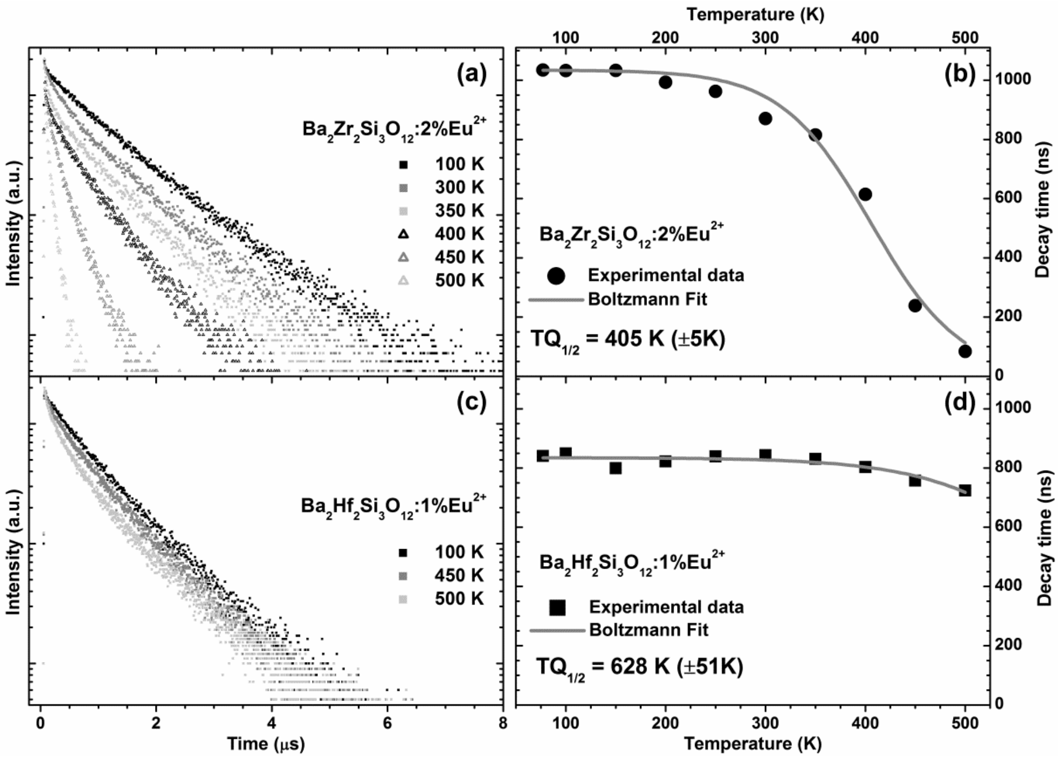

Figure 6.9 *(a) Temperature dependent decay curves (λ_{ex} = 375 nm) of $Ba_2Zr_2Si_3O_{12}$:2%Eu^{2+} and its (b) $TQ_{1/2}$ value estimation; (c) temperature dependent decay curves (λ_{ex} = 375 nm) of $Ba_2Hf_2Si_3O_{12}$:1%Eu^{2+} and its (d) $TQ_{1/2}$ value estimation.*

The RT decay curve fitting data of some selected samples are tabulated in *Table 6.1*. The first component does not originate from Eu^{2+} because it is too fast. The typical Eu^{2+} decay times are usually in the range of 0.5 to 10 μs [169]. The second (main) component (~1 μs) falls well in the typical range of Eu^{2+} decay time. Surprisingly, the slower component became faster with higher Hf^{4+}

concentration. However, this is not in line with quantum efficiencies, where efficiency increased with higher Hf^{4+} concentration. This can be explained as follows; the probability of radiative decay is proportional to the cube of the frequency of emission [170]. The lifetime in entirely Zr^{4+} and Hf^{4+} compounds is 0.974 and 0.903 μs, respectively, what gives a ratio of 1.07. The emission maxima of Zr^{4+} and Hf^{4+} derivatives are 493 and 480 nm, respectively, giving the cube (of emission frequency) ratio of 1.08. This matches well with the expectations from decay ratio (1.07).

Table 6.1 *Fitting parameters of the decay curves (λ_{ex} = 375 nm) of $Ba_{2-x}Eu_xZr_{2-y}Hf_ySi_3O_{12}$ samples and their quantum efficiencies (λ_{ex} = 310 nm).*

$Ba_{2-x}Eu_xZr_{2-y}Hf_ySi_3O_{12}$		**τ_1 (ns)**	**Rel.% (τ_1)**	**τ_2 (ns)**	**Rel.% (τ_2)**	**QE (%)**
x	**y**					
0.04	0	188	15	974	85	13
	0.4	176	13	959	87	16
	0.8	150	10	945	90	20
	1.2	234	16	968	84	26
	1.6	272	18	925	82	33
	2	367	22	909	78	51
0.01	2	421	34	933	66	62
0.02		411	27	937	73	56
0.04		367	22	909	78	51
0.08		405	25	923	75	43
0.16		405	20	897	80	36

The colour points and luminous efficacies of $Ba_{2-x}Eu_xZr_{2-y}Hf_ySi_3O_{12}$ phosphors were studied as a function of Hf^{4+} and Eu^{2+} concentration. The obtained data is summarized in *Table 6.2*. The colour points of synthesized samples are located in the cyan-blue region of the CIE 1931 chromaticity diagram as shown in *Figure 6.10a*. It is evident that coordinates *x* and *y* decrease if Hf^{4+} concentration is increased thus indicating the blue shift of emission. This goes hand in hand with emission spectra depicted in *Figure 6.6b* and emission maxima data given in *Table 6.2*. LE values also decrease following the same trend. This can be explained by smaller overlap of human eye sensitivity curve (maximum at 555 nm [164, 171]) and emission spectra if the latter shifts towards blue region. Furthermore, LE values increase considerably if samples possess higher Eu^{2+} concentration. Once again this is related with the shift of emission maxima towards green spectral region where the human eye sensitivity is higher.

Table 6.2 *CIE 1931 colour points, luminous efficacies and emission maxima of* $Ba_{2-x}Eu_xZr_{2-y}Hf_ySi_3O_{12}$ *samples as a function of* Hf^{4+} *and* Eu^{2+} *concentration.*

$Ba_{2-x}Eu_xZr_{2-y}Hf_ySi_3O_{12}$		Colour coordinate		LE (lm/W_{opt})	λ_{em} (max) (nm)
x	y	x	y		
0.04	0	0.204	0.386	305	493
	0.4	0.201	0.366	294	491
	0.8	0.199	0.355	288	491
	1.2	0.194	0.330	274	489
	1.6	0.192	0.296	253	483
	2	0.183	0.276	240	480
0.01	2	0.179	0.230	205	462
0.02		0.181	0.246	218	472
0.04		0.183	0.276	240	480
0.08		0.190	0.290	250	481
0.16		0.194	0.319	267	485

Figure 6.10a reveals that the blend of $Ba_{2-x}Eu_xZr_{2-y}Hf_ySi_3O_{12}$ and YAG:Ce phosphors would not result in white light at any mixing ratio, because the line connecting colour points of these phosphors does not cross BBL. However, employing some orange or orange-red emitting phosphor instead of YAG:Ce would allow to produce white light. On the other hand, the CRI value of such light source probably would be poor due to the lack of intensity in green spectral region; therefore, an additional green phosphor would be required to compensate it.

One of the critical requirements for LED phosphors is good colour point stability. *Figure 6.10b* depicts the colour points of $Ba_2Zr_2Si_3O_{12}$:2%Eu^{2+} and $Ba_2Hf_2Si_3O_{12}$:1%Eu^{2+} samples as a function of temperature. The colour points of Zr derivative shows a strong dependence on temperature in the range of 100−300 K as was anticipated from the temperature dependent emission spectra as shown in *Figure 6.8a*. However, at temperatures 300–500 K the colour points are rather stable, but as discussed above, the efficiency of the phosphor is quite low at elevated temperatures, what is a bottleneck for practical application. The Hf derivative shows much more stable colour points in the range of 100–500 K, and thus is more suitable for practical application.

It also possesses much higher $TQ_{1/2}$ and QE values as shown in *Figure 6.8d* and *Table 6.1*, respectively, if compared to its Zr counterpart.

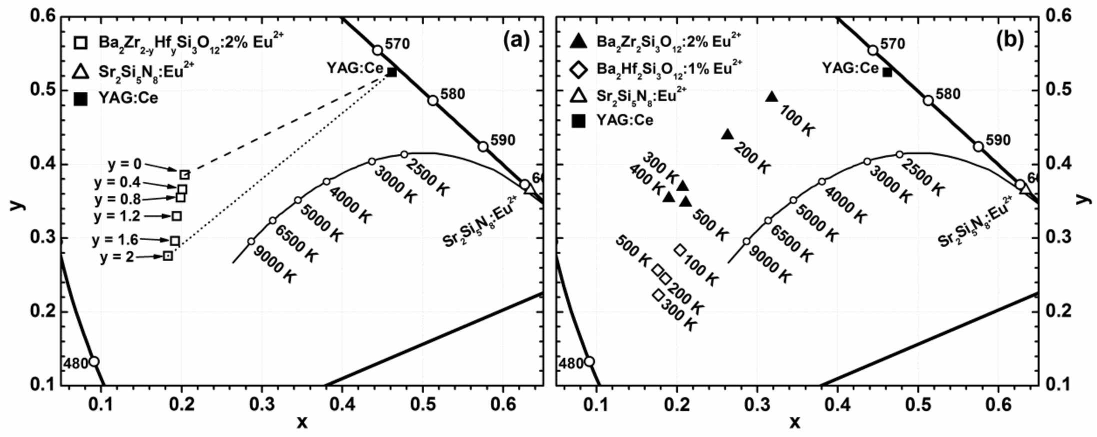

Figure 6.10 *Sections of the CIE 1931 colour diagram with colour points of (a)* $Ba_2Zr_{2-y}Hf_ySi_3O_{12}$*:2%*$Eu^{2+}$ *and (b)* $Ba_2Zr_2Si_3O_{12}$*:2%*Eu^{2+} *and* $Ba_2Hf_2Si_3O_{12}$*:1%*Eu^{2+} *as a function of temperature. Colour points of YAG:Ce [53] and* $Sr_2Si_5N_8$*:*Eu^{2+} *[172] are given for reference.*

Chapter 7. $Li_3Ba_2La_3(MoO_4)_8:Eu^{3+}$ Red Emitting Phosphors

7.1. TG/DTA, XRD, and SEM Data Analysis

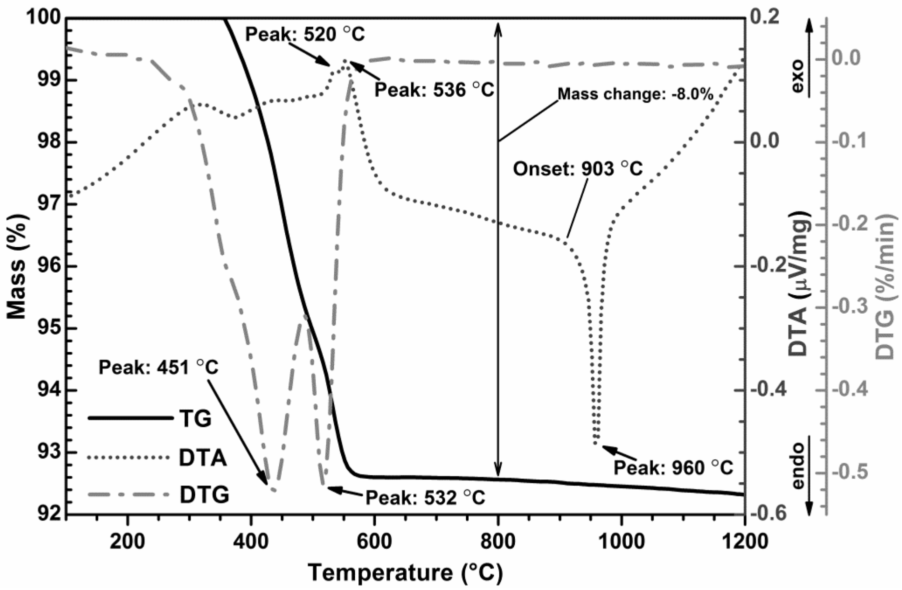

Figure 7.1 *TG/DTA curves of the $3Li_2CO_3$-$4BaCO_3$-$3La_2O_3$-$16MoO_3$ blend.*

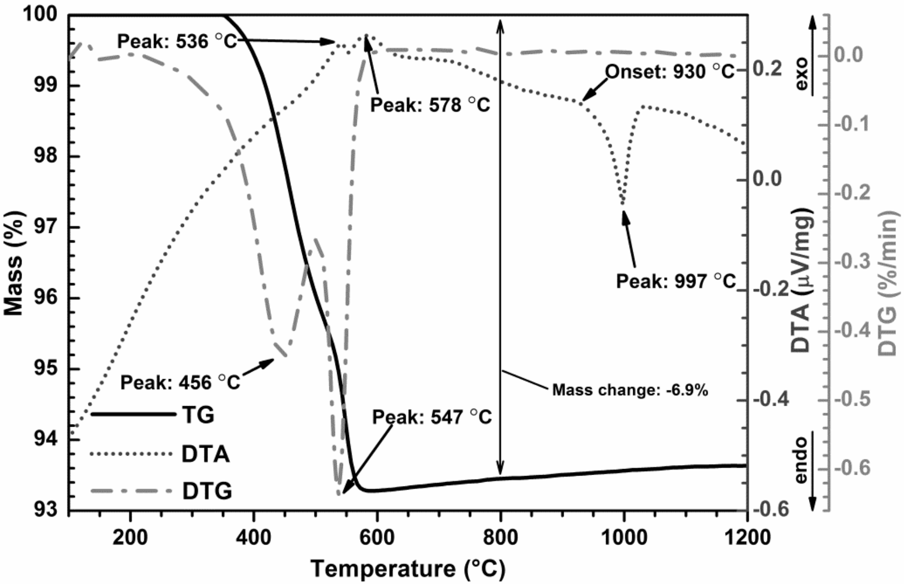

Figure 7.2 *TG/DTA curves of the $3Li_2CO_3$-$4BaCO_3$-$3Eu_2O_3$-$16MoO_3$ blend.*

The TG/DTA curves of the starting materials blend for $Li_3Ba_2La_3(MoO_4)_8$ and $Li_3Ba_2Eu_3(MoO_4)_8$ compounds are depicted in *Figure 7.1* and *Figure 7.2*, respectively. The TG and DTG reveal that mass loss happens in two steps for both lanthanum (at 451 and 532 °C) and europium (at 456 and 547 °C) derivatives. This can be attributed to the decomposition of lithium and barium carbonates. For lanthanum compound both steps yielded a mass loss of about

8.0% which is close to the calculated mass loss of 7.2%. For europium derivative both steps yielded a mass loss of about 6.9% and this value is in good agreement with the calculated one – 7.0%. However, the decomposition of lithium and barium carbonates occurs at much lower temperatures then reported in the literature [173], about 700 and 1000 °C, respectively. The DTA curves reveal that the melting point of $Li_3Ba_2La_3(MoO_4)_8$ and $Li_3Ba_2Eu_3(MoO_4)_8$ is 960 and 997 °C, respectively. The melting point of $Li_3Ba_2La_3(MoO_4)_8$ is about 40 °C lower than reported by M. Song et al. (999 °C) [174]. However, reported value was obtained for the single crystal of $Li_3Ba_2La_3(MoO_4)_8$. The melting point depends on the particle size and, in general, decreases with decreasing particle size due to the higher chemical potential of the surface ions [175, 176].

The XRD patterns of $Li_3Ba_2La_{3-x}Eu_x(MoO_4)_8$ as a function of Eu concentration are depicted in *Figure 7.3*. The patterns of synthesized samples match well with the reference pattern of $Li_3Ba_2Gd_3(MoO_4)_8$ (PDF2 (ICSD) 00-077-0830) and patterns of isostructural compounds reported in the literature [75, 177, 178]. The XRD measurements revealed that solid solutions are formed at any La^{3+}/Eu^{3+} ratio without miscibility gap. This in line with Vegard’s Law which state that in order to form a solid solution the cations of two compounds must have ionic radii within ±15% of each other [164]. The ionic radius of La^{3+} and Eu^{3+} for CN = 8 is 1.16 and 1.066 Å, respectively [158].

The morphology of the $Li_3Ba_2La_3(MoO_4)_8$, $Li_3Ba_2La_{1.5}Eu_{1.5}(MoO_4)_8$ and $Li_3Ba_2Eu_3(MoO_4)_8$ phosphor powders was inspected by taking SEM pictures. The obtained SEM images are depicted in *Figure 7.4*. The morphologies show rather large (3–5 μm) agglomerated particles with irregular shape and surrounded by smaller (~500 nm) particles. However, no significant differences were observed in the SEM pictures for the samples with different Eu^{3+} concentration. The obtained relatively large particles at rather low sintering temperature can be explained by high Li content in the structure, which promotes particle growth [179].

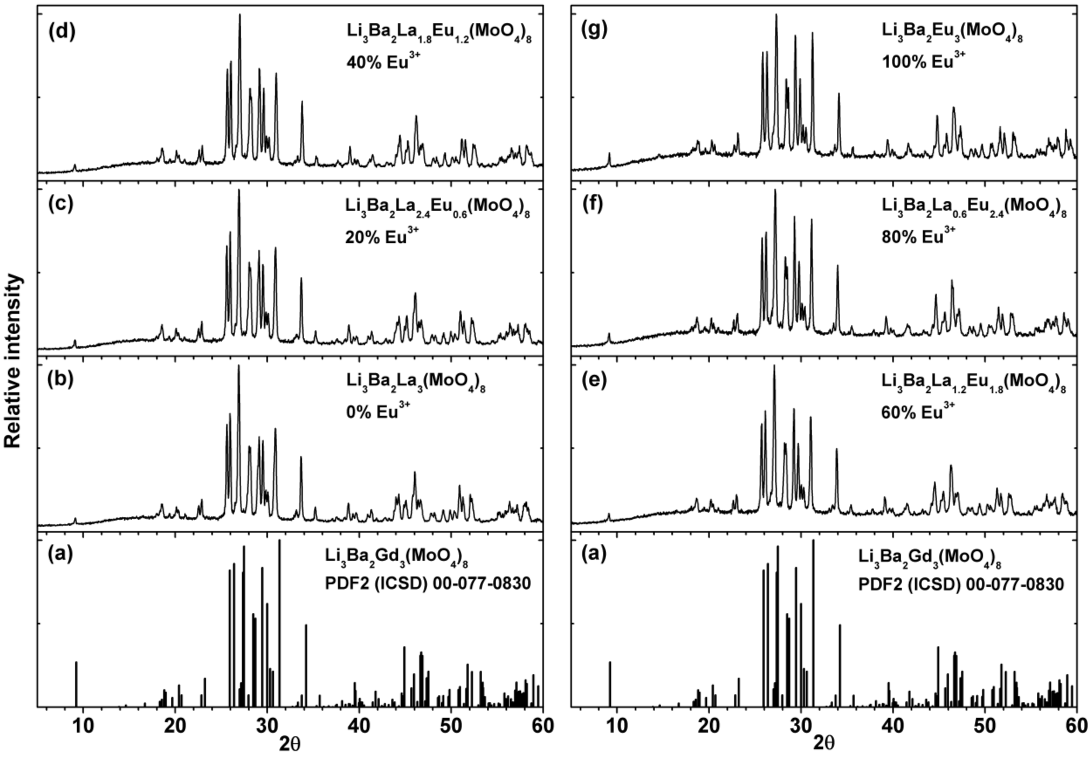

Figure 7.3 *XRD patterns of* $Li_3Ba_2La_3(MoO_4)_8$*:*Eu^{3+} *samples with different* Eu^{3+} *concentrations: (a) reference pattern of* $Li_3Ba_2Gd_3(MoO_4)_8$*; (b) 0%* Eu^{3+}*; (c) 20%* Eu^{3+}*; (d) 40%* Eu^{3+}*; (e) 60%* Eu^{3+}*; (f) 80%* Eu^{3+}*; (g) 100%* Eu^{3+}*.*

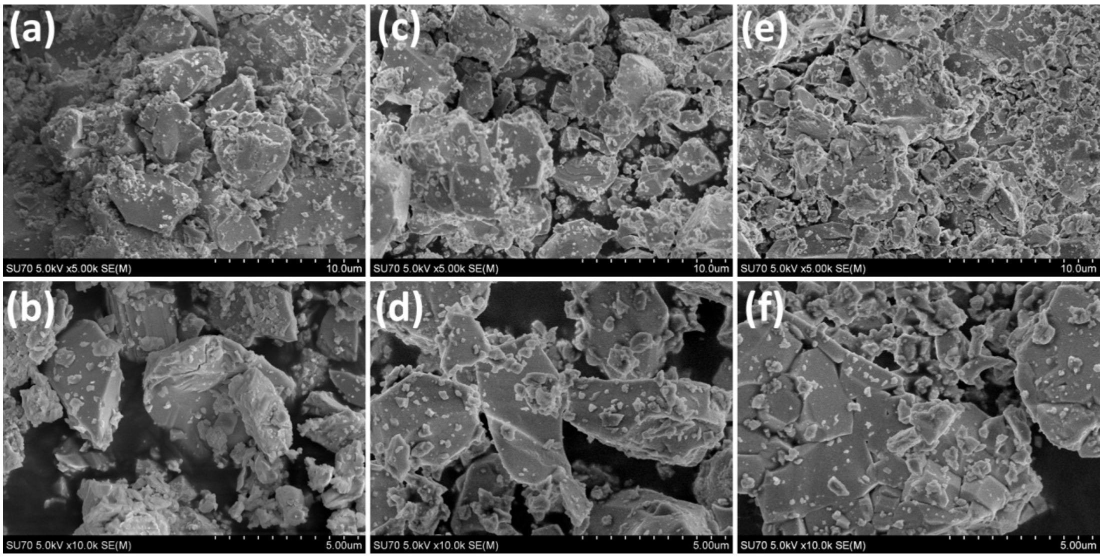

Figure 7.4 *SEM pictures of* $Li_3Ba_2La_3(MoO_4)_8$ *under magnification of (a) ×5.0k and (b) ×10.0k;* $Li_3Ba_2La_{1.5}Eu_{1.5}(MoO_4)_8$ *(c) ×5.0k and (d) 10.0k;* $Li_3Ba_2Eu_3(MoO_4)_8$ *(e) ×5.0k and (f) ×10.0k.*

7.2. Optical Properties

The body colour of $Li_3Ba_2La_3(MoO_4)_8$ was white, indicating the absence of absorption in the visible range as depicted in *Figure 7.5*. The optical band gap of the undoped material, derived from the turning point of the absorption edge in the reflection spectrum, was around 340 nm (3.65 eV). The optical band gap decreased upon substitution of La^{3+} by Eu^{3+}, and was around 344 nm (3.60 eV) for $Li_3Ba_2Eu_3(MoO_4)_8$ sample. Those samples containing a high concentration of Eu^{3+} possessed a moderate reddish body colour due to some absorption in the blue-violet spectral range causing Eu^{3+} luminescence, what is in line with reflection spectra shown in *Figure 7.5*. The strength of Eu^{3+} line absorption increased with the concentration and was strongest when all lanthanum was replaced by europium. The reflection spectrum of $Li_3Ba_2Eu_3(MoO_4)_8$ consists of typical Eu^{3+} absorption lines originating from the $^7F_0 \rightarrow {}^5D_J$, $^7F_0 \rightarrow {}^5L_J$ and $^7F_0 \rightarrow {}^5G_J$ transitions [65, 178, 180-183]. The broad band absorption in the range 250–360 nm can be attributed to the optical band gap of $Li_3Ba_2Eu_3(MoO_4)_8$.

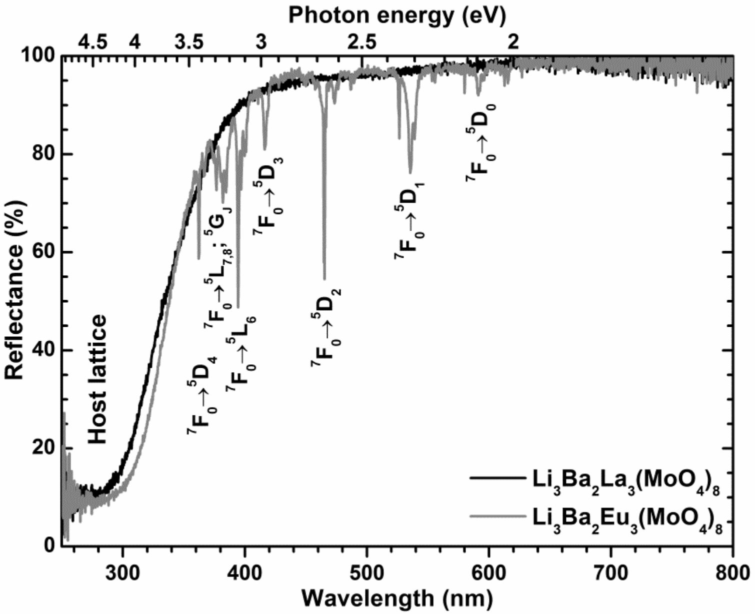

Figure 7.5 *Reflection spectra of* $Li_3Ba_2La_3(MoO_4)_8$ *and* $Li_3Ba_2Eu_3(MoO_4)_8$.

Figure 7.6a shows excitation spectra of samples doped with 10 and 100% Eu^{3+} monitoring the emission at 615.5 nm ($^5D_0 \rightarrow {}^7F_2$ transition). The band located between 250 and 350 nm can be attributed to the CT from $[MoO_4]^{2-}$

groups to Eu^{3+}. It shows broadening and a slight red-shift with increasing Eu^{3+} content and the overall intensity increases by a factor of around 2.5. The red shift of the CT band is caused by the decreasing size of Eu^{3+} site, when substituting La^{3+} by smaller Eu^{3+}. This results in the shorter Eu–O bonds, which eases the charge transfer. There are several sets of lines in the range of 350–600 nm which are associated with the typical intraconfigurational $[Xe]4f^6$ transitions of Eu^{3+}. Lines originating from $^7F_0 \rightarrow {}^5L_6$ and $^7F_0 \rightarrow {}^5D_2$ transitions are located at 395 and 465 nm, respectively, and are of the special interest. The spectral position of these lines match well with the emission spectra of near-UV and blue LEDs, respectively, thus making the synthesized phosphors suitable for solid state light sources. Moreover, it should be noted that the intensity ratio between the $^7F_0 \rightarrow {}^5L_6$ and the $^7F_0 \rightarrow {}^5L_J$, ^5G_J is much different between the 10% and the 100% doped sample. We assume that the $^7F_0 \rightarrow {}^5L_J$, ^5G_J transitions become more probable due to the broadening of the CT-level with increasing Eu^{3+} concentration and thus the admixing of the CT-level with those excited terms of the $[Xe]4f^6$ ground state configuration, which are energy wise close to the CT state.

The emission spectra of $Li_3Ba_2La_3(MoO_4)_8:Eu^{3+}$ samples doped with 10% and 100% of Eu^{3+} under 465 nm excitation are depicted in *Figure 7.6b*. The strongest emission lines located at 612.5 and 615.5 nm are attributed to the $^5D_0 \rightarrow {}^7F_2$ transition. The intensity of lines originating from $^5D_0 \rightarrow {}^7F_1$ (≈ 595 nm), $^5D_0 \rightarrow {}^7F_3$ (≈ 655 nm) and $^5D_0 \rightarrow {}^7F_4$ (≈ 705 nm) is much weaker if compared to $^5D_0 \rightarrow {}^7F_2$ transition. The $^5D_0 \rightarrow {}^7F_2$ is ED transition [137, 171], which requires a lower symmetry onto the respective Eu^{3+} sites.

The intensity of different $[Xe]4f^6 \rightarrow [Xe]4f^6$ transitions of Eu^{3+} depends on the local environment of europium ion. Therefore, more insight into possible change of Eu^{3+} structural surrounding can be gained by calculating the ratio of integrated emission intensities of $^5D_0 \rightarrow {}^7F_2$ and $^5D_0 \rightarrow {}^7F_1$ transitions [184]. The $(^5D_0 \rightarrow {}^7F_2)/(^5D_0 \rightarrow {}^7F_1)$ ratio is called the asymmetry ratio and gives a measure of the degree of distortion from the inversion symmetry of the local environment of the Eu^{3+} ion in the lattice [178, 185-187]. The asymmetry ratios as a function of Eu^{3+} concentration and as a function of temperature of $Li_3Ba_2Eu_3(MoO_4)_8$ sample are presented in *Figure 7.7*. The asymmetry ratio increased from 10.5 to 11.8 when Eu^{3+} concentration was raised from 10% to 100%. Furthermore, the ratio decreased from 11.8 to 10.4 when the temperature of $Li_3Ba_2Eu_3(MoO_4)_8$ was increased from 100 to 500 K. However, the obtained asymmetry ratio values are higher than 8.1 as was reported for the $Li_3Ba_2Gd_3(MoO_4)_8:Eu^{3+}$ compounds by Chang et al. [178]. It was assumed that the ratio of the occupation of Eu^{3+} onto the two different sites is a function of Eu^{3+} concentration, i.e. for low Eu^{3+} concentrations the activator is first incorporated onto the 8-fold coordinated site, because this site better to the ionic radius of Eu^{3+}. Furthermore, it was assumed that the 10-fold coordinated site has a lower local symmetry and, therefore, a higher asymmetry ratio for the Eu^{3+} emission spectrum is expected. This explains the increase of the symmetry ratio with increasing the Eu^{3+} concentration. For the observation of a decreasing asymmetry ratio of the $Li_3Ba_2Eu_3(MoO_4)_8$ compound with increasing temperature two different mechanisms can be considered. It can either be attributed to energy transfer between the two Eu^{3+} sites or to a different dependence of thermal quenching of the $^5D_0$ state via the CT state. Since no difference of the location of the $^5D_0$ state has been observed in the emission spectrum, it is more likely that the 10-fold Eu^{3+} site shows stronger TQ, which is in line with the larger expected relaxation for this crystallographic site.

The inset of *Figure 7.6b* shows emission integrals of $Li_3Ba_2La_3(MoO_4)_8:Eu^{3+}$ samples as a function of Eu^{3+} concentration. It was found out that emission integrals increase with the increasing Eu^{3+} concentration and reaches maximum at 90% doping level. The sample doped with 100% of Eu^{3+} showed slightly weaker emission indicating possible concentration quenching. However, the obtained results differ from that published by Guo et al. [75] and Chang et al. [178] who reported the concentration quenching in $Li_3Ba_2Gd_3(MoO_4)_8:Eu^{3+}$ phosphors occurring at 6.7% and 80% of Eu^{3+} concentration, respectively. The reason for such mismatch is unclear. It might be that the optical properties of $Li_3Ba_2Gd_3(MoO_4)_8$:Eu^{3+} are greatly influenced by the preparation method and/or synthesis temperature/time. The replacement of Gd^{3+} ions by larger La^{3+} ions also might have some impact on luminescent properties of the material.

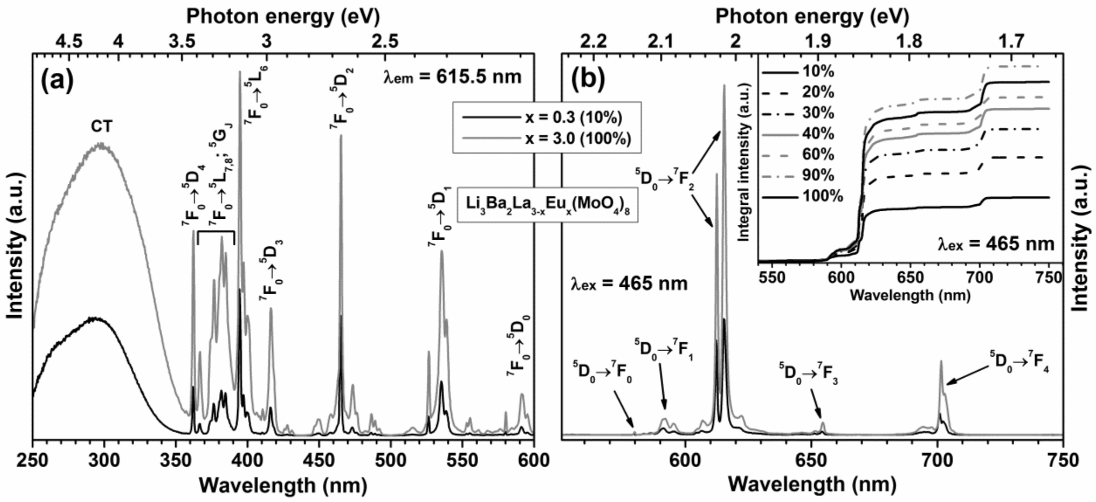

Figure 7.6 *(a) Excitation (λ_{em} = 615.5 nm) and (b) emission (λ_{ex} = 465 nm) spectra of $Li_3Ba_2La_3(MoO_4)_8$:Eu^{3+} doped with 10% and 100% of Eu^{3+}. Inset shows emission (λ_{ex} = 465 nm) integral intensity as a function of Eu^{3+} concentration.*

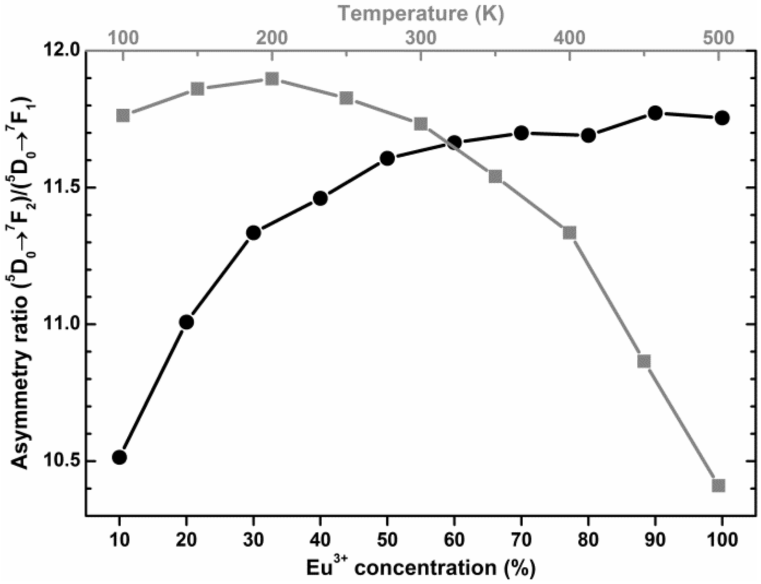

Figure 7.7 *Asymmetry ratios as a function of Eu^{3+} concentration (black line) and as a function of temperature of $Li_3Ba_2Eu_3(MoO_4)_8$ sample (grey line).*

The temperature dependent emission spectra (λ_{ex} = 465 nm) of 20% and 100% of Eu^{3+} doped specimens are depicted in *Figure 7.8a* and *Figure 7.8c*, respectively. The emission intensity decreases at elevated temperatures roughly by the factor of 4.5 for both given Eu^{3+} concentrations. However, the decrease of emission integrals was not that strong as could be evaluated from the data presented in *Figure 7.8b* and *Figure 7.8d* for 20% and 100% doped samples, respectively. The much slower decrease of emission integrals at increased temperatures can be explained by broadening of emission lines due to stronger electron–phonon interaction at higher temperatures. The line broadening compensates the decrease of emission intensity to some extent. Therefore, the decrease of the total light output (emission integral) is not that distinct. A Boltzmann sigmoidal fit was employed for the calculation of the $TQ_{1/2}$ values. The results showed that 20% and 100% doped samples lose half of the efficiency at 478 K (205 °C) and 515 K (242 °C), respectively. This indicates that the specimen doped with 100% of Eu^{3+} (namely, $Li_3Ba_2Eu_3(MoO_4)_8$) is more interesting for application in LEDs. Furthermore, the absorption of 100% of Eu^{3+} doped phosphor is much higher than its 20% doped counterpart, what is another plus for the former one.

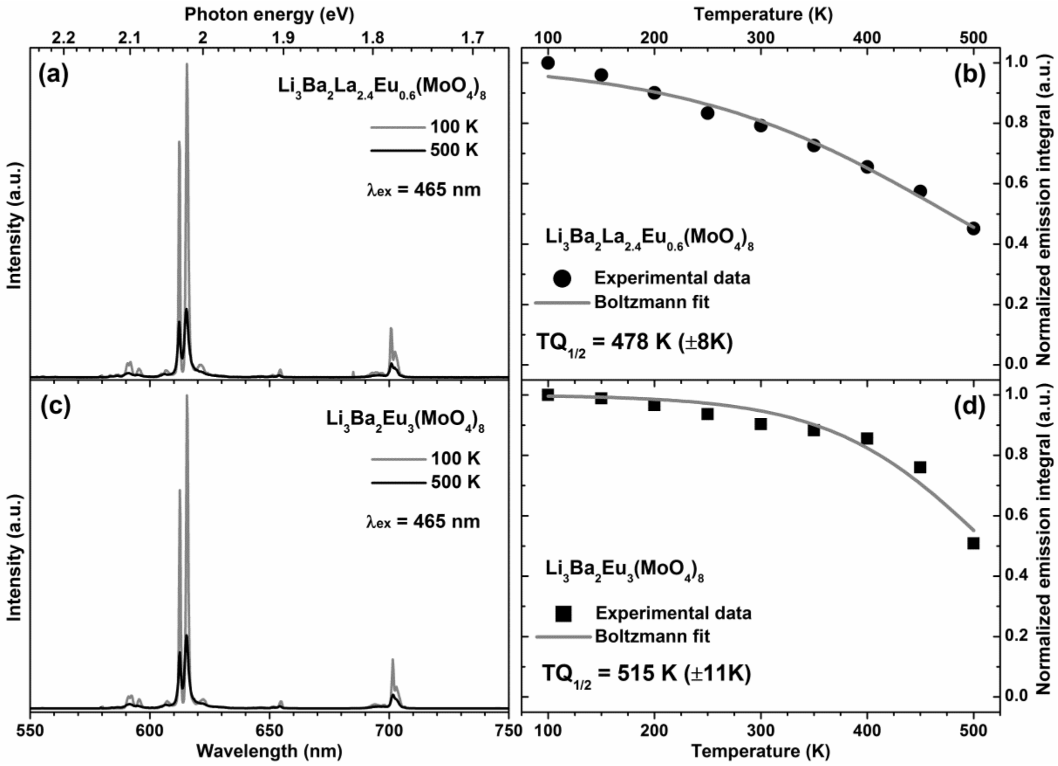

Figure 7.8 *Temperature dependent emission spectra ($\lambda_{ex} = 310$ nm) of $Li_3Ba_2La_3(MoO_4)_8$:Eu^{3+} samples (a) doped with 20% Eu^{3+} and its (b) $TQ_{1/2}$ value estimation; (c) doped with 100% Eu^{3+} and its (d) $TQ_{1/2}$ value estimation.*

Figure 7.9a and *Figure 7.9c* show temperature dependent decay curves of 20% and 100% Eu^{3+} doped samples, respectively, when excited at 465 nm. All decay curves were fitted by a single exponential decay $I(t) = I_0 \cdot exp(-t/\tau)$, where $I(t)$ is intensity at a given time t, I_0 is the initial intensity, and τ is a lifetime [178]. It is obvious that decay times get shorter with increasing temperature. The same was observed for the Eu^{3+} concentration increase, i.e. decay time became shorted at larger Eu^{3+} content in the structure. *Figure 7.9b* and *Figure 7.9d* represent the calculated decay times as a function of temperature for 20% and 100% of Eu^{3+} doped samples, respectively. The decay times of sample doped with 100% of Eu^{3+} are shorter; however, the scale was left the same as for 20% of Eu^{3+} doped sample for better comparison. In both cases decay times decrease with increasing temperature.

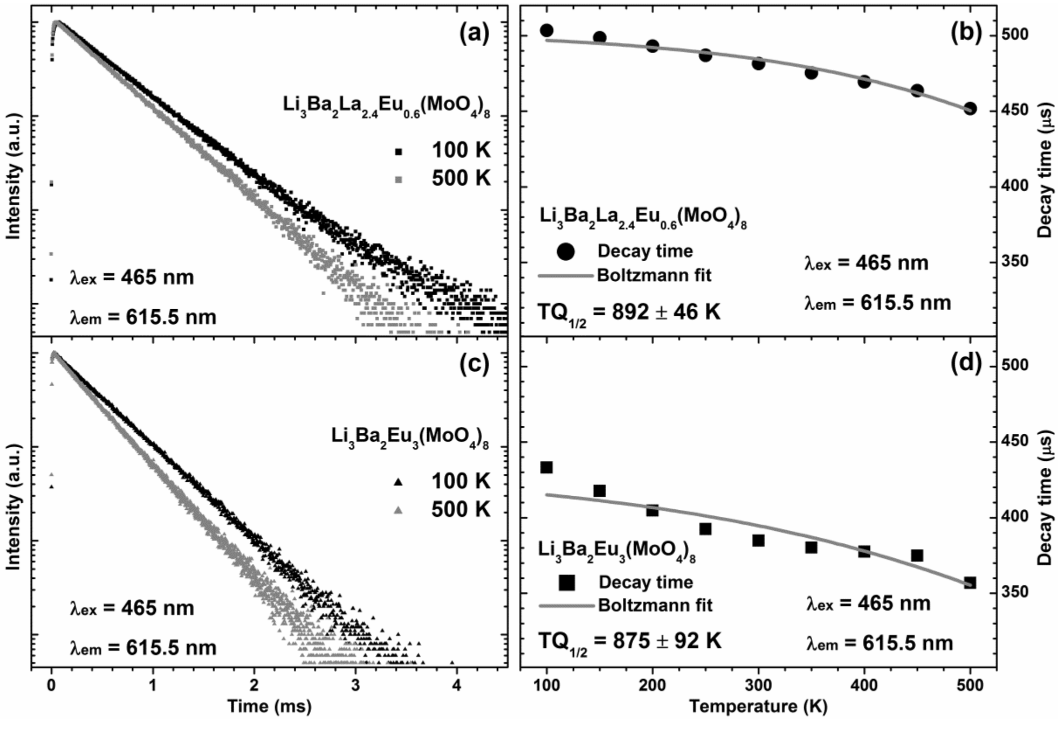

Figure 7.9 *Temperature dependent decay curves* (λ_{ex} = *465 nm) of* $Li_3Ba_2La_3(MoO_4)_8{:}Eu^{3+}$ *samples (a) doped with 20%* Eu^{3+} *and its (b)* $TQ_{1/2}$ *value estimation; (c) doped with 100%* Eu^{3+} *and its (d)* $TQ_{1/2}$ *value estimation.*

The calculated decay times for wider range of Eu^{3+} concentration are summarized in *Table 7.1* and it can be concluded that decay times of Eu^{3+} in $Li_3Ba_2La_3(MoO_4)_8$ host lattice decreases with increasing both temperature and/or Eu^{3+} concentration. Unfortunately, the estimation of $TQ_{1/2}$ from temperature dependent decay times employing Boltzmann fit resulted in values with great error. The high error is due to the fact that the curve does not overpass the turning point (half of the value at low temperature in this case). However, it is evident that decay times decrease slower than emission integrals when temperature increases. This leads to the conclusion that internal efficiency of the phosphors decreases much slower than external efficiency.

Table 7.1 *Decay constants (λ_{ex} = 465 nm) of $Li_3Ba_2La_3(MoO_4)_8$:Eu^{3+} phosphors as a function temperature and Eu^{3+} concentration.*

T (K)	$Li_3Ba_2La_3(MoO_4)_8$:Eu^{3+} decay time (μs)				
	20% Eu^{3+}	40% Eu^{3+}	60% Eu^{3+}	80% Eu^{3+}	100% Eu^{3+}
100	504	488	487	457	433
150	499	485	487	450	418
200	493	481	482	442	405
250	487	477	479	438	392
300	482	473	472	433	384
350	475	467	467	430	380
400	470	461	461	422	377
450	464	455	453	423	375
500	452	442	437	394	357

Figure 7.10 shows that the decay time is not dependent on the excitation channel ($^7F_0 \rightarrow {}^5D_2$, $^7F_0 \rightarrow {}^5D_2$, or LMCT (ligand to metal charge transfer)). This proves that after excitation into the different excited levels of Eu^{3+}, a fast non-radiative decay to the $^5D_0$ - level, which then emits, occurs.

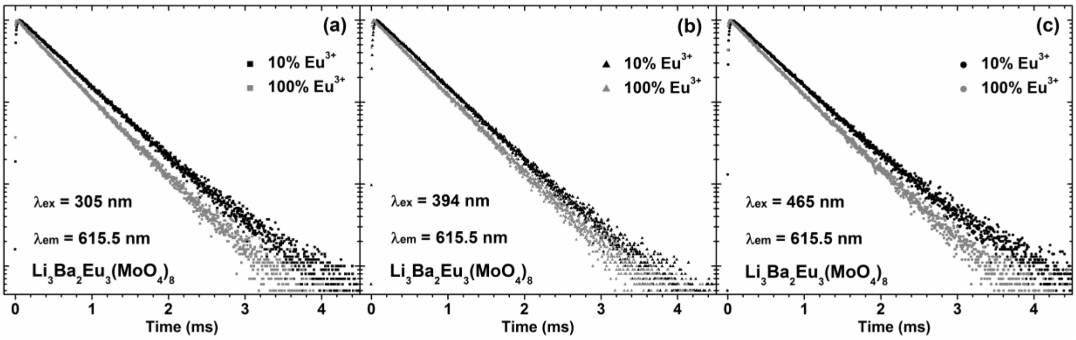

Figure 7.10 *Decay curves (λ_{em} = 615.5 nm) of 10% and 100% of Eu^{3+} doped samples at different excitation wavelengths: (a) 305 nm, (b) 394 nm and (c) 465 nm.*

$Li_3Ba_2La_3(MoO_4)_8$:Eu^{3+} phosphors were investigated as both Eu^{3+} concentration and temperature. The obtained results are summarized in *Table 7.2*. With raising the Eu^{3+} concentration the *x* and *y* coordinates increase and decrease, respectively. This indicates that colour points slightly shift towards deeper red spectral region in the CIE 1931 colour diagram, which fragment is shown in *Figure 7.11* for better visualization. It is also worth mentioning that sample doped with 100% of Eu^{3+} possesses colour point which is very close to the NTSC (National Television System Committee) standard for red chromaticity (0.670, 0.330) [178, 188, 189]. LE values slightly decreased with increasing Eu^{3+} concentration, what goes hand in hand with the shift of colour points to the deeper red region. However, the calculated LE values for $Li_3Ba_2La_3(MoO_4)_8:Eu^{3+}$ phosphors are still very high if compared to other red-emitting phosphors, viz. $Sr_2Si_5N_8:Eu^{2+}$ (λ_{em} = 620 nm, LE = 240 lm/W_{opt}), $CaAlSiN_3:Eu^{2+}$ (λ_{em} = 650 nm, LE = 150 lm/W_{opt}) and $CaS:Eu^{2+}$ (λ_{em} = 650 nm, LE = 85 lm/W_{opt}) [32]. It also evident that colour points are very stable in the temperature range of 100–500 K and this is a huge advantage of the phosphor considered for the application in pcLEDs.

Table 7.2 *Colour points and LE as a function of Eu^{3+} concentration in $Li_3Ba_2La_3(MoO_4)_8:Eu^{3+}$ at RT and as a function of temperature in $Li_3Ba_2Eu_3(MoO_4)_8$.*

$Li_3Ba_2La_3(MoO_4)_8:Eu^{3+}$				$Li_3Ba_2Eu_3(MoO_4)_8$			
Eu^{3+} (%)	**x**	**y**	**LE (lm/W_{opt})**	**T (K)**	**x**	**y**	**LE (lm/W_{opt})**
10	0.660	0.340	330	100	0.669	0.331	321
20	0.664	0.336	325	150	0.669	0.331	318
30	0.666	0.334	322	200	0.669	0.331	316
40	0.667	0.333	320	250	0.669	0.331	314
50	0.668	0.332	318	300	0.668	0.331	312
60	0.668	0.332	316	350	0.668	0.332	312
70	0.668	0.331	315	400	0.667	0.333	313
80	0.669	0.331	314	450	0.665	0.335	316
90	0.669	0.331	313	500	0.662	0.338	319
100	0.669	0.331	312				

Quantum efficiencies were calculated employing Eq. 5.1. The $LiEu(MoO_4)_2$ was used as a standard (QE = 100%, λ_{ex} = 465 nm) [71]. The results are represented in *Figure 7.12*. The QE values increase with increasing Eu^{3+} content in the host lattice and reach maximum (≈ 100%) when Eu^{3+} concentration is in the range 70–90%. The complete substitution of La^{3+} by Eu^{3+} leads to the slight decrease of QE value. The present finding shows that basically there is no concentration quenching in the synthesized phosphors. This leads to the conclusion that the large $(MoO_4)^{2-}$ groups separate the Eu^{3+}

ions to such an extent, that the probability of energy transfer between Eu^{3+} pairs, which causes concentration quenching, is rather low [178].

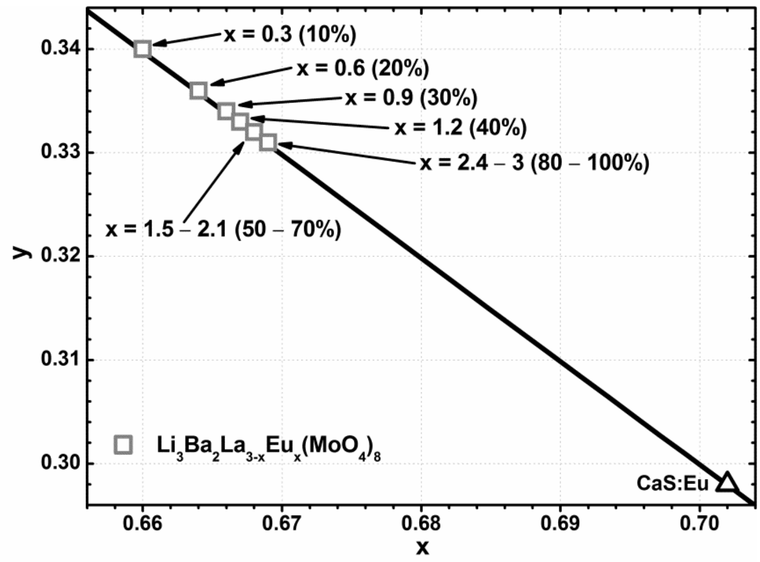

Figure 7.11 *Fragment of the CIE 1931 colour diagram with colour points of* $Li_3Ba_2La_{3-x}Eu_x(MoO_4)_8$ *phosphors as a function of* Eu^{3+} *concentration.*

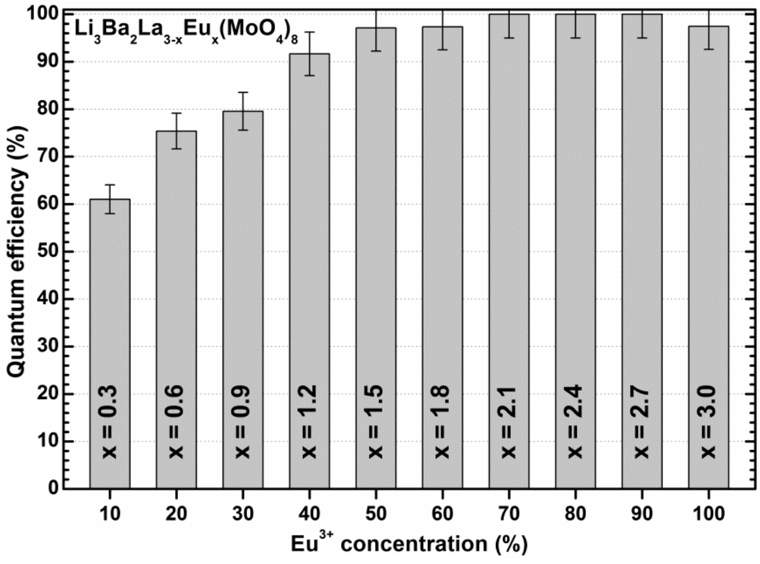

Figure 7.12 *Quantum efficiencies* (λ_{ex} *= 465 nm) of* $Li_3Ba_2La_3(MoO_4)_8$:Eu^{3+} *samples as a function of* Eu^{3+} *concentration.*

7.3. Optical Properties of $Li_3Ba_2Eu_3(MoO_4)_8$ *Ceramics*

Lanthanides usually suffer from a rather low absorption, because of the parity- and spin-forbidden character of their intraconfigurational $[Xe]4f^n \rightarrow [Xe]4f^n$ transitions [32, 119, 137]. This is a bottleneck for practical application, where strong absorption is one of the top requirements. Few actions can be taken to deal with the problem: first – adding a sensitizer to the material (sensitizer efficiently absorbs radiation and transfers the energy to activator), second – increasing the activator concentration (the drawback usually is concentration quenching), third – making ceramics (the absorption is increased due to longer optical pathway of the incident photons). The third option has been chosen in our case, because no sensitizer was available and the concentration of Eu^{3+} was already 100%. The $Li_3Ba_2Eu_3(MoO_4)_8$ ceramic disks with a thickness of 0.41 or 0.70 mm were prepared by applying 10 ton pressure (ø 1 cm disk) on the phosphor powder for 5 min. The obtained pellets were sintered at 800 °C for 5 h in air.

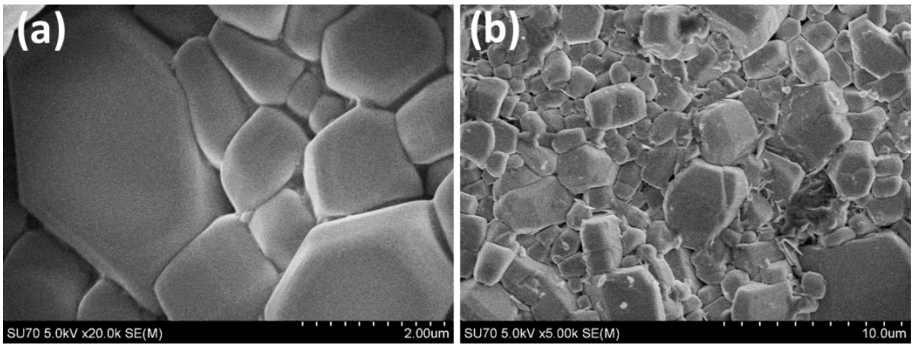

Figure 7.13 *SEM pictures of $Li_3Ba_2Eu_3(MoO_4)_8$ ceramics under magnification of (a) ×20.0k and (b) ×5.0k.*

The SEM images of the surface of prepared ceramic disks are shown in *Figure 7.13*. The surface comprises large and small particles grown together. However, for better quality ceramics a higher pressure and/or sintering temperature might be required. On the other hand, the increase of the sintering temperature is quite limited due to low melting point of material and ceramic disks annealed at 900 °C were already molten.

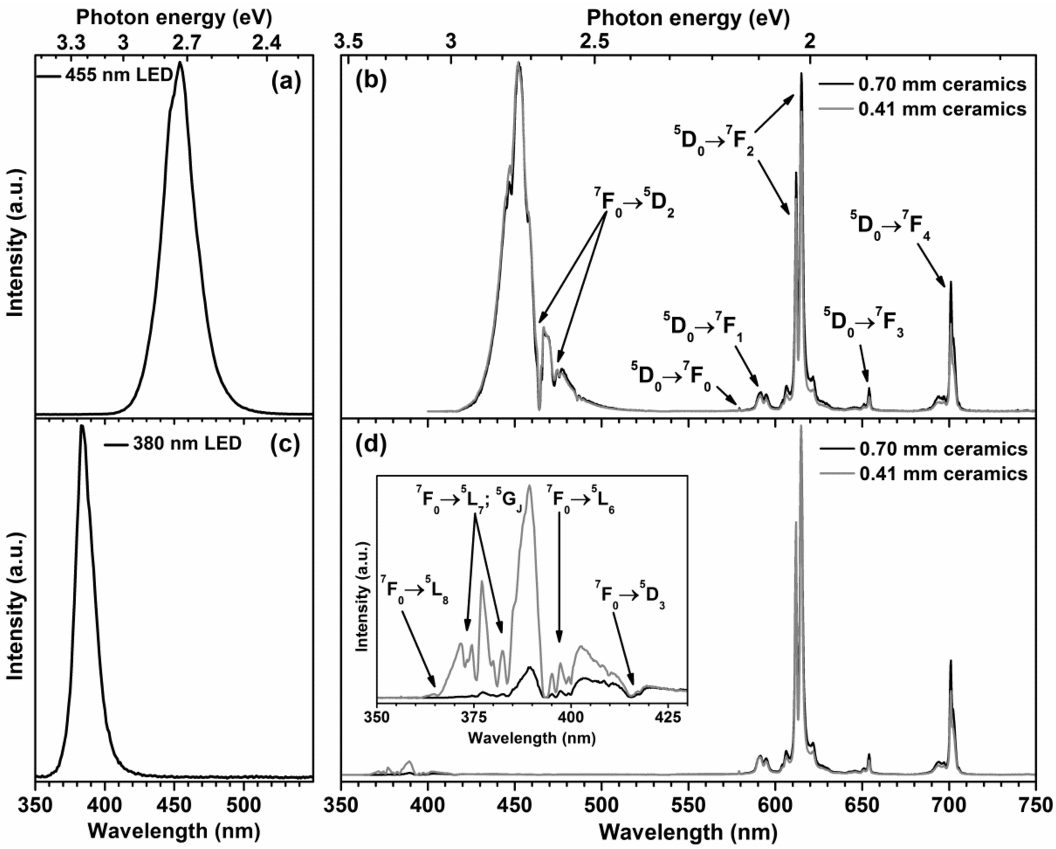

Figure 7.14 *(a) Emission spectrum of blue LED. (b) Emission spectra of* $Li_3Ba_2Eu_3(MoO_4)_8$ *ceramics excited by blue LED. (c) Emission spectrum of near-UV LED. (d) Emission spectra of* $Li_3Ba_2Eu_3(MoO_4)_8$ *ceramics excited by near-UV LED. Inset shows enlarged fragment in near-UV LED emission range.*

The emission spectra were recorded in the transmission mode, *i.e.* LED on the bottom and ceramic disk on top of it, in the range of 400–750 nm and 350–750 nm for blue ($\lambda_{max} \approx 455$ nm) and near-UV ($\lambda_{max} \approx 380$ nm) LED, respectively. The obtained spectra are given in *Figure 7.14*. The emission spectra of blue and near-UV LED are also plotted for comparison. It is obvious that a large portion of blue LED light is not absorbed by the ceramics (see *Figure 7.14b*), because only $^7F_0 \rightarrow {}^5D_2$ absorption occurs in this spectral region. The increase of ceramics thickness only slightly increased the Eu^{3+} emission intensity if compared to blue LED. However, the absorption of the light emitted by near-UV LED is more efficient as can be seen in *Figure 7.14d*. This is due to abundant absorption transitions, namely $^7F_0 \rightarrow {}^5D_{4,3}$, $^7F_0 \rightarrow {}^5L_J$ and $^7F_0 \rightarrow {}^5G_J$, of Eu^{3+} in this spectral region [183]. The 0.41 mm ceramics still passes some light emitted by near-UV LED, whereas 0.70 mm ceramics absorbs all of it as can be seen from the inset of *Figure 7.14d*. This leads to the conclusion that $Li_3Ba_2Eu_3(MoO_4)_8$ ceramics can be used for red emitting LEDs or as a red component in white emitting LEDs pumped by a near-UV emitting semiconductor die.

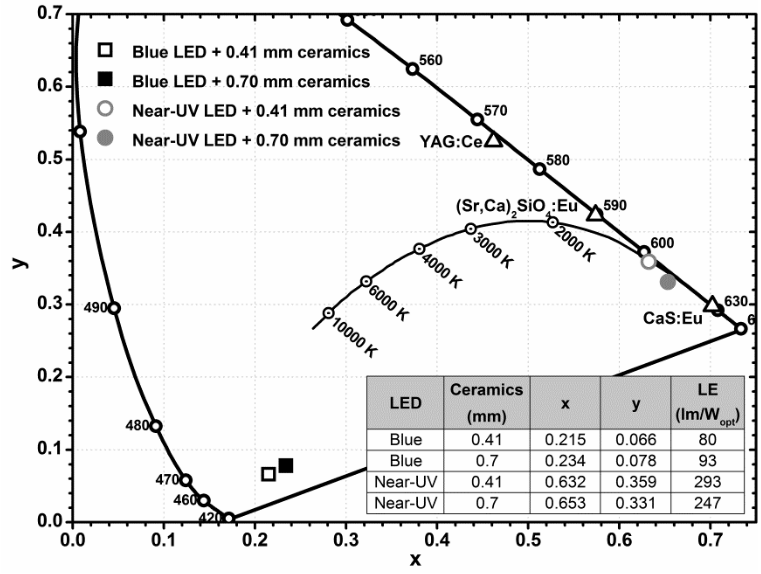

LED	Ceramics (mm)	x	y	LE (lm/W_{opt})
Blue	0.41	0.215	0.066	80
Blue	0.7	0.234	0.078	93
Near-UV	0.41	0.632	0.359	293
Near-UV	0.7	0.653	0.331	247

Figure 7.15 *Fragment of the CIE 1931 colour diagram with colour points of $Li_3Ba_2Eu_3(MoO_4)_8$ ceramics combined with the blue or near-UV LED. Exact colour points and LE values for each combination are given in the inset table.*

Figure 7.15 reveals that combination of the blue LED and $Li_3Ba_2Eu_3(MoO_4)_8$ ceramics gives the colour points lying in the purple region of the CIE 1931 colour diagram. As expected from *Figure 7.14b* the colour point of the thicker ceramics has shifted to the right in the diagram, because of the slightly stronger Eu^{3+} emission with respect to blue LED. The LE values of the spectra are rather small due to relatively low human eye sensitivity in the given regions. However, the combination of prepared ceramics with near-UV LEDs gives different results. Firstly, the colour points are in the reddish-orange region. Secondly, LE values are much higher. This is because of the brighter emission of Eu^{3+} if excited in the near-UV spectral region. The LE value considerably decreases with the increased thickness of the ceramics. The observed phenomenon can be explained by stronger emission intensity of $^5D_0 \rightarrow {}^7F_4$ transition with respect to $^5D_0 \rightarrow {}^7F_2$ (see *Figure 7.14d*). The emission of $^5D_0 \rightarrow {}^7F_4$ transition occurs at around 700 nm, where the human eye sensitivity is very low, thus reducing the LE value of the whole spectrum.

Chapter 8. $(Y,Lu)_3Al_3MgSiO_{12}:Ce^{3+}$ Green to Orange Emitting Phosphors

8.1. TG/DTA, XRD, and SEM Data Analysis

The TG/DTA curves of dried Y-Al-Mg-Si-O and Lu-Al-Mg-Si-O gels obtained after the glycolate sol-gel process are shown in *Figure 8.1* and *Figure 8.2*, respectively. The TG curve of the Y-Al-Mg-Si-O gel indicates the presence of a sudden mass loss step of about 25% at 194 °C accompanied by strong exothermal peak of the DTA curve. This process is likely caused by decomposition of yttrium and/or aluminium nitrates, whose decomposition temperatures were reported to be in the similar temperature range [190, 191]. The second mass loss step of about 39% occurs between 200 and 500 °C and can be attributed to further decomposition of metal nitrates and burning of organic residues that remained after the sol-gel process. Furthermore, there is a strong endothermic peak at 924 °C in the DTA curve. It can be attributed to the formation of the garnet phase.

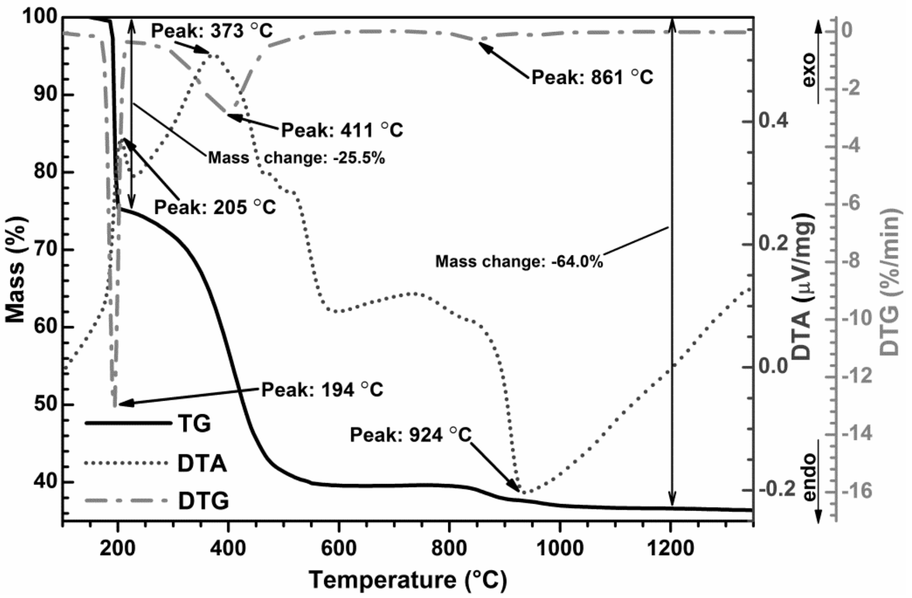

Figure 8.1 *TG/DTA curves of dried Y-Al-Mg-Si-O precursor gel.*

The TG/DTA curves of Lu-Al-Mg-Si-O gel (see *Figure 8.2*) are slightly different than those of Y derivative. There is one major mass loss step of about 43% in the range of 200−650 °C. It can be attributed to the decomposition of metal nitrates and organic residues. This is in good agreement with the strong exothermic peak at 367 °C in this temperature range. Like in a DTA curve of Y derivative there is a strong endothermic peak at 925 °C showing the formation of garnet phase.

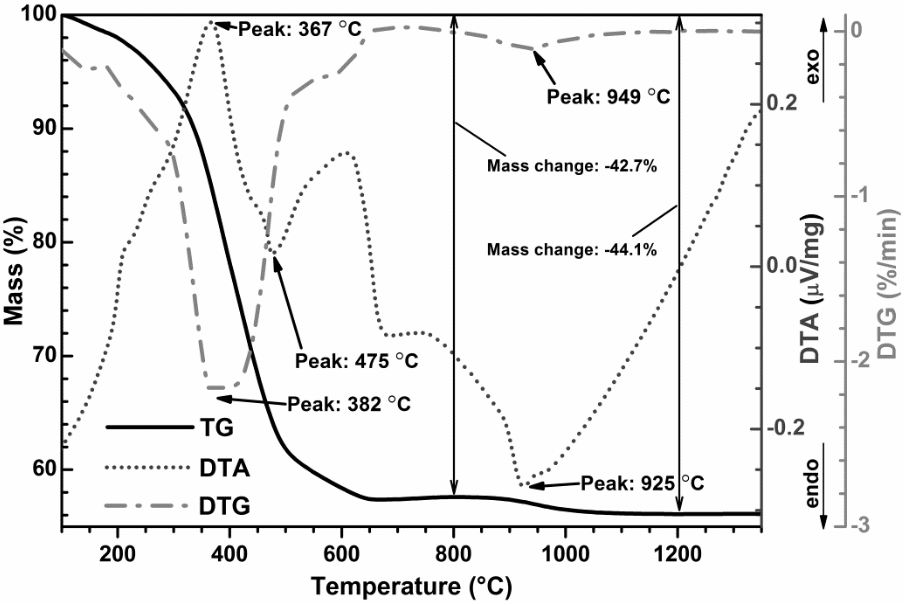

Figure 8.2 *TG/DTA curves of dried Lu-Al-Mg-Si-O precursor gel.*

XRD patterns of the synthesized undoped samples as a function of sintering temperature and Y/Lu ratio in the structure are shown in *Figure 8.3*. It turned out that at 500 °C no crystallization takes place and only amorphous material is obtained. However, sintering this amorphous material at 1200 °C or higher temperatures resulted in formation of garnet type compounds. XRD analysis revealed that besides the main garnet phase, the YAM phase ($Y_4Al_2O_9$ PDF4+ (ICDD) 04-013-3127, marked with asterisk) is present as an impurity, if powders were annealed at 1200 and 1400 °C. The amount of YAM phase decreased with increasing sintering temperature and finally single phase garnet materials were obtained once the temperature reached 1600 °C. As expected the width of XRD peaks decreased with increasing sintering temperature indicating particle growth. All aforementioned observations also apply to the samples with different Y/Lu ratio. The XRD patterns of $(Y,Lu)_3Al_3MgSiO_{12}$ powders sintered at 1600 °C matches well with the reference data. Moreover, the single phase garnet has been formed in the whole substitutional range of lutetium. This shows that the system $Y_3Al_3MgSiO_{12}$–$Lu_3Al_3MgSiO_{12}$ is a solid solution without a miscibility gap [192].

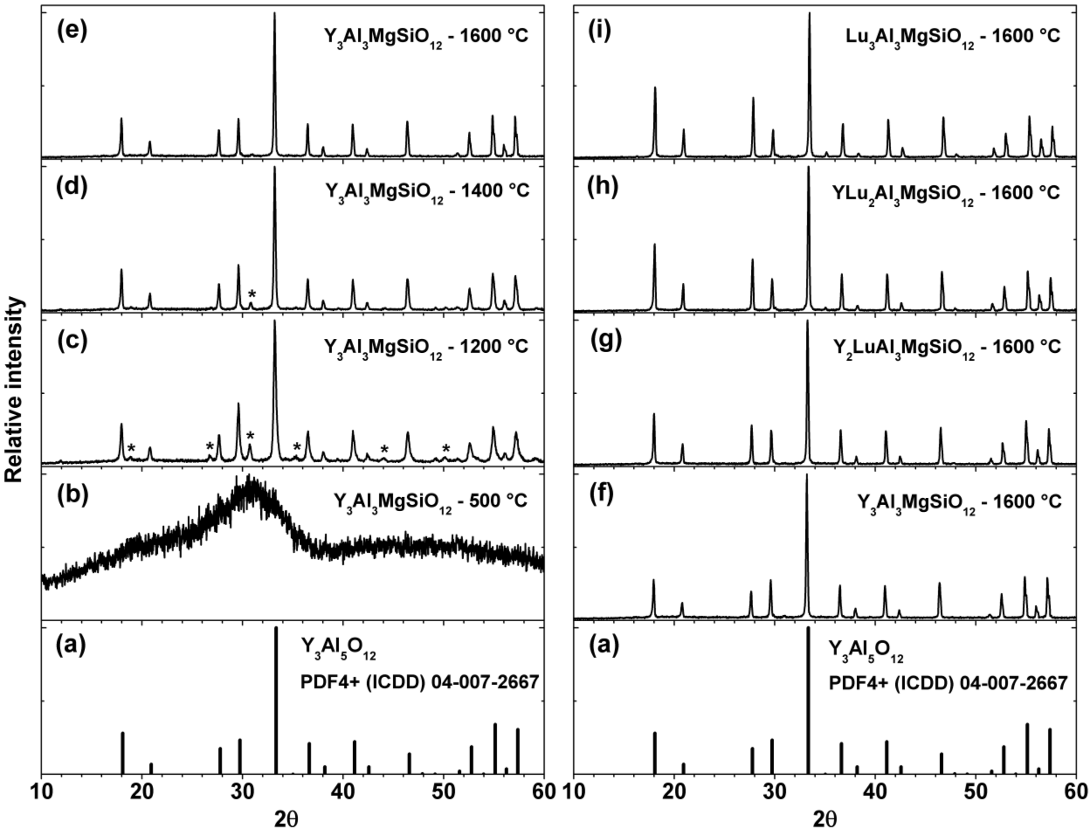

Figure 8.3 *XRD patterns of: (a) $Y_3Al_5O_{12}$ reference; (b–e) $Y_3Al_3MgSiO_{12}$ as a function of sintering temperature; (f–i) $(Y,Lu)_3Al_3MgSiO_{12}$ as a function of Y/Lu ratio.*

The morphological features of $Y_3Al_3MgSiO_{12}$ powders sintered at different temperatures were investigated by taking SEM pictures. The typical morphological images are shown in *Figure 8.4*. The sample sintered at 1200 °C possesses a sponge-like morphology. The particles are of irregular shape and are formed from highly agglomerated primary crystallites. The average crystallite size is in the sub-micrometre range and tends to increase with elevated sintering temperatures. The mean crystallite size of $Y_3Al_3MgSiO_{12}$ samples sintered at 1200, 1400, and 1600 °C is 60 nm, 800 nm, and 4.3 μm, respectively. Similar results were obtained for those samples containing lutetium [192].

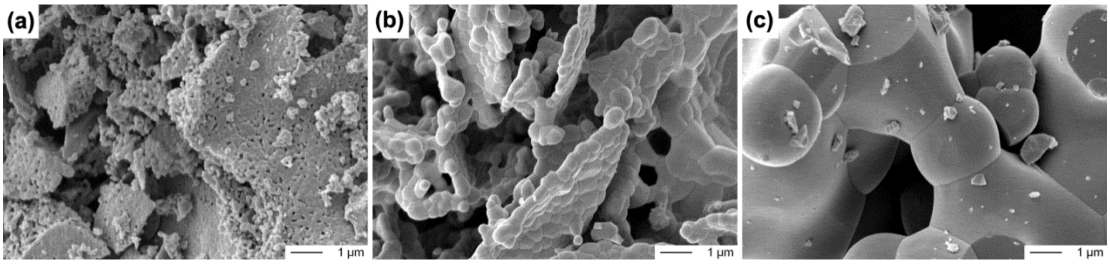

Figure 8.4 *SEM images of $Y_3Al_3MgSiO_{12}$ powders sintered at different temperatures: (a) 1200, (b) 1400 and (c) 1600 °C.*

8.2. Optical Properties

The body colour of all undoped samples regardless the Y/Lu ratio was white indicating that there is no absorption in the visible spectral region. However, the body colour of Ce^{3+} doped samples varied from green to orange depending on Y/Lu ratio. This indicates the strong absorption in the blue spectral region and is in good agreement with reflection spectra given in *Figure 8.5*. The colour of the samples also became more intensive with increased Ce^{3+} concentration leading to the stronger absorption (see *Figure 8.5a*).

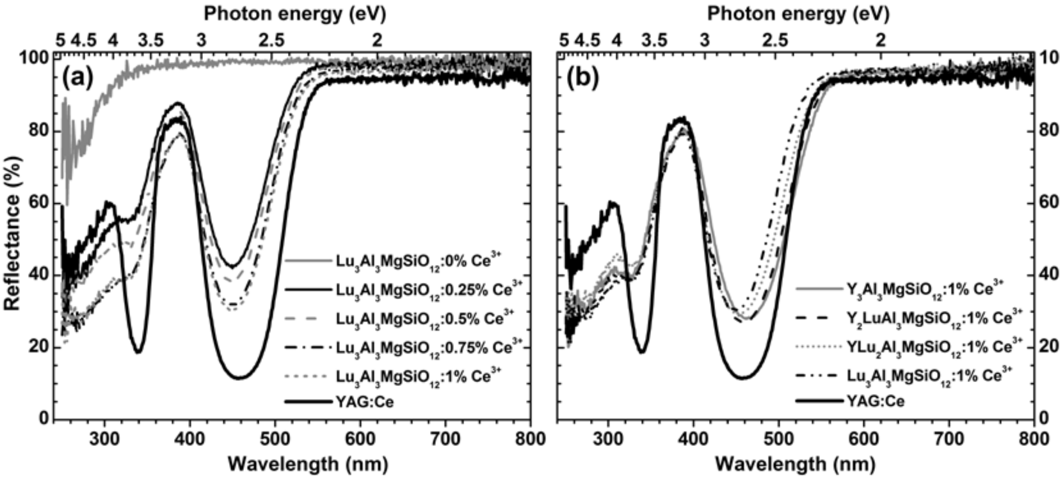

Figure 8.5 *(a) Reflection spectra of $Lu_3Al_3MgSiO_{12}:Ce^{3+}$ as a function of Ce^{3+} concentration; (b) reflection spectra of $(Y,Lu)_3Al_3MgSiO_{12}:1\%Ce^{3+}$ as a function of Y/Lu ratio.*

The reflection spectra shown in *Figure 8.5b* indicates that substitution of Y by Lu in the structure causes a slight shift of Ce^{3+} absorption band towards shorter wavelengths. This is likely caused by the decreased crystal field strength of the host lattice once Y is replaced by Lu. Similar results are observed for YAG:Ce and LuAG:Ce, where the strongest Ce^{3+} absorption band is located at 460 and 450 nm, respectively [38]. Reflection spectra reveal that prepared phosphor powders possess high brilliance since the reflectance values at longer wavelengths are close to unity.

The excitation spectra of samples with different Y/Lu ratio are depicted in *Figure 8.6a*. The spectra of YAG:Ce is also included for reference. The excitation spectra contain two broad bands attributed to the [Xe]4f^1 → [Xe]5d^1 transition of Ce^{3+} ions. The higher energy band is much weaker than its lower energy counterpart. This is probably caused by photoionization, *i.e.* the higher crystal-field component of the excited [Xe]5d^1 configuration of Ce^{3+} is likely close or in the conduction band. It was also observed that the splitting between the high and low energy bands decreases with higher Lu content in the structure. This indicates that the crystal-field strength decreases with the increasing Lu content in the host lattice.

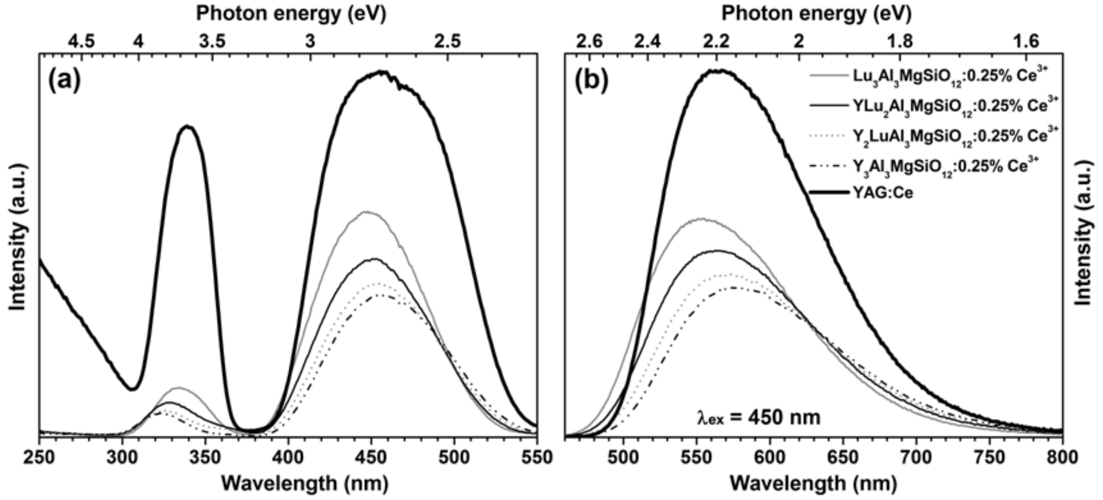

Figure 8.6 *Excitation (a) and emission (b) spectra of* $(Y,Lu)_3Al_3MgSiO_{12}:0.25\%Ce^{3+}$ *samples as a function Y/Lu ratio.*

The emission spectra of the same samples are shown in *Figure 8.6b*. The spectra comprise a broad band, which is due to two strongly overlapping bands from the lowest crystal-field component of the [Xe]5d^1 configuration to the spin-orbit split sublevels $^2F_{5/2}$ and $^2F_{7/2}$ of the [Xe]4f^1 configuration of Ce^{3+} ions [193]. The emission maximum shifted from 555 to 575 nm when all lutetium was substituted by yttrium. This indicates that the stronger crystal-field strength is generated if Y content in the host lattice increases. This goes hand in hand with the data obtained from excitation spectra. Moreover, the highest emission intensity was obtained for the samples doped with 0.25% and 0.5% of Ce^{3+} [44]. Emission maximum also can be shifted towards longer wavelengths by ≈ 10 nm when Ce^{3+} concentration is increased from 0.25% to 1%. This is likely caused by re-absorption when the intensity of lower energy band increases with the cost of higher energy one. On the other hand, the increased Ce^{3+} concentration leads to drop of emission intensity due to concentration quenching. The red-shifted emission might be caused by increased Stokes shift, covalent character, and crystal-field splitting or a combination of all these parameters. For determination of the Stokes shift and a splitting between the two E_g levels, samples doped with 0.033% of Ce^{3+} were prepared in order to avoid energy transfer and re-absorption of emission as suggested by Bachmann et al. [2, 194]. The excitation and emission spectra of these samples were recorded at 100 K. The Stokes shift was calculated as the energy difference between the lowest energy band of excitation spectra and the higher energy band of emission spectra. Before the calculations were performed, wavelength was converted to wavenumbers and intensity of emission spectra was corrected by the function [137]:

$$I_E = \frac{I_\lambda \times \lambda^2}{hc} \qquad (Eq. 8.1)$$

wherein I_E and I_λ are intensities per energy and wavelength interval, respectively. λ is the wavelength, h and c are the Planck constant and the velocity of light, respectively. The calculated Stokes shift values for $Y_3Al_3MgSiO_{12}$, $Y_2LuAl_3MgSiO_{12}$, $YLu_2Al_3MgSiO_{12}$, and $Lu_3Al_3MgSiO_{12}$ are 3150, 3170, 3120, and 3050 cm^{-1}, respectively. The Stokes shift for YAG:Ce is about 2400 cm^{-1} [2, 194]. Obviously the obtained Stokes shift values are quite similar with respect to Y/Lu ratio in the structure. This implies that the observed red-shift of emission is not caused by Stokes shift. The energy difference between two excitation bands for $Y_3Al_3MgSiO_{12}$, $Y_2LuAl_3MgSiO_{12}$, $YLu_2Al_3MgSiO_{12}$, and $Lu_3Al_3MgSiO_{12}$ is 9580, 8940, 8250, and 7610 cm^{-1}, respectively [44]. However, the energy difference between the same levels in

YAG:Ce is about 7500 cm^{-1} [2, 194] confirming stronger crystal-field strength in the garnet hosts upon Mg^{2+}–Si^{4+} incorporation. This is in good agreement with some other Ce^{3+} doped silicate garnets reported by Setlur et al. [155] and Kishore et al. [151].

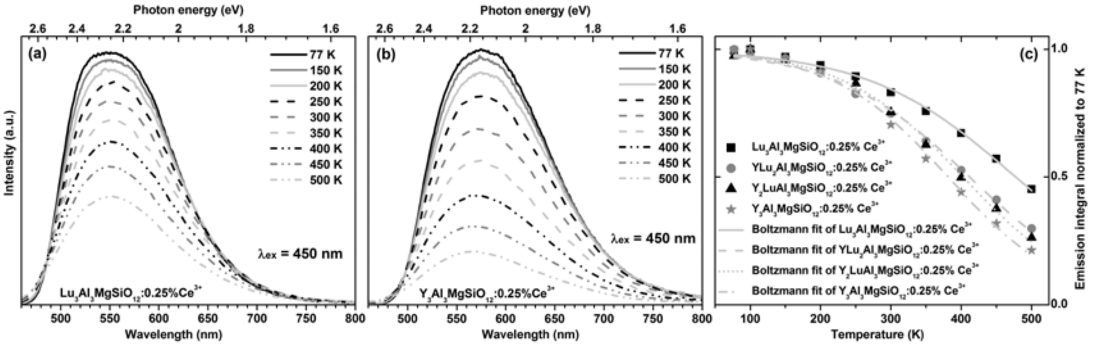

Figure 8.7 *Temperature dependent emission spectra of* $Lu_3Al_3MgSiO_{12}$*:0.25%*Ce^{3+} *(a) and* $Y_3Al_3MgSiO_{12}$*:0.25%*Ce^{3+}*; (c) thermal quenching of 0.25%* Ce^{3+} *doped samples as a function of Y/Lu ratio.*

Thermal quenching behaviour of synthetized samples was investigated with respect to Y/Lu ratio in the structure. The obtained results are summarized in *Figure 8.7*. Temperature dependent emission spectra of $Lu_3Al_3MgSiO_{12}$:0.25%Ce^{3+} and $Y_3Al_3MgSiO_{12}$:0.25%Ce^{3+} are shown in *Figure 8.7a* and *Figure 8.7b*, respectively. The PL intensity gradually decreases with the increasing temperature for both samples. However, the red-shifted emission of $Y_3Al_3MgSiO_{12}$:0.25%Ce^{3+} sample shows stronger thermal quenching than its Lu derivative. This is in line with the results obtained by Chiang et al. [45]. Chiang and co-workers investigated TQ behaviour of $Y_3Al_5O_{12}$:Ce^{3+}, $Tb_3Al_5O_{12}$:Ce^{3+}, and $Gd_3Al_5O_{12}$:Ce^{3+} and showed, that the strongest TQ is observed for the $Gd_3Al_5O_{12}$:Ce^{3+} sample, possessing the most red-shifted emission among the investigated phosphors. It was also observed that emission maximum shifted towards shorter wavelengths upon temperature increase. This is explained the stronger thermal quenching of lower energy emission band of Ce^{3+} if compared to higher energy one. A Boltzmann sigmoidal fit was employed for calculation of $TQ_{1/2}$ values from the normalized emission integrals of 0.25% Ce^{3+} doped samples with different Y/Lu ratio. The experimental data and fitted curves are depicted in *Figure 8.7c*.

The obtained $TQ_{1/2}$ values for $Y_3Al_3MgSiO_{12}$:0.25%Ce^{3+}, $Y_2LuAl_3MgSiO_{12}$:0.25%Ce^{3+}, $YLu_2Al_3MgSiO_{12}$:0.25%Ce^{3+}, and $Lu_3Al_3MgSiO_{12}$:0.25%Ce^{3+} samples are 382, 403, 412, and 478 K, respectively. The $TQ_{1/2}$ of YAG:Ce is about 530 K. Obviously, TQ becomes more severe if the emission band is red-shifted. The explanation for this is that incorporated Mg^{2+} and Si^{4+} ions decrease the band gap of the garnet type host lattice, since the Stokes shift of all prepared samples is about 3100 cm^{-1} and thus not dependent on the Y/Lu ratio. A reduced band gap compared to YAG:Ce or LuAG:Ce will promote photoionization at lower temperature and thus yield a lower temperature of thermal quenching. This interpretation is in line with the observation that the second excitation band at 325 nm is much weaker than that of unmodified YAG:Ce. This TQ mechanism, however, is different from that observed in aluminium garnets, wherein stronger TQ is explained by increased Stokes shift, which is in line with a configurational coordinate model for quenching [2, 45, 194].

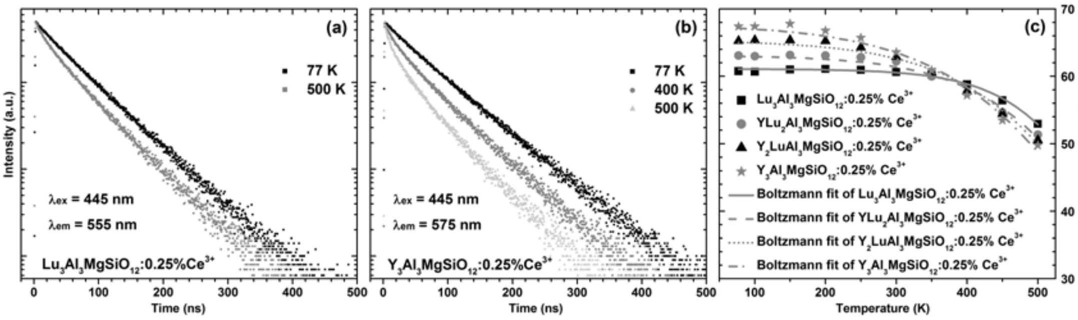

Figure 8.8 *Temperature dependent decay curves of* $Lu_3Al_3MgSiO_{12}$*:0.25%*Ce^{3+} *(a) and* $Y_3Al_3MgSiO_{12}$*:0.25%*Ce^{3+}*; (c) thermal quenching of 0.25%* Ce^{3+} *doped samples as a function of Y/Lu ratio.*

Thermal quenching behaviour of decay times of synthetized samples was also investigated with respect to Y/Lu ratio in the structure. Temperature dependent decay curves of $Lu_3Al_3MgSiO_{12}$:0.25%Ce^{3+} and $Y_3Al_3MgSiO_{12}$:0.25%Ce^{3+} are shown in *Figure 8.8a* and *Figure 8.8b*, respectively. The decay times of Lu derivative are slightly shorter than its Y counterpart. This is due to green shifted emission of Lu compound if compared to Y one. As expected, the decay curves became steeper with increasing temperature indicating the decrease of decay times. The shorter decay times are attributed to the decrease of the internal efficiency of activator ions [194]. The decay times decrease much faster for $Y_3Al_3MgSiO_{12}$:0.25%Ce^{3+}. This observation is in line with temperature dependent emission spectra (see *Figure 8.7*), where the emission intensity of Y derivative decreased much faster than its Lu counterpart. This once again confirms that temperature quenching becomes more severe for the red-shifted Ce^{3+} doped garnet phosphors. Moreover, at low temperatures the emission decays mono-exponentially, whereas at high temperatures the bi-exponential decay was observed. The weight of the second (faster) component increased with increasing temperature and is attributed to the quenching processes. *Figure 8.8c* shows calculated decay times of $(Y,Lu)_3Al_3MgSiO_{12}$:0.25%Ce^{3+} phosphors as a function of Y/Lu ratio and the temperature. The Boltzmann fit was used to calculate $TQ_{1/2}$ values from the obtained data. However, since the decay times do not decrease more than half of the initial values, the fit resulted in $TQ_{1/2}$ values with greater error (±14 K) than those obtained from emission integrals (±4 K). The calculated $TQ_{1/2}$ values from decay times for $Y_3Al_3MgSiO_{12}$:0.25%Ce^{3+}, $Y_2LuAl_3MgSiO_{12}$:0.25%Ce^{3+}, $YLu_2Al_3MgSiO_{12}$:0.25%Ce^{3+}, and $Lu_3Al_3MgSiO_{12}$:0.25%Ce^{3+} samples are 607, 620, 631, and 631 K, respectively. These values are about 200 K higher than the ones obtained from temperature dependent emission integrals shown in *Figure 8.7c*. This indicates that internal efficiency (proportional to decay times) of Ce^{3+} decreases much slower than its external efficiency (proportional to internal efficiency and escape efficiency). Hence, the thermal quenching is caused either by decreased escape efficiency or by an increases probability for re-absorption.

Figure 8.9a shows the colour points of the $(Y,Lu)_3Al_3MgSiO_{12}:Ce^{3+}$ phosphors as a function of Y/Lu ratio and Ce^{3+} concentration at RT. The colour points of LuAG:Ce, YAG:Ce, and LEDs emitting at 448 and 465 nm are also added for reference. The colour points of prepared phosphors are distributed close to the edge of CIE 1931 colour diagram showing high colour saturation. As anticipated from emission spectra, the colour points shifted from green-yellow to yellow-orange part of the CIE 1931 chromaticity diagram if the yttrium content in the lattice increased. Similar shift was also observed with increasing Ce^{3+} concentration. Lines in *Figure 8.9a* denote colour-mixing solutions of the conventional dichromatic phosphor converted solid-state lamp composed of a 465 nm emitting LED and the prepared phosphors. Obviously, the combination of 465 nm emitting LED and $Lu_3Al_3MgSiO_{12}$:0.25%Ce^{3+} would not result in a white light source, since the respective colour gamut does not overlap with BBL. However, combination of 465 nm emitting LED and $YLu_2Al_3MgSiO_{12}$:0.25%Ce^{3+}, $Y_2LuAl_3MgSiO_{12}$:0.25%Ce^{3+}, $Y_3Al_3MgSiO_{12}$:0.25%Ce^{3+}, or $Y_3Al_3MgSiO_{12}$:1%Ce^{3+} phosphors would enable blends, which have a colour point corresponding to white light for the CCT of around 7000, 5000, 4000, and 3000 K, respectively. *Figure 8.9a* also reveals that the employment of 448 nm emitting LED would enable even a warmer white light source, but this will go at the cost of luminous efficacy.

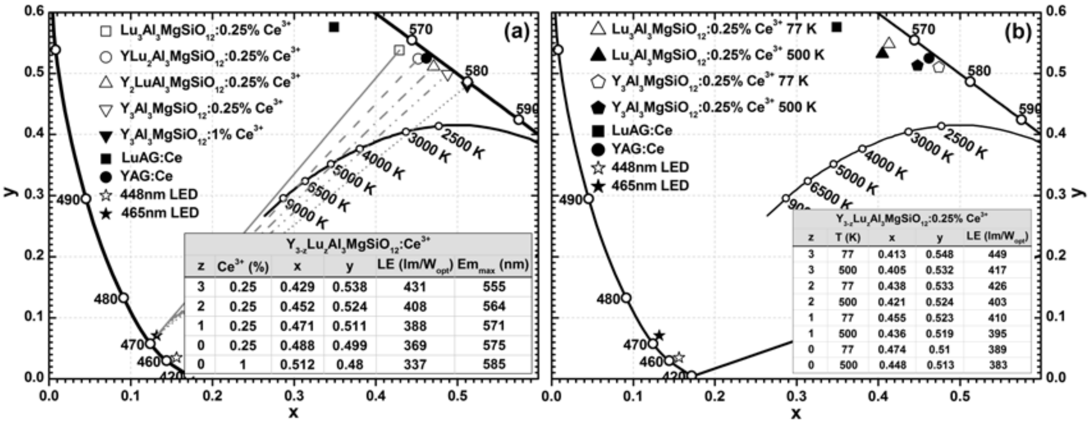

$Y_{3-z}Lu_zAl_3MgSiO_{12}:Ce^{3+}$

z	Ce^{3+} (%)	x	y	LE (lm/W_{opt})	Em_{max} (nm)
3	0.25	0.429	0.538	431	555
2	0.25	0.452	0.524	408	564
1	0.25	0.471	0.511	388	571
0	0.25	0.488	0.499	369	575
0	1	0.512	0.48	337	585

$Y_{3-z}Lu_zAl_3MgSiO_{12}$:0.25% Ce^{3+}

z	T (K)	x	y	LE (lm/W_{opt})
3	77	0.413	0.548	449
3	500	0.405	0.532	417
2	77	0.438	0.533	426
2	500	0.421	0.524	403
1	77	0.455	0.523	410
1	500	0.436	0.519	395
0	77	0.474	0.51	389
0	500	0.448	0.513	383

***Figure 8.9** Fragments of the CIE 1931 colour diagram with colour points of (a) (Y,Lu)$_3$Al$_3$MgSiO$_{12}$:Ce^{3+} as a function of Ce^{3+} concentration and Y/Lu ratio (exact colour points, luminous efficacies and emission maxima are given in inset table); (b) Y and Lu derivatives at different temperatures (exact colour points and luminous efficacies for each temperature are given in inset table).*

The relation between Y/Lu ratio and Ce^{3+} concentration to colour points, LE values, and emission maximum is summarized in the inserted table in *Figure 8.9a*. LE values decreases if Lu is substituted by Y and with higher Ce^{3+} concentration. The observed decrease is caused by the red-shift of emission spectra and, consequently, smaller overlap with the human eye sensitivity curve.

Figure 8.9b illustrates part of the CIE 1931 chromaticity diagram with the temperature dependent colour points of 0.25% Ce^{3+} doped samples with different Y/Lu ratio. The colour points move away from the edge upon temperature increase. Thus the colour saturation decreases with increasing temperature. This is attributed to the blue-shift of Ce^{3+} emission maximum and broadening of emission spectra with the increasing temperature. Considering the very broad temperature range, the colour points of the prepared samples are rather stable, what is one of the requirements for LED phosphors. Moreover, the colour point stability increases if the emission maximum is at shorter wavelengths. Therefore, this could be a bottleneck for practical application of so desired red-shifted garnets, like $Y_3Al_3MgSiO_{12}$:Ce^{3+}.

The inset table of *Figure 8.9b* summarizes the relation of Y/Lu ratio to temperature, colour points, and LE values. The LE values decrease with increasing Y content in the lattice and this is attributed to the lower overlap between human eye sensitivity curve and red-shifted emission spectra following the same trend. It was also observed that LE values decrease with at high temperatures and this contradicts to the blue-shift of emission maximum at elevated temperatures (see *Figure 8.7*). However, with increasing temperature the emission spectra become broader and, therefore, leads to lower overlap with human eye sensitivity curve regardless the blue-shift of maximum.

The quantum efficiencies of all synthesized samples were calculated according to Eq. 5.1. It was observed that QE values gradually increases upon increasing the sintering temperature and reaches maximum if samples are annealed at 1600 °C. The QE values as a function of Ce^{3+} concentration and Y/Lu ratio in the lattice are shown in *Figure 8.10*. Regardless the Y/Lu ratio the most efficient samples were those doped with 0.25% of Ce^{3+}. The increase of activator concentration resulted in gradual decrease of efficiency. Moreover, the complete substitution of Y by Lu in the structure has led to the increase of QE values from 68% to 86% if samples were doped with 0.25% of Ce^{3+}. These results go hand in hand with the emission spectra depicted in *Figure 8.6b*, where emission intensity decreased with increasing Y content in the lattice while maintaining the same Ce^{3+} concentration. This once again indicates that the red-shift of the emission band results in a decrease in efficiency.

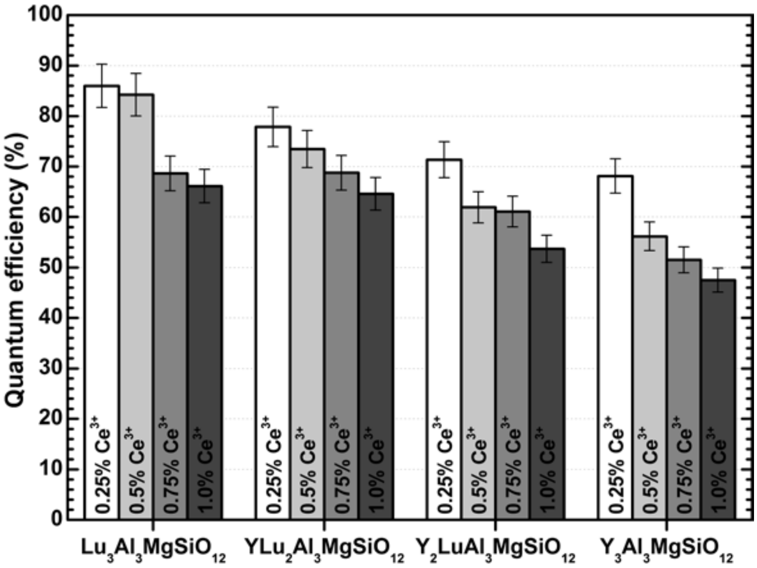

Figure 8.10 *Quantum efficiencies of the* $(Y,Lu)_3Al_3MgSiO_{12}:Ce^{3+}$ *samples sintered at 1600 °C.*

Chapter 9. $CaLu_2Al_4SiO_{12}$:Ce^{3+} Green Emitting Phosphors

9.1. TG/DTA, XRD, and SEM Data Analysis

The TG/DTA curves of Ca-Lu-Al-Si-O precursor gel obtained after the combustion process are shown in *Figure 9.1*. The TG curve reveals that the mass loss happens in two steps. The first step (peak at 550 °C) yielded in a mass loss of about 12% and can be attributed to burning of organic residues that remained after the combustion process. This is in line with the DTA curve (peak at 520 °C), which shows exothermic processes occurring in that temperature range. The second mass loss step of 5% takes place in the temperature range 800–1000 °C and can be attributed to the decomposition of metal carbonates or oxy-carbonates. This is in good agreement with the DTA curve showing endothermic processes in this temperature range. According to the DTA curve, the garnet phase starts to form around 996 °C, which was confirmed by powder XRD measurements as depicted in *Figure 9.2*.

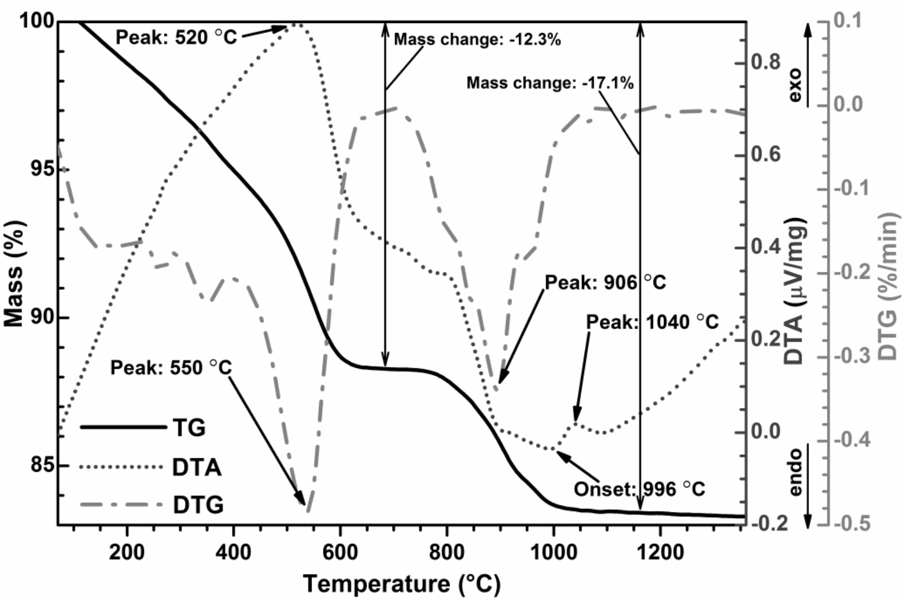

Figure 9.1 *TG/DTA curves of the Ca-Lu-Al-Si-O precursor gel obtained after the combustion process.*

XRD patterns of undoped $CaLu_2Al_4SiO_{12}$ powders as a function of sintering temperature are shown in *Figure 9.2* along with a reference pattern of $Lu_3Al_5O_{12}$. It is obvious that during the combustion process no crystallization takes place. However, the garnet phase with some minor secondary phases was already obtained after annealing powders at 1000 °C for 2 h in air. The peaks that do not belong to the garnet phase are marked with an asterisk. Unfortunately, the identification of the secondary phases formed after the calcination at 1000 °C was not successful. Subsequent sintering at 1400–1500 °C for 4 h resulted in single phase garnet type materials. Besides, no differences in the XRD patterns were observed if the synthesized garnets were doped with Ce^{3+} (at least up to 3 mol-%). The samples sintered at temperatures higher than 1500 °C were molten, suggesting that the melting point of the materials is close to this temperature.

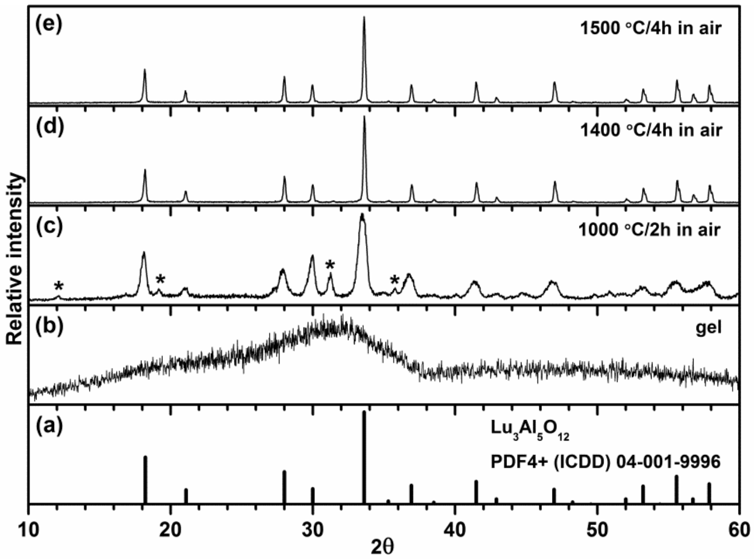

Figure 9.2 *XRD patterns of: (a)* $Lu_3Al_5O_{12}$ *reference; (b) Ca-Lu-Al-Si-O gel after combustion process; (c) sample annealed at 1000 °C for 2 h; and subsequently sintered for 4 h in air at (d) 1400 °C or (e) 1500 °C.*

The SEM images of $CaLu_2Al_4SiO_{12}$ samples sintered at 1000, 1400, and 1500 °C are shown in *Figure 9.3*. The sample sintered at 1000 °C possesses a sponge-like morphology with large voids, which, likely, were former by escaping gas during the firing process of initial gel. However, annealing powders at 1400 °C results in the formation of well-shaped particles with the size in the range of 0.5–3 μm and high degree of agglomeration. Further increase of the sintering temperature leads to even larger particles and stronger agglomeration.

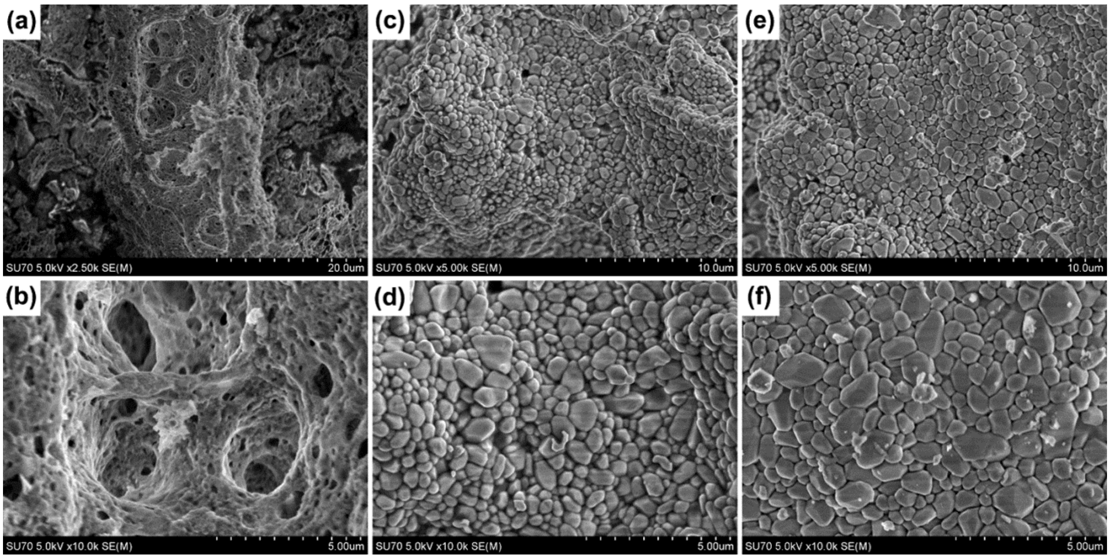

Figure 9.3 *SEM images of $CaLu_2Al_4SiO_{12}$ samples sintered at 1000 °C under magnification of (a) ×2.5k and (b) ×10.0k; 1400 °C (c) ×5.0k and (d) ×10.0k; 1500 °C (e) ×5.0k and (f) ×10.0k.*

9.2. Optical Properties

The body colour of undoped sample was bright white indicating that there is no absorption in the visible spectral region. However, Ce^{3+} doped samples possessed a slightly greenish to pale yellow body colour depending on dopant concentration caused by the strong absorption of the activator in the blue spectral region. This is in line with the reflection spectra depicted in *Figure 9.4*. As expected, absorption increased with increasing doping level of Ce^{3+}. It is also evident that the absorption band of phosphors under investigation is slightly shifted towards shorter wavelengths if compared to conventional LuAG:Ce phosphor, 440 vs. 450 nm, respectively. This indicates that the lowest 5d crystal-field component of Ce^{3+} in $CaLu_2Al_4SiO_{12}$ host lattice lies at a higher energy than in LuAG:Ce. Samples also possess high brilliance since the reflectance at longer wavelengths is rather close to unity. However, reflectance at longer wavelengths decreases with increasing Ce^{3+} concentration, probably due to defect formation in the lattice.

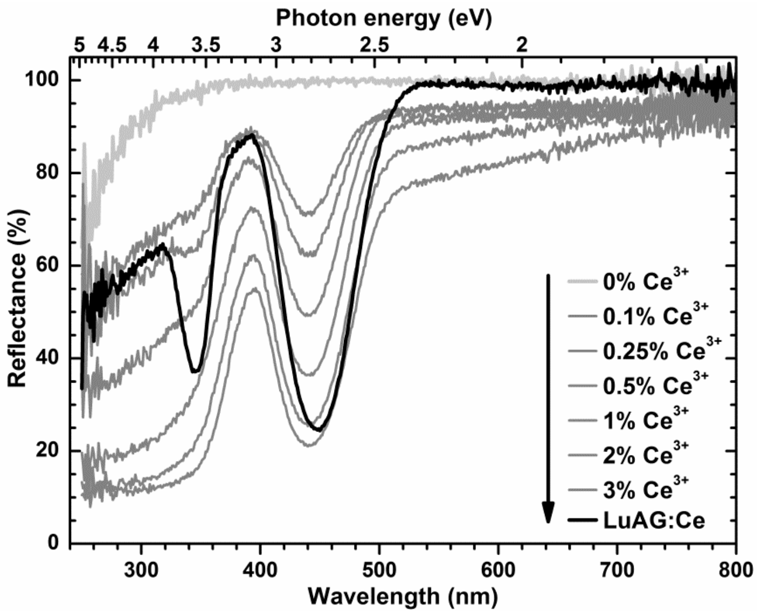

Figure 9.4 *Reflection spectra of $CaLu_2Al_4SiO_{12}:Ce^{3+}$ powders sintered at 1400 °C as a function of Ce^{3+} concentration.*

Figure 9.5a and *Figure 9.5b* display excitation and emission spectra of $CaLu_2Al_4SiO_{12}:Ce^{3+}$ phosphors as a function of Ce^{3+} concentration, respectively. LuAG:Ce is also included in the spectra for comparison. The excitation spectra contain two broad bands attributed to the $[Xe]4f^1 \rightarrow [Xe]5d^1$ transitions of Ce^{3+} ions. The higher energy band is much weaker than its counterpart at lower energy. This is quite different from the excitation spectrum of LuAG:Ce whose low and high energy bands are of comparable intensities. This phenomenon might be attributed to photoionization, i.e. the higher crystal-field component of the excited $[Xe]5d^1$ configuration of Ce^{3+} in the $CaLu_2Al_4SiO_{12}$ host lattice is likely close to or in the conduction band. This is in line with VUV reflection measurement of the undoped sample. It shows that the optical band gap of $CaLu_2Al_4SiO_{12}$ host lattice is at 215 nm (5.77 eV), whereas the optical band gap of LuAG is about 177 nm (7.01 eV) [163].

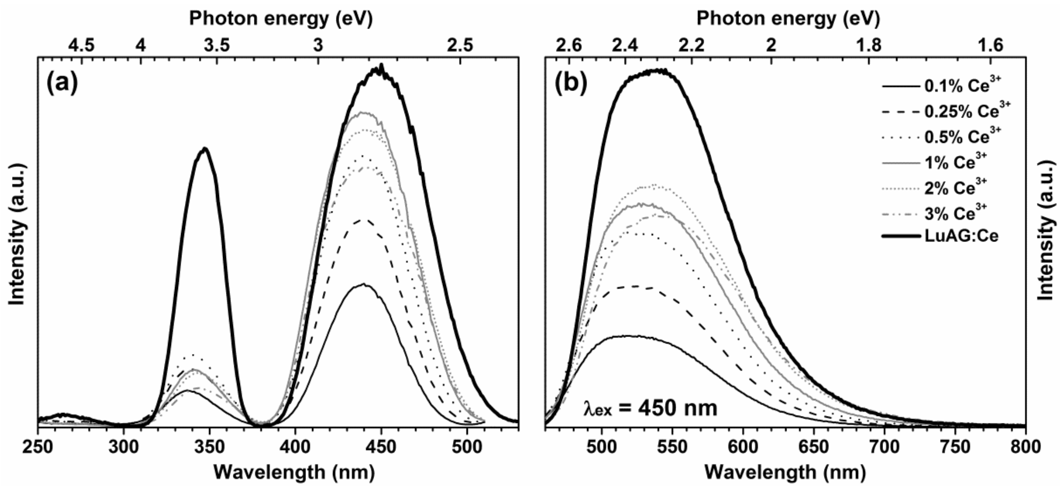

Figure 9.5 *Excitation (a) and emission (b) spectra of* $CaLu_2Al_4SiO_{12}:Ce^{3+}$ *powders sintered at 1400 °C as a function of* Ce^{3+} *concentration.*

The emission spectra of the synthesized phosphors are depicted in *Figure 9.5b* and comprise one broad band, which is a result of the strong overlap of the two bands originating in the transitions from the lowest crystal-field component of the $[Xe]5d^1$ configuration to the spin–orbit split sublevels $^2F_{5/2}$ and $^2F_{7/2}$ of the $[Xe]4f^1$ configuration of Ce^{3+} ions [44, 193]. It turns out that the emission properties are very sensitive to variations of the Ce^{3+} concentration. With increasing Ce^{3+} concentration from 0.1 to 3.0 mol-% the emission maximum shifts from 520 to 542 nm. This is probably caused by re-absorption process (an emitted photon is again absorbed by activator due to overlapping absorption and emission bands). However, at higher activator concentrations the emission intensity drops down indicating concentration quenching. The emission of the phosphors under investigation is shifted towards shorter wavelengths (higher energies) if compared to YAG:Ce [44] and LuAG:Ce [195] emitting at around 560 and 540 nm, respectively. The anticipated increase in the Ce–O bond distance upon substitution of trivalent Lu (0.977 Å) by divalent Ca (1.22 Å) [158, 196] results in a reduced crystal-field strength on Ce^{3+} ion. The reduced crystal-field strength leads to a larger gap between the lowest excited state and the ground state. To determine the Stokes shift and the splitting between the crystal-field components of the $[Xe]5d^1$ configuration of Ce^{3+} in the $CaLu_2Al_4SiO_{12}$ host lattice, emission and excitation spectra were recorded at 77 K for a sample containing 0.1% of Ce^{3+}.

The Stokes shift was calculated as the energy difference between the excitation band with the lowest energy and the high energy emission band. The intensity of the emission spectrum was corrected by applying Eq. 8.1. The calculated Stokes shift for $CaLu_2Al_4SiO_{12}$ is 2040 cm^{-1}. The Stokes shift of YAG:Ce [2, 194] and LuAG:Ce [197] was reported to be about 2400 and 2700 cm^{-1}, respectively. The energy difference between the crystal-field components of the $[Xe]5d^1$ configuration in $CaLu_2Al_4SiO_{12}$:0.1%Ce^{3+}, LuAG:Ce [198] and YAG:Ce [2, 194] was 6950, 7000 and 7500 cm^{-1}, respectively. This goes hand in hand with the explanation for the blue-shifted emission resulting from a lower crystal-field splitting.

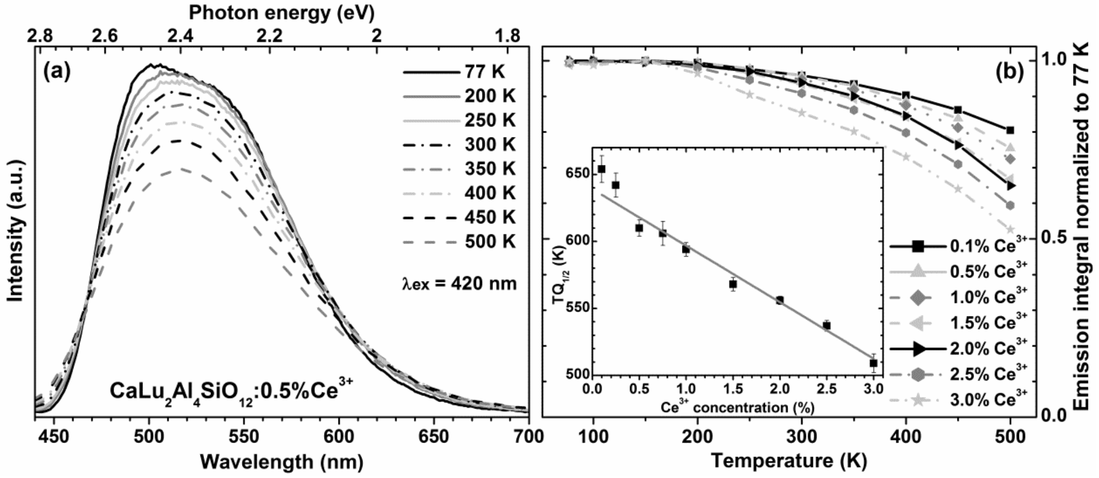

Figure 9.6 *(a) Temperature dependent emission spectra of* $CaLu_2Al_4SiO_{12}$*:0.5%*Ce^{3+} *and (b) thermal quenching of* $CaLu_2Al_4SiO_{12}$*:*Ce^{3+} *phosphors as a function of* Ce^{3+} *concentration. The inset shows calculated* $TQ_{1/2}$ *values for different* Ce^{3+} *concentrations.*

Figure 9.6a represents temperature dependent emission spectra of $CaLu_2Al_4SiO_{12}$:0.5%Ce^{3+} specimen. It turns out that emission intensity decreases with increasing temperatures. Moreover, the shoulder at higher energies observed in emission spectrum at 77 K vanishes at higher temperatures. This can be explained by increased energy transfer from the high energy emission band to the low energy emission band at elevated temperatures. This results in relative decrease of high energy emission intensity with respect to its low energy counterpart. Furthermore, a thermal broadening of emission band was also observed for all prepared samples.

The thermal quenching behaviour of the investigated phosphors as a function of Ce^{3+} concentration is shown in *Figure 9.6b*. A Boltzmann sigmoidal fit was employed for calculation of $TQ_{1/2}$ [44]. It is evident that the PL integrals decrease if temperature is increased. The sample with 0.1% of Ce^{3+} loses only 20% of its low-temperature emission intensity at 500 K (≈ 227 °C), whereas the sample with 3% of Ce^{3+} loses about 50%, showing that the thermal quenching becomes more severe at higher Ce^{3+} concentrations. The thermal quenching is either due to mutual energy transfer between the Ce^{3+} ions to the host lattice defect centres or due to the higher defect density upon increasing the Ce^{3+} concentration (see *Figure 9.4*). The re-absorption at higher Ce^{3+} concentrations increases due to emission spectra broadening and thus larger overlap between absorption and emission bands. The inset in *Figure 9.6b* depicts $TQ_{1/2}$ values of $CaLu_2Al_4SiO_{12}:Ce^{3+}$ phosphors with different Ce^{3+} concentrations obtained from the Boltzmann-sigmoidal fit. The $TQ_{1/2}$ values decrease almost linearly with increasing Ce^{3+} concentration.

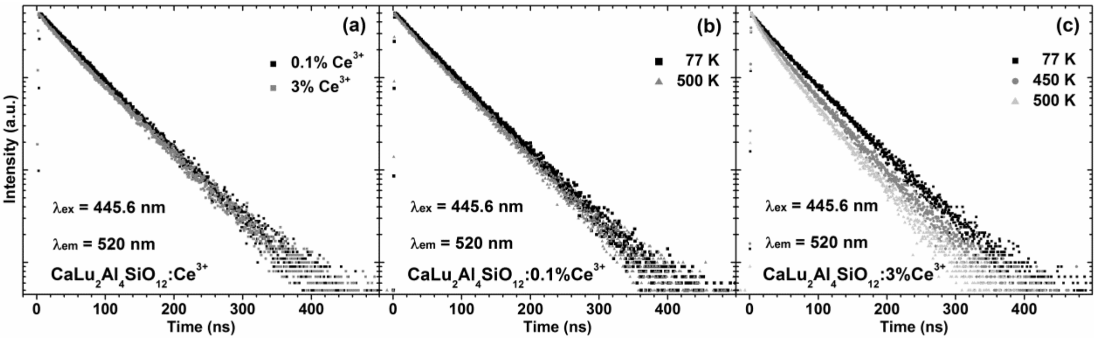

Figure 9.7 *(a) Decay curves of $CaLu_2Al_4SiO_{12}:Ce^{3+}$ as a function of Ce^{3+} concentration; (b) and (c) decay curves of samples doped with 0.1 and 3% of Ce^{3+}, respectively, as a function of temperature.*

Several temperature and/or Ce^{3+} concentration dependent decay curves of $CaLu_2Al_4SiO_{12}:Ce^{3+}$ phosphors are given in *Figure 9.7*. The decay curves of the specimen doped with 0.1 and 3% of Ce^{3+} are nearly identical (see *Figure 9.7a*), suggesting similar internal efficiency of Ce^{3+} ions at both concentrations. However, the decay curves change considerably at different temperatures. At low Ce^{3+} contents (*Figure 9.7b*) in the structure the decay constants obtained from measurements at 77 and 500 K are similar, thus indicating only slight decrease of efficiency. This is in good agreement with weak decrease of emission integrals shown in *Figure 9.6b*. Furthermore, at high Ce^{3+} contents the decay constant decreases considerably at elevated temperatures. This again indicates more severe temperature quenching of samples doped with high Ce^{3+} concentrations as was observed from emission integrals.

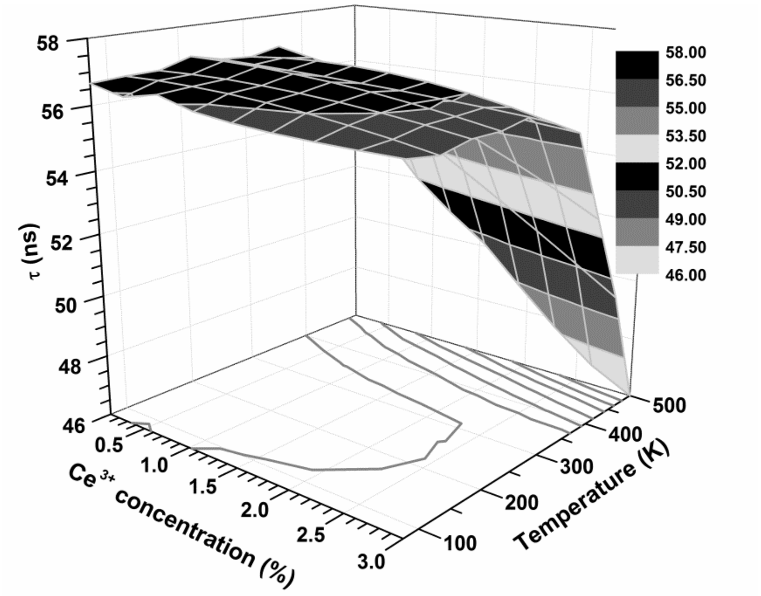

Figure 9.8 *$CaLu_2Al_4SiO_{12}:Ce^{3+}$ decay constants as a function of Ce^{3+} concentration and temperature.*

Figure 9.8 shows the 3D representation of $CaLu_2Al_4SiO_{12}:Ce^{3+}$ decay constants as a function of Ce^{3+} concentration and temperature. All decay curves were single-exponential. The PL decay constants are proportional to the rates of radiative and non-radiative transitions and, therefore, to the internal efficiency of the activator ions and deliver a deeper insight into the respective quenching mechanisms. The internal quantum efficiency of luminescent centre is given by [119]:

$$\eta = \frac{W_r}{W_r + W_{nr}} \qquad (Eq. 9.1)$$

where η is internal efficiency, W_r and W_{nr} are radiative and non-radiative transition rates, respectively. From low to moderate Ce^{3+} concentrations (up to 2 mol-%) decay times are constant up to 350 K, showing that no thermal quenching takes place. At temperatures above 350 K decay times start to decrease, indicating that the TQ sets in. At high Ce^{3+} concentrations the decay time decreases more strongly and the decrease sets in at lower temperatures. The lower quenching temperature can be explained by (thermally activated) concentration quenching. Thermal activation results from the increased overlap between excitation and emission spectra due to their broadening at higher temperatures. On the other hand, thermally activated trapping of the excitation energy by defects also plays a role [2, 194]. The measured decay times of $CaLu_2Al_4SiO_{12}:Ce^{3+}$ samples were shorter compared to LuAG:Ce (Philips) (τ_r = 58 ns). This is in line with the blue-shift of the emission spectrum and the increased probability for the transition due to the larger energy separation as expected by the impact on the Einstein coefficient [170].

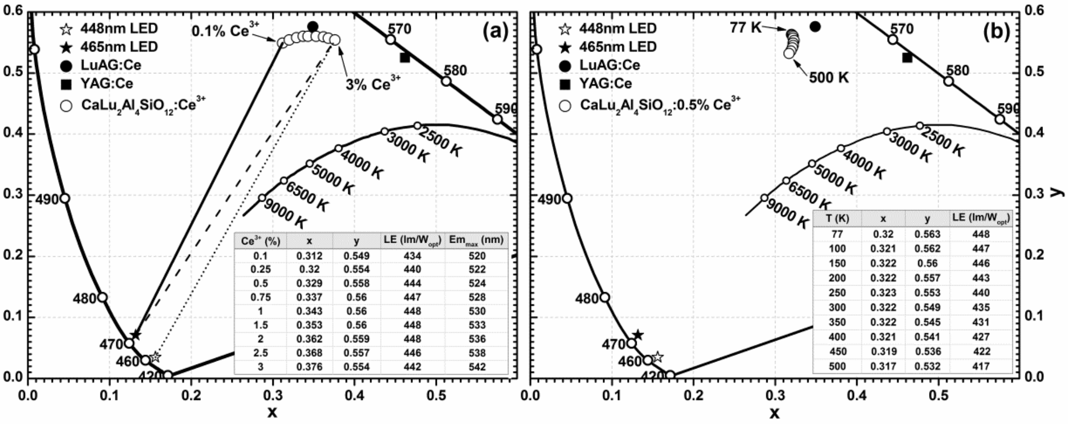

Ce^{3+} (%)	x	y	LE (lm/W_{opt})	Em_{max} (nm)
0.1	0.312	0.549	434	520
0.25	0.32	0.554	440	522
0.5	0.329	0.558	444	524
0.75	0.337	0.56	447	528
1	0.343	0.56	448	530
1.5	0.353	0.56	448	533
2	0.362	0.559	448	536
2.5	0.368	0.557	446	538
3	0.376	0.554	442	542

T (K)	x	y	LE (lm/W_{opt})
77	0.32	0.563	448
100	0.321	0.562	447
150	0.322	0.56	446
200	0.322	0.557	443
250	0.323	0.553	440
300	0.322	0.549	435
350	0.322	0.545	431
400	0.321	0.541	427
450	0.319	0.536	422
500	0.317	0.532	417

Figure 9.9 *Fragments of the CIE 1931 colour diagram with colour points of (a)* $CaLu_2Al_4SiO_{12}:Ce^{3+}$ *as a function of* Ce^{3+} *concentration (exact colour points, luminous efficacies and emission maximum for each* Ce^{3+} *concentration are given in inset table); (b)* $CaLu_2Al_4SiO_{12}:0.5\%Ce^{3+}$ *as a function of temperature (exact colour points and luminous efficacies for each temperature are given in inset table).*

Figure 9.9a represents the colour points of the $CaLu_2Al_4SiO_{12}:Ce^{3+}$ phosphors as a function of Ce^{3+} concentration as well as the colour points of LuAG:Ce, YAG:Ce, and LEDs emitting at 448 and 465 nm. Colour points of the target materials are distributed further from the edge of CIE 1931 colour diagram showing lower colour saturation if compared to YAG:Ce. With increasing Ce^{3+} concentration the colour points shift towards higher x values (from yellowish-green to yellow-green region) what is in line with the emission spectra shown in *Figure 9.5b*. It turned out that any combination of $CaLu_2Al_4SiO_{12}:Ce^{3+}$ phosphors with a 448 or a 465 nm emitting LED would not result in a white light source, because the respective colour gamut does not overlap with BBL. In order to obtain white light an additional red or orange emitting phosphor would be required. Luminous efficacies of the phosphors slightly increase with increasing activator concentration. This goes hand in hand with the observed red shift of emission following the same trend. This indicates a better overlap of the emission spectra with the human eye sensitivity curve (peaking at 555 nm). However, the luminous efficacy starts to diminish when the Ce^{3+} concentration exceeds 2 mol-%, even though the emission maxima have not reached the maximum of the human eye sensitivity curve. This is interpreted as a band broadening due to the higher probability of mutual Ce-Ce interactions, which broaden the spin-orbit split $[Xe]4f^1$ ground level (in emission) and the $[Xe]5d^1$ level (in excitation). The broader emission spectrum leads to smaller overlap with the human eye sensitivity curve and thus lowers LE values.

Figure 9.9b shows the fraction of the CIE 1931 chromaticity diagram with the colour points of $CaLu_2Al_4SiO_{12}$:0.5%Ce^{3+} phosphor at different temperatures. Taking into account the very broad temperature range, the colour points of the sample are rather stable, what is one of the requirements for LED phosphors. It was also observed that the LE values (see inset table in *Figure 9.9b*) decreased with increasing temperature. This is explained by the broadening of emission spectra upon temperature increase, thus smaller overlap with the human eye sensitivity curve, resulting in smaller LE values.

Quantum efficiencies of all prepared samples were calculated according to Eq. 5.1 and are shown in *Figure 9.10*. The highest efficiencies were obtained for samples doped with 0.25% or 0.5% of Ce^{3+}. An increased activator concentration resulted in gradual decrease in efficiency. The highest efficiency was 86% for the sample with 0.25% of Ce^{3+} sintered at 1450 °C. However, it should be noted, that all herein discussed samples were not completely optimized and even higher QE values could be possible to achieve, *i.e.* by choosing another synthesis method, modifying the Ce^{3+} concentration, optimizing the particle morphology, and so on.

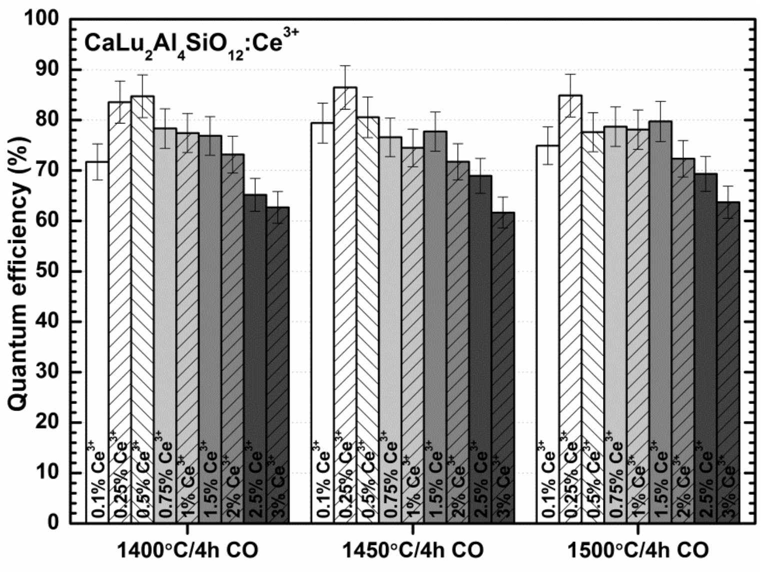

Figure 9.10 *Quantum efficiencies ($\lambda_{ex} = 450\,nm$) of CaLu$_2$Al$_4$SiO$_{12}$:Ce^{3+} phosphors as a function of Ce^{3+} concentration and sintering temperature.*

Chapter 10. $CaY_2Al_4SiO_{12}:Ce^{3+}$ Yellow Emitting Phosphors

10.1. TG/DTA, XRD, and SEM Data Analysis

The TG/DTA curves of Ca-Y-Al-Si-O precursor gel obtained after the combustion process are shown in *Figure 10.1*. The TG curve reveals that the mass loss occurs in two main steps similar to Ca-Lu-Al-Si-O gel described in *Figure 9.1*. The first step (peak at 536 °C) yielded in a mass loss of about 16% and can be attributed to burning of organic residues that remained after the combustion process. This is in line with the DTA curve (peak at 510 °C), which shows exothermic processes occurring in that temperature range. The second mass loss step of 6% takes place in the temperature range 800–1000 °C and can be attributed to the decomposition of metal carbonates or oxy-carbonates. This is in good agreement with the DTA curve showing endothermic processes in this temperature range.

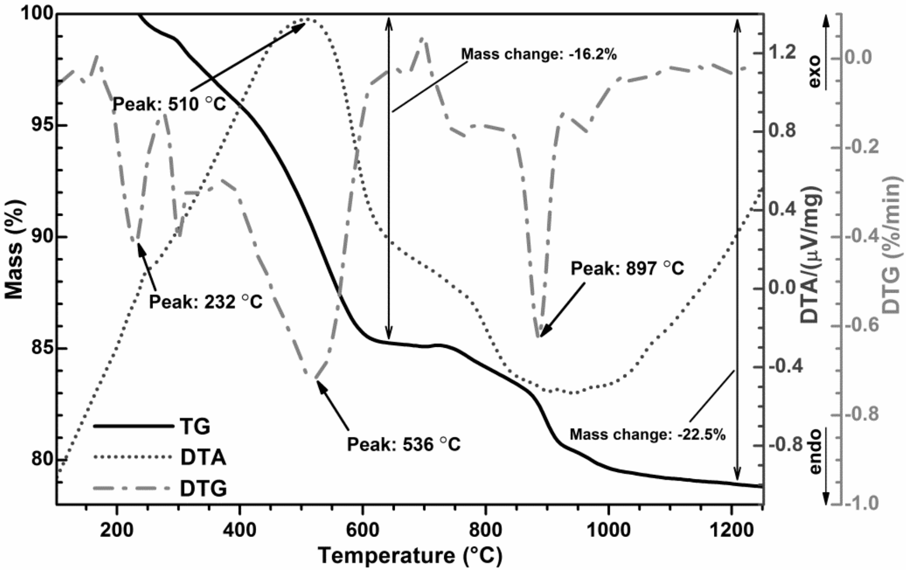

Figure 10.1 *TG/DTA curves of the Ca-Y-Al-Si-O precursor gel obtained after the combustion process.*

The XRD patterns of undoped $CaY_2Al_4SiO_{12}$ powders as a function of sintering temperature are shown in *Figure 10.2* along with a reference pattern of $Y_3Al_5O_{12}$ (PDF4+ (ICDD) 04-007-2667). During the combustion process no crystallization processes were observed. Annealing gel powders at 1000 °C for 2 h in air resulted in the formation of various silicate and aluminate phases.

Moreover, only very little garnet phase formation has been detected. This observation is very different from $CaLu_2Al_4SiO_{12}$ compounds where the garnet phase started to form already at 1000 °C [38]. Sintering the powders at 1200 °C resulted in nearly single phase garnet materials with $Ca_2Al_2SiO_7$ (PDF4+ (ICDD) 04-014-4683) as a minor secondary phase (marked with an asterisk in *Figure 10.2d*). However, subsequent sintering at 1400–1450 °C for 4 h resulted in single phase garnet type materials. Furthermore, no differences in the XRD patterns were observed if the synthesized phosphors were doped with Ce^{3+} (at least up to 3 mol-%). The samples sintered at temperatures higher than 1450 °C were molten, indicating that the melting point of these materials is close to this temperature.

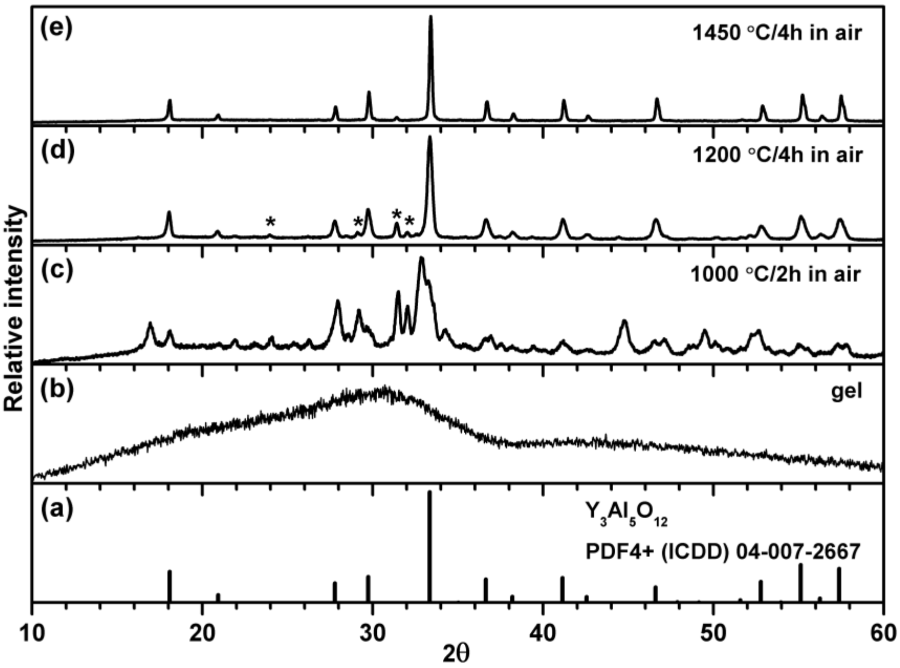

***Figure 10.2** XRD patterns of: (a) $Y_3Al_5O_{12}$ reference; (b) Ca-Y-Al-Si-O gel after combustion process; (c) sample annealed at 1000 °C for 2 h; and subsequently sintered for 4 h in air at (d) 1200 °C or (e) 1450 °C.*

The change of particle morphology of $CaY_2Al_4SiO_{12}$ with increasing sintering temperature was inspected by taking SEM pictures. Some of the obtained SEM images are depicted in *Figure 10.3*. The specimen annealed at 1000 °C possesses a sponge-like structure formed by highly agglomerated nano-scale particles. As expected, the particle growth was observed when sintering temperature was increased. The sample sintered at 1200 °C still possessed a sponge-like structure, but with larger and better shaped particles in comparison to sample annealed at 1000 °C. Finally, the sintering of specimen at 1450 °C has led to the formation of relatively large particles (~0.5−1.5 μm) with high level of particle size distribution. These large particles are formed from well crystallized and shaped sub-micrometer particles grown together.

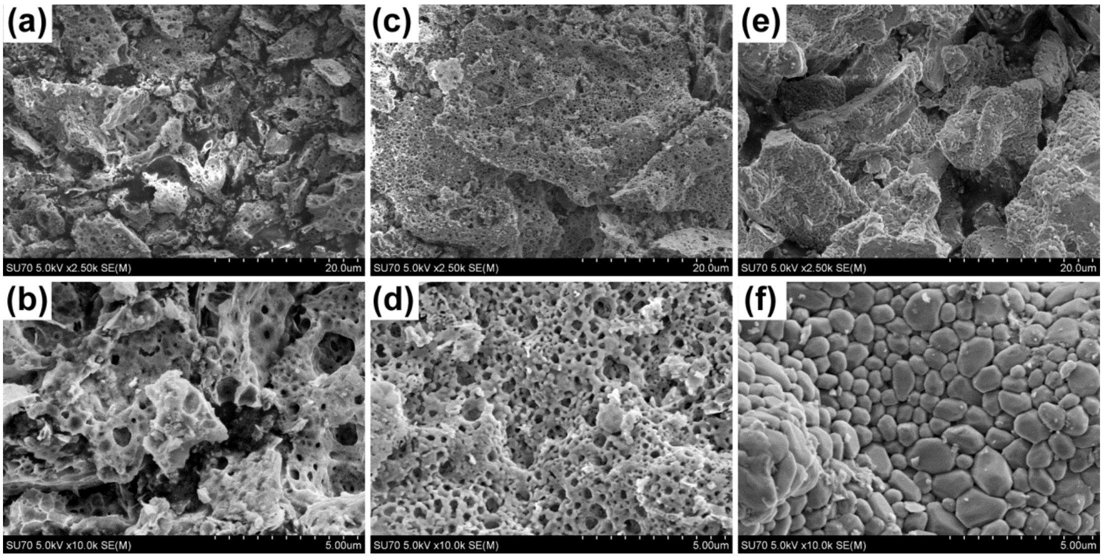

Figure 10.3 *SEM images of $CaY_2Al_4SiO_{12}$ samples sintered at 1000 °C under magnification of (a) ×2.5k and (b) ×10.0k; 1200 °C (c) ×2.5k and (d) ×10.0k; 1450 °C (e) ×2.5k and (f) ×10.0k.*

10.2. Optical Properties

The body colour of undoped $CaY_2Al_4SiO_{12}$ sample was white indicating that it does not absorb radiation in the visible spectral region. However, Ce^{3+} doped samples possessed yellowish to dark yellow body colour caused by the strong absorption of Ce^{3+} in the blue spectral region as confirmed by reflection spectra given in *Figure 10.4*. As expected, absorption increased with increasing the activator concentration. It was also observed that the absorption band of prepared phosphors is slightly shifted towards shorter wavelengths if compared to YAG:Ce (U728, Philips), 450 vs. 460 nm, respectively. One can thus draw the conclusion that the lowest 5d crystal-field component of Ce^{3+} in $CaY_2Al_4SiO_{12}$ host lattice lies at a higher energy than in YAG:Ce. Furthermore, the low level doped samples (up to 1% of Ce^{3+}) possess high brilliance because the reflectance at wavelengths longer than 540 nm is rather close to unity. However, the reflectance values of samples, doped with more than 1% of Ce^{3+}, decreased probably due to defect formation in the lattice, thus causing greyishing.

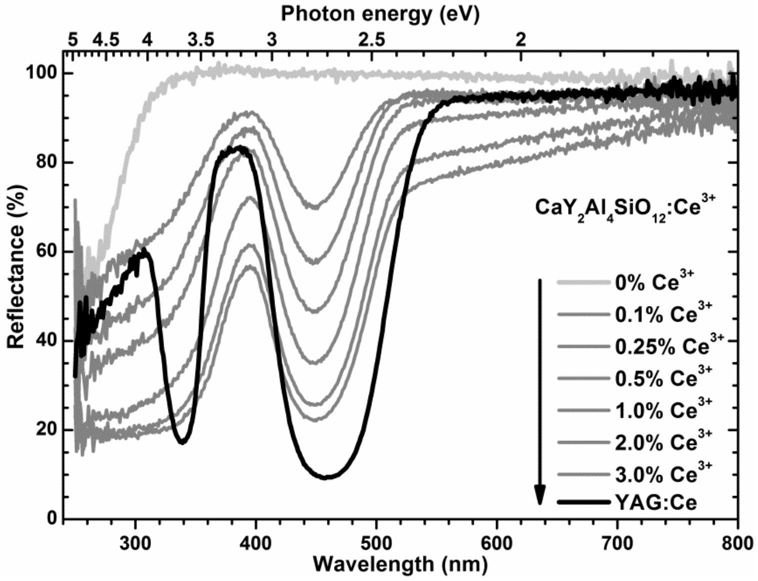

Figure 10.4 *Reflection spectra of $CaY_2Al_4SiO_{12}:Ce^{3+}$ powders sintered at 1450 °C as a function of Ce^{3+} concentration.*

Excitation spectra of synthesized samples as a function of Ce^{3+} concentration are given in *Figure 10.5a*. The spectrum of YAG:Ce standard material (U728, Philips) is also included for reference. The excitation spectra contain two broad bands attributed to the $[Xe]4f^1 \rightarrow [Xe]5d^1$ transitions of Ce^{3+} ions. However, the higher energy band is very weak if compared to its low energy counterpart. This is different from the excitation spectrum of YAG:Ce whose high and low energy bands are of nearly equal intensity. The observed phenomenon, as for $CaLu_2Al_4SiO_{12}:Ce^{3+}$ samples, is attributed to photoionization. Moreover, the optical band gap of $CaY_2Al_4SiO_{12}$ host lattice is ≈ 200 nm (6.20 eV), whereas the band gap of $Y_3Al_5O_{12}$ is 190 nm (6.53 eV) [163, 199], therefore, the phosphors under investigation are likely to suffer from photoionization at lower excitation energies in comparison to YAG:Ce. Furthermore, the distance between low and high energy bands in the excitation spectra of the prepared samples are smaller if compared to YAG:Ce, thus indicating that $CaY_2Al_4SiO_{12}$ host lattice generates a weaker crystal field on the dodecahedral sites than in YAG.

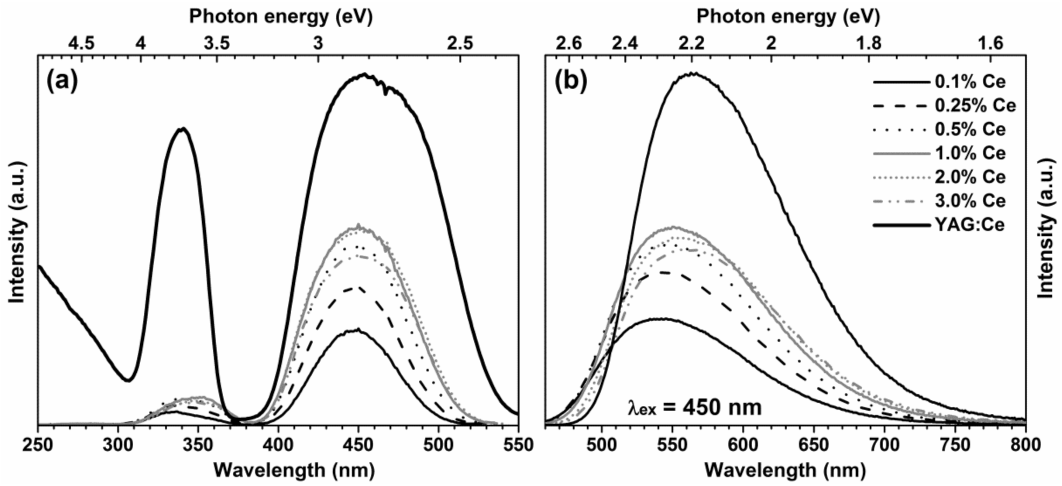

Figure 10.5 *Excitation (a) and emission (b) spectra of* $CaY_2Al_4SiO_{12}:Ce^{3+}$ *phosphors sintered at 1450 °C as a function of* Ce^{3+} *concentration.*

The emission spectra of the $CaY_2Al_4SiO_{12}:Ce^{3+}$ samples are shown in *Figure 10.5b*. As in $CaLu_2Al_4SiO_{12}:Ce^{3+}$ emission spectra depicted in *Figure 9.5b* they comprise one broad band, which is a result of the strong overlap of the two bands originating in the transitions from the lowest crystal-field component of the [Xe]$5d^1$ configuration to the spin–orbit split sublevels $^2F_{5/2}$ and $^2F_{7/2}$ of the [Xe]$4f^1$ configuration of Ce^{3+} ions [44, 193]. The emission intensity increased up to 1% of Ce^{3+} and started decreasing if higher activator concentrations were introduced into the host lattice. The drop of intensity at higher Ce^{3+} levels is attributed to concentration quenching. It is worth mentioning that concentration quenching in $CaY_2Al_4SiO_{12}:Ce^{3+}$ samples occurs at higher concentrations than in $CaLu_2Al_4SiO_{12}:Ce^{3+}$ samples [38], 1% and 0.5% of Ce^{3+}, respectively. Since the "$CaLu_2$" is smaller than the "CaY_2" site, the incorporation of a high Ce^{3+} concentration is more difficult and thus results in inhomogeneous distribution of the Ce^{3+} ions. It was also observed that emission maximum shifted from 542 to 560 nm if Ce^{3+} concentration was increased from 0.1% to 3%. Due to the incorporation of Ca^{2+}–Si^{4+} pairs into the host compound it might be that multiple Ce^{3+} centers are present in the $CaY_2Al_4SiO_{12}$ through the inherent disorder in the host. Therefore, there can be energy transfer from the high energy centers to low energy centers. Such energy migration becomes much more likely at higher Ce^{3+} concentrations, thus causing the red-shift of emission. For the Stokes shift and the splitting between the crystal-field components of the [Xe]5d^1 configuration of Ce^{3+} determination, excitation and emission spectra were recorded at 77 K for the sample doped with 0.1% of Ce^{3+}. The Stokes shift was measured in the exact way as it was done for CaLu$_2$Al$_4$SiO$_{12}$:0.1%Ce^{3+} sample described in Chapter 9.2 and gave a value of 2810 cm^{-1}, what is about 400 cm^{-1} larger than for YAG:Ce (2400 cm^{-1}) [2, 194]. A larger Stokes shift points to a larger relaxation during the [Xe]4f^1 → [Xe]5d^1 transition of Ce^{3+}, which is in line with the enlargement of the dodecahedral site by the incorporation of divalent calcium. The calculation of energy difference between the crystal-field components of the [Xe]5d^1 configuration in CaY$_2$Al$_4$SiO$_{12}$:0.1%Ce^{3+} and YAG:Ce [2, 194] yielded values of 7400 and 7500 cm^{-1}, respectively. The obtained results are in line with the blue shifted emission resulting from the lower crystal-field splitting.

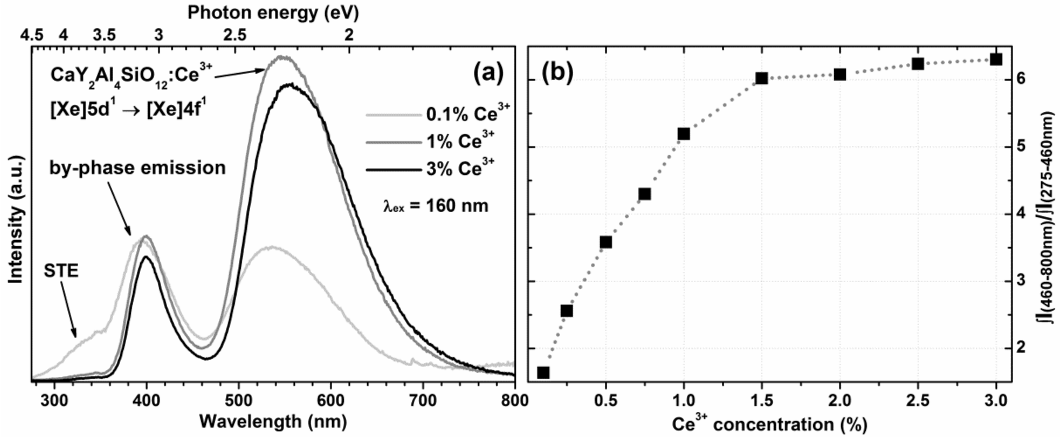

Figure 10.6 *(a) Emission spectra of* $CaY_2Al_4SiO_{12}:Ce^{3+}$ *upon 160 nm excitation, (b) the ratio of emission integrals in the ranges 460−800 nm and 275−460 nm as a function of* Ce^{3+} *concentration.*

The VUV emission spectra (λ_{ex} = 160 nm) are shown in *Figure 10.6a*. Even though no secondary phases were observed in the powder XRD patterns, the emission spectra clearly shows besides the band at ~540 nm originating from the CaY$_2$Al$_4$SiO$_{12}$:Ce^{3+} phase, an additional band peaking at 397 nm. This band likely originates from the secondary phase, which concentration is below the XRD detection limits. The emission spectra of the samples with a low Ce^{3+} concentration also contained a shoulder at ~340 nm, which was attributed to a self-trapped exciton (STE) emission. The shoulder vanishes at higher Ce^{3+} concentrations. It turned out that emission intensity of the secondary phase decreases with increasing Ce^{3+} concentration if compared to $CaY_2Al_4SiO_{12}:Ce^{3+}$ (see *Figure 10.6b*). This is in line with the expected increase of re-absorption of the 397 nm emission band of the unknown second phase by the absorption band of the Ce^{3+} doped garnet.

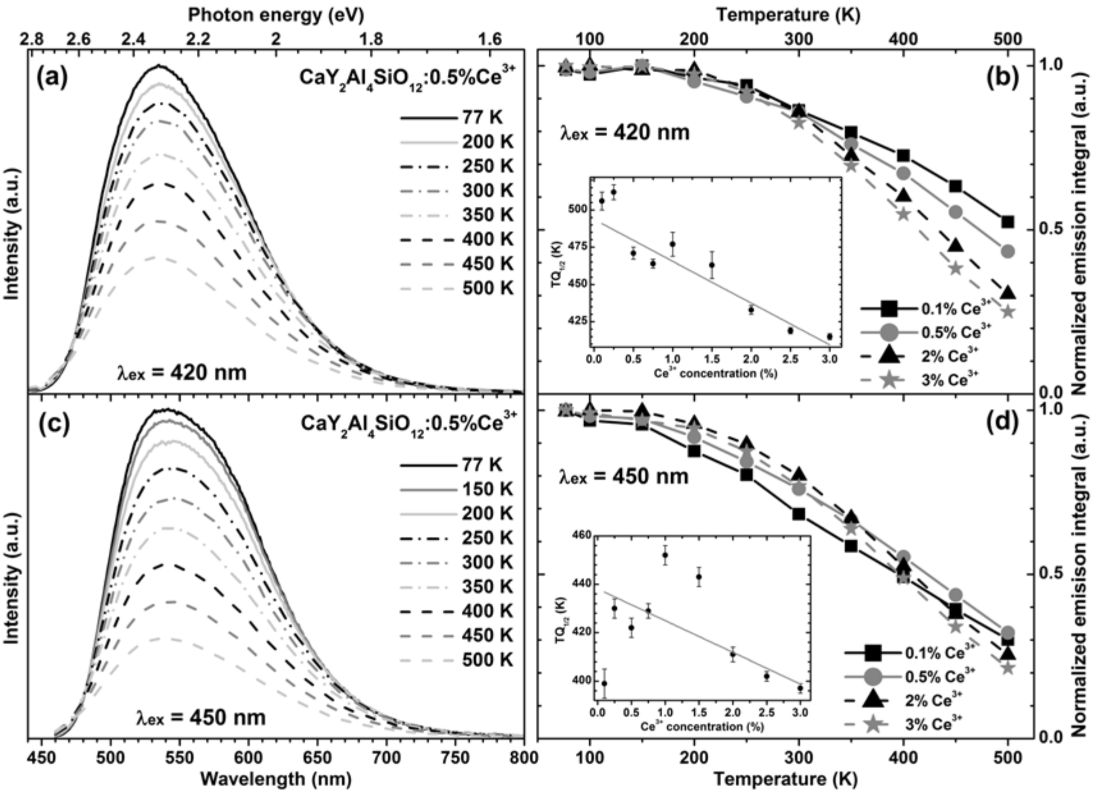

Figure 10.7 *(a) Temperature dependent emission spectra of $CaY_2Al_4SiO_{12}:0.5\%Ce^{3+}$ ($\lambda_{ex} = 420$ nm) and (b) thermal quenching of $CaY_2Al_4SiO_{12}:Ce^{3+}$ phosphors as a function of Ce^{3+} concentration ($\lambda_{ex} = 420$ nm) (the inset shows calculated $TQ_{1/2}$ values for different Ce^{3+} concentrations). (c) Temperature dependent emission spectra of $CaY_2Al_4SiO_{12}:0.5\%Ce^{3+}$ ($\lambda_{ex} = 450$ nm) and (d) thermal quenching of $CaY_2Al_4SiO_{12}:Ce^{3+}$ phosphors as a function of Ce^{3+} concentration ($\lambda_{ex} = 450$ nm) (the inset shows calculated $TQ_{1/2}$ values for different Ce^{3+} concentrations).*

Temperature dependent emission spectra of $CaY_2Al_4SiO_{12}:0.5\%Ce^{3+}$ specimen excited at 420 and 450 nm are shown in *Figure 10.7a* and *Figure 10.7c*, respectively. Emission intensity decreases with increasing temperature regardless of the excitation wavelength. However, the intensity decreases a little bit slower if sample is excited 420 nm. Moreover, the shape of the spectra also differs if excited at different wavelengths. Under 420 nm excitation the emission spectra looks rather symmetrical, whereas under 450 nm excitation a shoulder at longer wavelengths is observed, especially at lower temperatures. This indicates that the probability of emission of higher energy band is increased if excitation wavelength decreases (energy increases). Nevertheless, a possible explanation requires a more detailed study. Contrary to the temperature dependent emission spectra of $CaLu_2Al_4SiO_{12}$:0.5%Ce^{3+} sample showed in *Figure 9.6a*, where emission maximum shifted to longer wavelengths with increased temperatures, the emission spectra of $CaY_2Al_4SiO_{12}$:0.5%Ce^{3+} sample shows a slight shift of emission maxima towards shorter wavelengths. This can be explained by faster quenching of low energy emission band if compared to its high energy counterpart. Furthermore, a thermal broadening of emission band was observed for all samples regardless the Ce^{3+} concentration and excitation wavelength.

The TQ behaviour of the $CaY_2Al_4SiO_{12}:Ce^{3+}$ phosphors as a function of Ce^{3+} concentration under excitation at 420 and 450 nm is shown in *Figure 10.7b* and *Figure 10.7d*, respectively. A Boltzmann sigmoidal fit was employed for the calculation of $TQ_{1/2}$ values. The PL integrals decreased with increasing temperature regardless the concentration of Ce^{3+} and excitation wavelength. However, the excitation at 420 nm resulted in slower integral decrease if compared to the results obtained for 450 nm excitation. The calculated $TQ_{1/2}$ values are also rather different for 420 and 450 nm excitation and are given in the inset graphs of *Figure 10.7b* and *Figure 10.7d*, respectively. The decrease of $TQ_{1/2}$ values as a function of Ce^{3+} concentration is almost linear if samples are excited at 420 nm. Nevertheless, no similar trend was observed if samples were excited at 450 nm. Yet, it is clear that TQ becomes more severe at higher Ce^{3+} concentrations. The thermal quenching is caused either by mutual energy transfer between the Ce^{3+} ions to the host lattice defect centres or the higher defect density upon increasing the Ce^{3+} concentration (see *Figure 10.4*) [38].

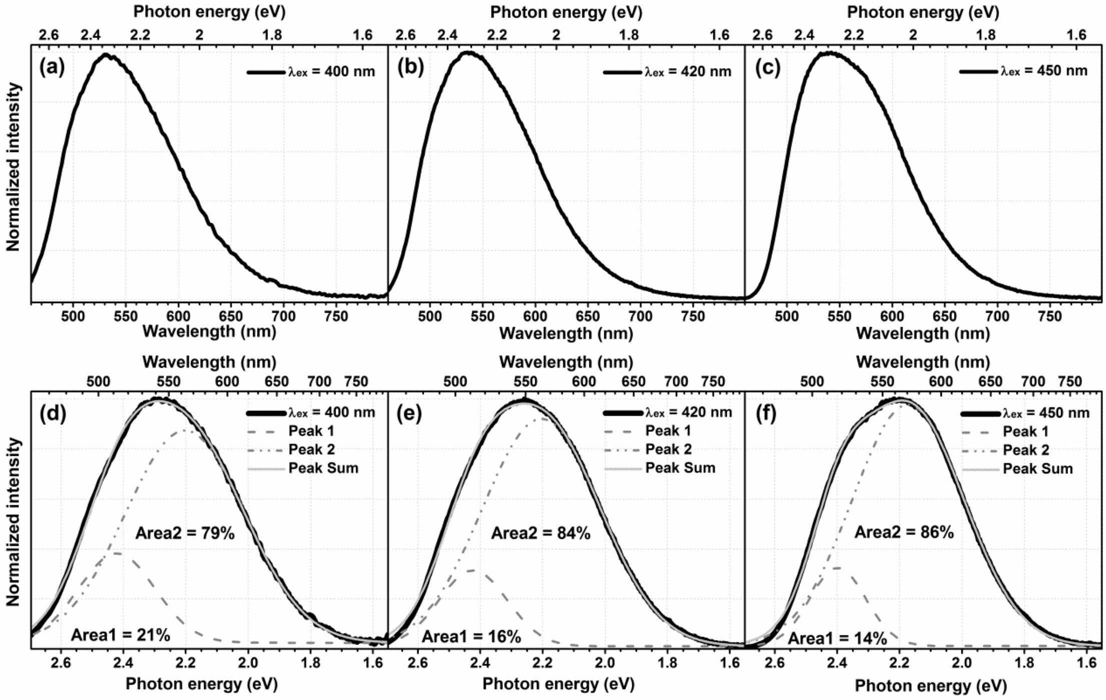

Figure 10.8 *Emission spectra of* $CaY_2Al_4SiO_{12}$*:0.5%*Ce^{3+} *measured at 77 K under different excitation wavelengths: (a) 400 nm, (b) 420 nm and (c) 450 nm; (d), (e) and (f) depicts the peak fitting results of the respective graphs in the energy scale.*

The observed shift of the emission maximum if excited at different wavelengths was studied in more detail, because shifting emission spectra leads to the shift of color points, which in turn directly influence the color point and rendering of white light source. The emission spectra were recorded at 77 K and are given in *Figure 10.8a-c*. It is obvious, that emission spectrum, recorded for 400 nm excitation, is rather symmetrical. Moreover, the intensity is quite high already at 460 nm, indicating the stronger intensity of higher energy emission band. However, with increasing excitation wavelength, *i.e.* decreasing energy, the intensity at 460 nm decreases and is completely gone if excited at 450 nm. Moreover, the emission band broadens with increasing excitation wavelength and the shoulder around 580 nm appears if excited at 450 nm. The recorded emission spectra were fitted by two Gaussian functions in order to observe the intensity change of low and high energy bands. Before the fitting procedure the wavelength scale was converted to energy scale and the intensity per wavelength interval was converted to intensity per energy interval by applying Eq. 8.1 [137]. The fitting results are shown in *Figure 10.8d-f*. It turned out that the intensity of higher energy band decreases with increasing excitation wavelength. Moreover, the area of the high energy band also decreased from 21% to 14% with increasing excitation wavelength from 400 to 450 nm, respectively. Since the emission spectra are clearly dependent on the excitation wavelength, it was assumed that in these garnet samples Ce^{3+} occupies at least two positions, which have a different local environment, even though the garnet structure only offers one dodecahedral site. The presence of two different Ce^{3+} sites might be caused by a non-homogeneous distribution of the activator ions inside the host material, *i.e.* there might be isolated Ce^{3+} ions on the one hand and Ce^{3+} ions close to the another Ce^{3+} ion on the other hand. The slight difference in the crystallographic environment can thus explain the difference in the transition probabilities for the $[Xe]5d^1 \rightarrow [Xe]4f^1$ ($^2F_{7/2}$) and $[Xe]5d^1 \rightarrow [Xe]4f^1$ ($^2F_{5/2}$) transition.

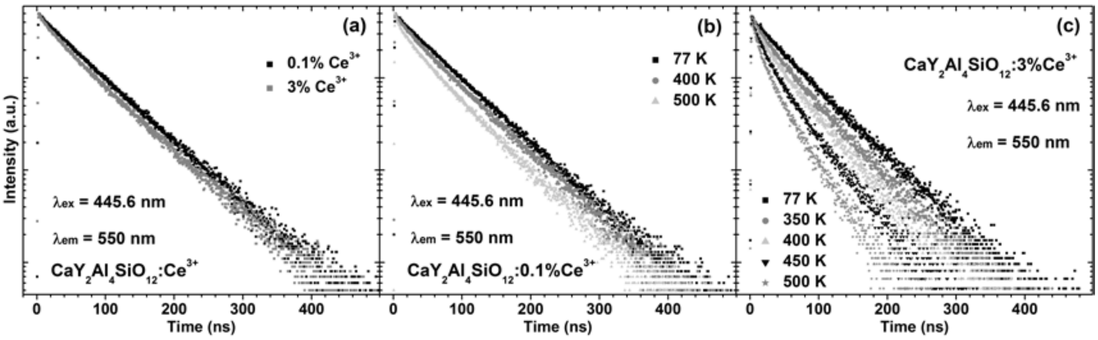

Figure 10.9 *(a) Decay curves of $CaY_2Al_4SiO_{12}:Ce^{3+}$ as a function of Ce^{3+} concentration; (b) and (c) decay curves of samples doped with 0.1% and 3% of Ce^{3+}, respectively, as a function of temperature.*

Several temperature and/or Ce^{3+} concentration dependent decay curves of $CaY_2Al_4SiO_{12}:Ce^{3+}$ phosphors are shown in *Figure 10.9*. The decay curves of the samples doped with 0.1% and 3% of Ce^{3+} are almost identical (see *Figure 10.9a*) if measured at RT, thus suggesting similar internal efficiency. Yet, the decay curves change considerably at different temperatures. At low Ce^{3+} concentration (*Figure 10.9b*) the decay curves experience only a slight change with increasing temperature. However, the decay curves of 3% Ce^{3+} doped sample depicted in *Figure 10.9c* become much steeper with increasing temperature what shows the faster decay time and, therefore, the reduced internal efficiency of Ce^{3+}. The more pronounced quenching at higher Ce^{3+}

concentrations is in good agreement with the results obtained from emission integrals (see *Figure 10.7b*).

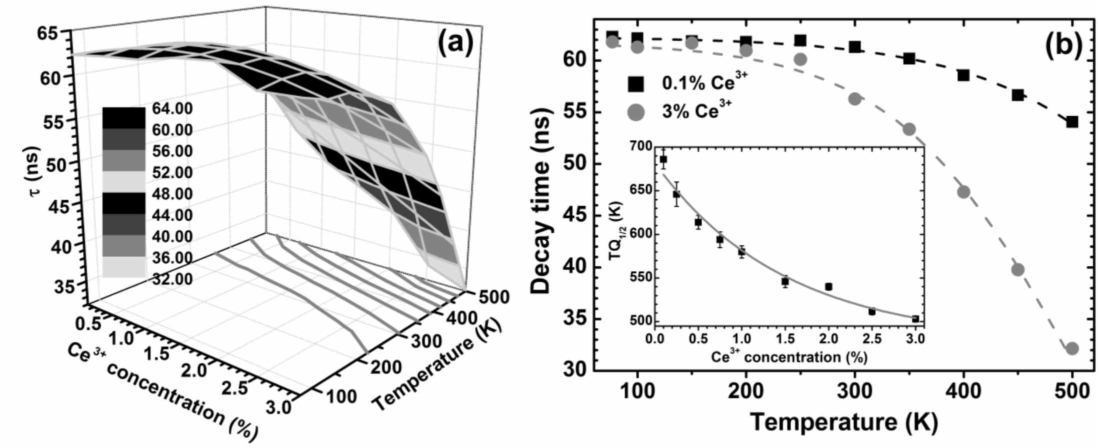

Figure 10.10 *(a) $CaY_2Al_4SiO_{12}$:Ce^{3+} decay constants as a function of Ce^{3+} concentration and temperature. (b) $TQ_{1/2}$ estimation from decay times (inset shows $TQ_{1/2}$ values as a function of Ce^{3+} concentration).*

The 3D representation of $CaY_2Al_4SiO_{12}$:Ce^{3+} decay times as a function of Ce^{3+} concentration and temperature is shown in *Figure 10.10a*. All decay curves were mono-exponential except those for high Ce^{3+} concentrations and high temperatures. As was already mentioned in the previous chapter, the PL decay constants are proportional to the probabilities of radiative and non-radiative transitions and thus to the internal efficiency of the activator. At low temperatures the decay times are nearly identical regardless of the Ce^{3+} concentration indicating similar efficiency. Similar to temperature dependent emission integrals the decay times start decreasing with increasing temperature. However, the decrease is much faster for the samples containing high Ce^{3+} concentrations indicating stronger thermal quenching for those specimens. This is in good agreement with the emission integrals depicted in *Figure 10.7b*. The lower quenching temperature can be explained by (thermally activated) concentration quenching. Thermal activation results from the increased overlap between excitation and emission spectra due to their broadening at higher temperatures [38]. On the other hand, thermally activated trapping of the excitation energy by defects also plays a role [2, 194]. The measured decay times of $CaY_2Al_4SiO_{12}$:Ce^{3+} specimens were slightly shorter if compared to YAG:Ce (U728, Philips) (τ_r = 67 ns). This goes hand in hand with the slight blue-shift of the emission spectrum and the increased probability for the transition due to the larger energy separation as expected by the impact on the Einstein coefficient [170].

Figure 10.10b shows Boltzmann-sigmoidal fit for the samples doped with 0.1 and 3% of Ce^{3+}. As discussed in the previous paragraph the more severe TQ was observed for the sample with high Ce^{3+} concentration. The $TQ_{1/2}$ values calculated from the temperature dependent decays are given in the inset graph of *Figure 10.10b*. However, these values are around 100 K higher than those obtained from emission integrals. This clearly shows that the internal efficiency of Ce^{3+} ions decreases much slower than it was anticipated from emission integral data, which corresponds to the external efficiency of the phosphor. Therefore, the faster decrease of external efficiency is caused by decreased escape efficiency:

$$EQE = IQE \times \eta_{esc} \qquad (Eq. 10.1)$$

where EQE and IQE are external and internal quantum efficiencies, respectively, and η_{esc} is escape efficiency. This is in good agreement with reflection spectra given in *Figure 10.4*, which shows rising defect concentration upon Ce^{3+} concentration increase. Higher defect concentration means that there are more quenching sites for emitted photons and, therefore, lower escape efficiency. The $TQ_{1/2}$ values calculated from decay constants decreased exponentially with increasing Ce^{3+} concentration, whereas a linear decrease was observed for those values calculated from emission integrals.

The colour points of $CaY_2Al_4SiO_{12}:Ce^{3+}$ samples as a function of Ce^{3+} concentration are shown in *Figure 10.11a*. The colour points of YAG:Ce, LuAG:Ce, and LEDs emitting at 448 and 465 nm were also added for reference. The colour points of the target materials are located between LuAG:Ce and YAG:Ce. Furthermore, they are distributed further from the edge of CIE 1931 colour diagram indicating lower colour saturation if compared to YAG:Ce standard material. However, with increasing Ce^{3+}

concentration the colour points shift closer to that of YAG:Ce which is in good agreement with concentration dependent emission spectra (see *Figure 10.5b*), where the red shift of emission maxima was observed upon increasing Ce^{3+} concentration. The combination of 465 nm emitting LED and low level doped phosphor powders would not result in a white emitting solid state light source since the respective colour gamut does not overlap with BBL. On the other hand, the line connecting colour points of 465 nm emitting LED and 3% of Ce^{3+} doped sample does cross the BBL. Such a light source would possess a colour temperature around 9000 K, which is way too high for the application in indoor lighting. Moreover, the combination of 448 nm emitting LED and 3% of Ce^{3+} doped sample would result in the light source with the colour point of ≈ 5000 K, which is still too high. Therefore, in all cases the additional orange or red emitting phosphor would be required to decrease the colour temperature and improve the CRI of the device.

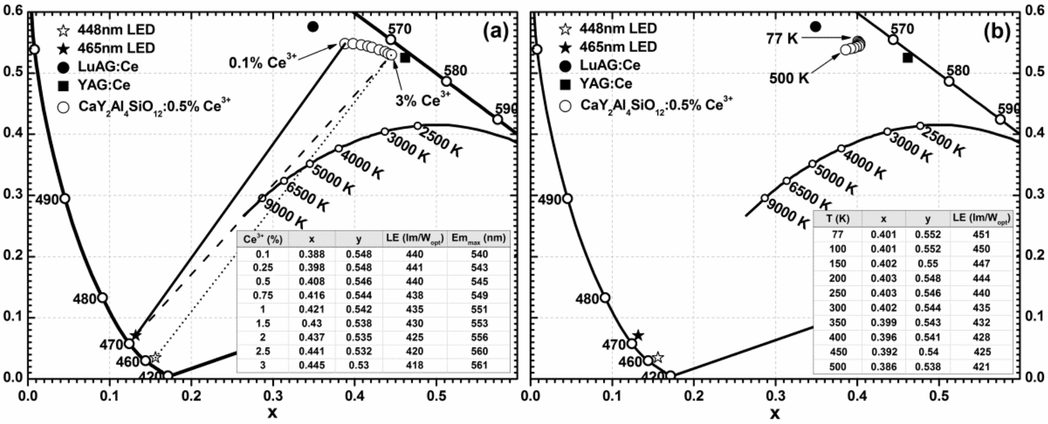

Ce^{3+} (%)	x	y	LE (lm/W_{opt})	Em_{max} (nm)
0.1	0.388	0.548	440	540
0.25	0.398	0.548	441	543
0.5	0.408	0.546	440	545
0.75	0.416	0.544	438	549
1	0.421	0.542	435	551
1.5	0.43	0.538	430	553
2	0.437	0.535	425	556
2.5	0.441	0.532	420	560
3	0.445	0.53	418	561

T (K)	x	y	LE (lm/W_{opt})
77	0.401	0.552	451
100	0.401	0.552	450
150	0.402	0.55	447
200	0.403	0.548	444
250	0.403	0.546	440
300	0.402	0.544	435
350	0.399	0.543	432
400	0.396	0.541	428
450	0.392	0.54	425
500	0.386	0.538	421

Figure 10.11 *Fragments of the CIE 1931 colour diagram with colour points of (a)* $CaY_2Al_4SiO_{12}:Ce^{3+}$ *as a function of* Ce^{3+} *concentration (exact colour points, luminous efficacies and emission maximum for each* Ce^{3+} *concentration are given in inset table); (b)* $CaY_2Al_4SiO_{12}:0.5\%Ce^{3+}$ *as a function of temperature (exact colour points and luminous efficacies for each temperature are given in inset table).*

It was observed that the calculated LE values of the $CaY_2Al_4SiO_{12}:Ce^{3+}$ phosphors decrease with increasing its Ce^{3+} concentration. This is in good agreement with the red shift of emission maxima following the same trend. The red-shifted emission results in lower overlap between emission spectra and human eye sensitivity curve resulting in decreasing LE values. Moreover, the increase of the Ce^{3+} concentration also results in broadening of the emission spectra, thus also influencing the decrease of LE values [38]. The relationship between Ce^{3+} dependent colour points, LE values and emission maxima of $CaY_2Al_4SiO_{12}:Ce^{3+}$ phosphors is summarized in the inset table of *Figure 10.11a*.

The fraction of the CIE 1931 colour diagram with the temperature dependent colour points of $CaY_2Al_4SiO_{12}:0.5\%Ce^{3+}$ phosphor is shown in *Figure 10.11b*. By taking the very broad temperature range into consideration, the colour points of the sample are relatively stable, what is one of the key requirements for LED phosphors. The LE values (see inset table in *Figure 10.11b*) decreased with increasing temperature. This is explained by the broadening of emission spectra upon increase of the temperature, hence smaller overlap with the human eye sensitivity curve, leading to smaller LE values.

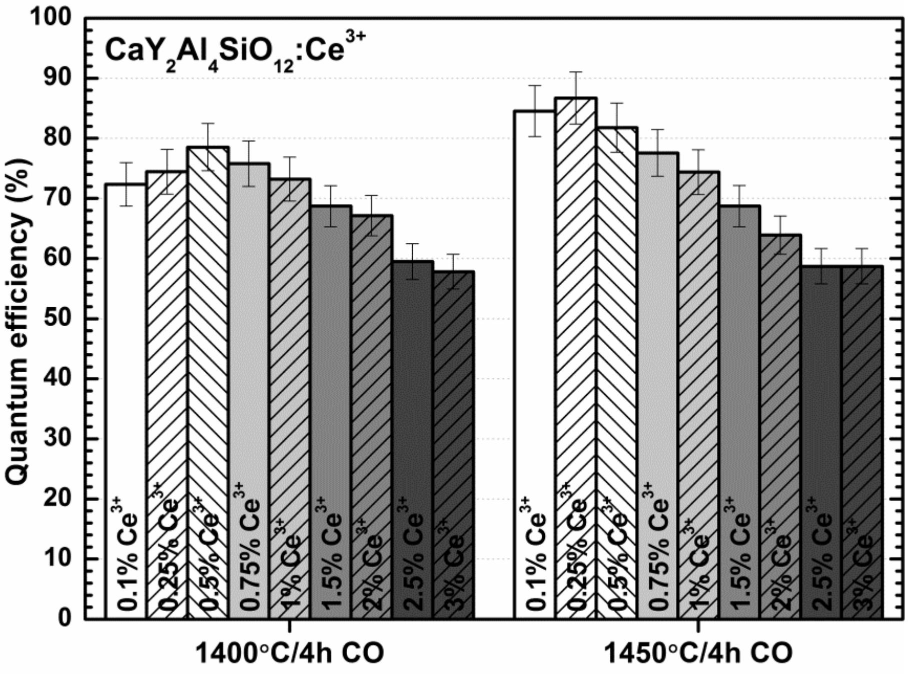

Figure 10.12 *Quantum efficiencies ($\lambda_{ex} = 450$ nm) of $CaY_2Al_4SiO_{12}:Ce^{3+}$ phosphors as a function of Ce^{3+} concentration and sintering temperature.*

Quantum efficiencies of the $CaY_2Al_4SiO_{12}:Ce^{3+}$ samples as a function of Ce^{3+} concentration and sintering temperature were calculated employing Eq. 5.1. The obtained results are depicted in *Figure 10.12*. The samples sintered at 1450 °C possessed higher efficiency than those sintered at 1400 °C. The increased activator concentration leads to steady decrease in efficiency. The sample doped with 0.25% of Ce^{3+} (1450 °C) showed the highest efficiency (≈ 86%). However, further increase of the quantum efficiency still could be achieved by choosing another synthesis method, modifying Ce^{3+} concentration, optimizing the particle morphology, and so on [38].

Chapter 11. Conclusions

1. $Ba_2(Zr,Hf)_2Si_3O_{12}:Eu^{2+}$ samples were prepared by high temperature solid state synthesis method and the phase purity was confirmed by powder XRD measurements. A solid solution without a miscibility gap was obtained at any Zr^{4+}/Hf^{4+} ratio due to close ionic radii of both ions.
2. $Ba_2(Zr,Hf)_2Si_3O_{12}:Eu^{2+}$ phosphors exhibit blue-cyan emission upon near-UV excitation. The emission originates from the $[Xe]4f^65d^1 \rightarrow [Xe]4f^7$ transition of Eu^{2+} and can be tuned Zr/Hf ratio or Eu^{2+} concentration. The traces of Eu^{3+} are still present in the materials despite of annealing under reducing conditions.
3. The calculated $TQ_{1/2}$ values for $Ba_2Zr_2Si_3O_{12}:2\%Eu^{2+}$ and $Ba_2Hf_2Si_3O_{12}:1\%Eu^{2+}$ were 260 K (−13 °C) and 445 K (172 °C), respectively. The highest QE value of 62% was obtained for the $Ba_2Hf_2Si_3O_{12}:0.5\%Eu^{2+}$ sample.
4. The red emitting $Li_3Ba_2La_3(MoO_4)_8:Eu^{3+}$ phosphors were prepared by solid state reaction at 800 °C. Powder XRD measurements confirmed that single phase materials were obtained at any La^{3+}/Eu^{3+} ratio.
5. The strongest emission lines originate from the electric-dipole ${}^5D_0 \rightarrow {}^7F_2$ transition of Eu^{3+} ion. The highest emission intensity was obtained for the sample doped with 90% of Eu^{3+}. Samples with Eu^{3+} concentrations of 70%, 80% and 90% showed a QE close to 100% upon 465 nm excitation. The calculated CIE 1931 colour points indicated a very high colour saturation. The calculated $TQ_{1/2}$ value for the $Li_3Ba_2Eu_3(MoO_4)_8$ specimen was 515 K (242 °C).
6. The prepared $Li_3Ba_2Eu_3(MoO_4)_8$ ceramics were highly excitable with the 380 nm emitting LED and showed bright red emission and are thus nicely applicable as a radiation converter onto near UV emitting LED chips.
7. $(Y,Lu)_3Al_3MgSiO_{12}:Ce^{3+}$ samples were prepared by aqueous sol-gel method employing 1,2-ethanediol as complexing agent. The powder XRD measurements revealed that single phase target materials at any Y/Lu ratio were obtained after sintering at 1600 °C under CO atmosphere.

8. Phosphors exhibit green to orange emission originating from the spin and parity allowed [Xe]5d^1 → [Xe]4f^1 transition of Ce^{3+} ions. The position of emission band can be tuned by Y/Lu ratio and/or Ce^{3+} concentration. The stronger TQ is observed for the samples with red shifted emission. The highest QE values of ~ 85% were obtained for $Lu_3Al_3MgSiO_{12}:Ce^{3+}$ samples doped with 0.25% and 0.5% of Ce^{3+}.
9. $CaLu_2Al_4SiO_{12}:Ce^{3+}$ samples were prepared by aqueous sol-gel combustion method employing THMAM as complexing agent and fuel. Single phase garnet materials were obtained after sintering gels at 1500 °C under CO atmosphere.
10. Phosphors showed green emission upon excitation at 450 nm. The emission of $CaLu_2Al_4SiO_{12}:Ce^{3+}$ specimens was blue shifted if compared to LuAG:Ce due to decreased crystal field strength. The concentration quenching sets in at rather low Ce^{3+} concentrations. The $TQ_{1/2}$ values decrease linearly with increasing Ce^{3+} concentration. The highest obtained QE value was 86% for the $CaLu_2Al_4SiO_{12}:0.25\%Ce^{3+}$ sample.
11. $CaY_2Al_4SiO_{12}:Ce^{3+}$ samples were synthesized by aqueous sol-gel combustion method employing THMAM as complexing agent and fuel. Powder XRD measurements confirmed that single phase target materials were obtained after sintering gels at 1450 °C under CO atmosphere.
12. Phosphors possess yellow emission if excited at 450 nm. The emission band is blue shifted in comparison with conventional YAG:Ce. The blue shift of emission is observed if samples are excited with shorter wavelengths (higher energies). The stronger TQ was observed for the samples possessing a higher Ce^{3+} concentration. The sample doped with 0.25% of Ce^{3+} showed the highest QE of 86%. The calculated CIE 1931 colour points showed little dependency on the temperature but high dependency on Ce^{3+} concentration.

Chapter 12. List of Publications and Conference Participation

12.1. Publications Included in the Thesis

12.1.1. Journal Articles

1. **A. Katelnikovas**, H. Winkler, A. Kareiva, T. Jüstel. “Synthesis and optical properties of green to orange tunable garnet phosphors for pcLEDs”. *Optical Materials* **33** (2011) 992.
2. V. Tomkute, **A. Katelnikovas**, H. Bettentrup, A. Kareiva, T. Jüstel. “Synthesis and luminescent properties of novel $Ba_{2-x}Eu_xZr_{2-y}Hf_ySi_3O_{12}$ phosphor”. *Optical Materials* **33** (2011) 1272.
3. **A. Katelnikovas**, J. M. Ogiegło, H. Winkler, A. Kareiva, T. Jüstel. “Synthesis of $Y_{3-x}Lu_xAl_3MgSiO_{12}$ garnet powders by sol-gel method”. *Journal of Sol-Gel Science and Technology* **59** (2011) 311.
4. **A. Katelnikovas**, J. Plewa, D. Dutczak, S. Möller, D. Enseling, H. Winkler, A. Kareiva, T. Jüstel. “Synthesis and optical properties of green emitting garnet phosphors for phosphor-converted light emitting diodes”. *Optical Materials* **34** (2012) 1195.
5. **A. Katelnikovas**, J. Plewa, S. Sakirzanovas, D. Dutczak, D. Enseling, F. Baur, H. Winkler, A. Kareiva, T. Jüstel. “Synthesis and optical properties of $Li_3Ba_2La_3(MoO_4)_8{:}Eu^{3+}$ powders and ceramics for pcLEDs”. *Journal of Materials Chemistry* **22** (2012) 22126.
6. **A. Katelnikovas**, S. Sakirzanovas, D. Dutczak, J. Plewa, D. Enseling, H. Winkler, A. Kareiva, T. Jüstel. “Synthesis and optical properties of yellow emitting garnet phosphors for pcLEDs”. *Journal of Luminescence* (2012) (accepted for publication).

12.1.2. Attended Conferences

1. **A. Katelnikovas**, H. Winkler, A. Kareiva, T. Jüstel. “Synthesis and optical properties of $CaY_2Al_4SiO_{12}{:}Ce^{3+}$”. *ICfE 7 – 7th International Conference on f Elements*. Cologne, Germany, August 23-27, (2009) P05-33-201.

2. **A. Katelnikovas**, T. Jüstel, A. Kareiva. “Synthesis and optical properties of $Ba_2Zr_2Si_3O_{12}$:Eu^{2+}”. *9th National Lithuanian Conference “CHEMIJA 2009*”. Vilnius, Lithuania, October 16, (2009) 30.
3. **A. Katelnikovas**, H. Winkler, A. Kareiva, T. Jüstel. “Synthesis and optical properties of green to orange tunable garnet phosphors for pcLEDs”. *European Materials Research Society (E-MRS) Spring Meeting*. Strasbourg, France, June 7-11, (2010) K-5.
4. **A. Katelnikovas**, D. Uhlich, H. Bettentrup, J. Plewa, A. Kareiva, T. Jüstel. “On the correlation between the composition of garnet type materials and their photoluminescence properties”. *6th Laser Ceramics Symposium*. Münster, Germany, December 6-8, (2010) 27.
5. **A. Katelnikovas,** A. Kareiva, T. Jüstel. “Synthesis and optical properties of $CaLu_2Al_4SiO_{12}$ doped by Ce^{3+}”. *Chemistry 2011. 10th International conference of Lithuanian Chemists*. Vilnius, Lithuania, October 14-15, 2011, 83.
6. **A. Katelnikovas**, H. Winkler, A. Kareiva, T. Jüstel. “On the efficient luminescence of rare earth doped molybdates”. *ICfE 8 - 8th International Conference on f-Elements*. Udine, Italy, August 26-31, (2012) OPT 32O.

12.2. Publications Not Included in the Thesis

12.2.1. Journal Articles

1. **A. Katelnikovas**, L. Grigorjeva, D. Millers, V. Pankratov, A. Kareiva. “Sol-gel preparation of nanocrystalline $CaWO_4$”. *Lithuanian Journal of Physics* **47** (2007) 63.
2. **A. Katelnikovas**, J. Barkauskas, F. Ivanauskas, A. Beganskiene, A. Kareiva. “Aqueous sol-gel synthesis route for the preparation of YAG: evaluation of sol-gel process by mathematical regression model”. *Journal of Sol-Gel Science and Technology* **41** (2007) 193.

3. E. Garskaite, N. Dubnikova, **A. Katelnikovas**, J. Pinkas, A. Kareiva. “Syntheses and characterisation of $Gd_3Al_5O_{12}$ and $La_3Al_5O_{12}$ garnets”. *Collection of Czechoslovak Chemical Communications* **72** (2007) 321.
4. **A. Katelnikovas**, P. Vitta, P. Pobedinskas, G. Tamulaitis, A. Žukauskas, J.-E. Jørgensen, A. Kareiva. “Photoluminescence in sol–gel-derived YAG:Ce phosphors”. *Journal of Crystal Growth* **304** (2007) 361.
5. **A. Katelnikovas**, A. Kareiva. “Low-temperature synthesis of lutetium gallium garnet (LGG) using sol-gel technique”. *Materials Letters* **62** (2008) 1655.
6. **A. Katelnikovas**, T. Jüstel, D. Uhlich, J.-E. Jørgensen, S. Sakirzanovas, A. Kareiva. “Characterization of cerium-doped yttrium aluminium garnet nanopowders synthesized via sol-gel process”. *Chemical Engineering Communications* **195** (2008) 758.
7. J. Plewa, **A. Katelnikovas**, T. Jüstel. “On the luminescence of $Lu_{3-x}Pr_xAl_5O_{12}$ ceramic bodies”. *Materiały Ceramiczne / Ceramic Materials* **60** (2008) 229.
8. **A. Katelnikovas**, H. Bettentrup, D. Uhlich, S. Sakirzanovas, T. Jüstel, A. Kareiva. “Synthesis and optical properties of Ce^{3+}–doped $Y_3Mg_2AlSi_2O_{12}$ phosphors”. *Journal of Luminescence* **129** (2009) 1356.
9. **A. Katelnikovas**, T. Bareika, P. Vitta, T. Jüstel, H. Winkler, A. Kareiva, A. Žukauskas, G. Tamulaitis. “$Y_{3-x}Mg_2AlSi_2O_{12}:Ce^{3+}{}_x$ phosphors – prospective for warm-white light emitting diodes”. *Optical Materials* **32** (2010) 1261.
10. S. Sakirzanovas, **A. Katelnikovas**, H. Bettentrup, A. Kareiva, T. Jüstel. “Synthesis and photoluminescence properties of Sm^{3+}–doped $LaMgB_5O_{10}$ and $GdMgB_5O_{10}$”. *Journal of Luminescence* **131** (2011) 1525.
11. **A. Katelnikovas**, J. Jurkevičius, K. Kazlauskas, P. Vitta, T. Jüstel, A. Kareiva, A. Žukauskas, G. Tamulaitis. “Efficient cerium-based sol-

gel derived phosphors in different garnet matrices for light-emitting diodes". *Journal of Alloys and Compounds* **509** (2011) 6247.

12. S. Sakirzanovas, **A. Katelnikovas**, D. Dutczak, A. Kareiva, T. Jüstel. "Synthesis and Sm^{2+}/Sm^{3+} doping effects on photoluminescence properties of $Sr_4Al_{14}O_{25}$". *Journal of Luminescence* **131** (2011) 2255.
13. **A. Katelnikovas**, H. Bettentrup, D. Dutczak, A. Kareiva, T. Jüstel. "On the correlation between the composition of Pr^{3+} doped garnet type materials and their photoluminescence properties". *Journal of Luminescence* **131** (2011) 2754.
14. S. Sakirzanovas, **A. Katelnikovas**, D. Dutczak, A. Kareiva, T. Jüstel. "Concentration influence on temperature-dependent luminescence properties of samarium substituted strontium tetraborate". *Journal of Luminescence* **132** (2012) 141.
15. D. Dutczak, A. Milbrat, **A. Katelnikovas**, A. Meijerink, C. Ronda, T. Jüstel. "Yellow persistent luminescence of $Sr_2SiO_4:Eu^{2+},Dy^{3+}$". *Journal of Luminescence* **132** (2012) 2398.

12.2.2. Attended Conferences

1. R. Skaudžius, S. Šakirzanovas, **A. Katelnikovas**, A. Beganskienė, A. Kareiva. "Spectroscopic evaluation and characterization of different mixed-metal garnets". *European seminar on infrared spectroscopy*. Lyon, France, April 4-6 (2006).
2. **A. Katelnikovas**, A. Kareiva. "Sol-gel chemistry approach to the preparation of nanocrystalline $CaWO_4$". *Inorganic Compounds: Synthesis, Properties and Application. Vilnius University Young Chemists Conference*. Vilnius, Lithuania, December 16-17 (2006) 9.
3. A. Stanulis, **A. Katelnikovas**, A. Beganskiene, D. Miksys. "Sol-gel derived antireflective coatings". *Inorganic Compounds: Synthesis, Properties and Application. Vilnius University Young Chemists Conference*. Vilnius, Lithuania, December 16-17 (2006) 21.

4. P. Vitta, T. Bareika, G. Tamulaitis, A. Žukauskas, **A. Katelnikovas**, A. Kareiva. “Photoluminescence analysis of sol-gel derived YAG:Ce phosphors”. *The 9th International Conference-School “Advanced Materials and Technologies*”. Palanga, Lithuania, August 27-31 (2007).
5. **A. Katelnikovas**, L. Vilčiauskas, L. Grigorjeva, D. Millers, V. Pankratov, A. Sternberg, A. Kareiva. “Sol-gel chemistry approach to the preparation of nanocrystalline $CaWO_4$”. *Advanced materials as studied by spectroscopic and diffraction techniques: specialized colloque AMPERE and Alexander von Humboldt workshop*. Vilnius, Lithuania, September 16-21 (2007).
6. **A. Katelnikovas**, H. Bettentrup, T. Jüstel. “Luminescence of Pr^{3+} doped $Lu_3Al_{5-x}Ga_xO_{12}$ garnet powders”. *8th Conference on Solid State Chemistry*. Bratislava, Slovak Republic, July 6-11 (2008) 86.
7. **A. Katelnikovas**, A. Kareiva, T. Jüstel. “Synthesis and optical properties of $Y_{3-x}Lu_xMg_2AlSi_2O_{12}$:$Ce^{3+}$”. *ECSSC XII – 12th European Conference on Solid State Chemistry*. Münster, Germany, September 20-23, (2009) 187.
8. A. Žalga, R. Sažinas, **A. Katelnikovas**, A. Selskis, J. Pinkas, A. Kareiva. “Influence of doping effect on the crystallization of $RE_2Mo_3O_{12}$ (RE = Gd, Eu) prepared by aqueous sol-gel citrate complex route”. *9th National Lithuanian Conference “CHEMIJA 2009*”. Vilnius, Lithuania, October 16, (2009) 51.
9. A. Žalga, **A. Katelnikovas**, A. Selskis, J. Pinkas, A. Kareiva. “Phase purity of Eu^{3+} and Ce^{4+} activated $MMo_xW_{1-x}O_4$ based (M = Ba, Ca) red – emitting phosphors”. *9th National Lithuanian Conference “CHEMIJA 2009*”. Vilnius, Lithuania, October 16, (2009) 52.
10. J. Jurkevicius, **A. Katelnikovas**, P. Vitta, A. Zukauskas, A. Kareiva, T. Jüstel, G. Tamulaitis. “Investigation of quantum efficiency of YMASG:Ce phosphor”. *The 12th International Conference “Advanced Materials and Technologies” and Summer School “European*

Doctorate in Physics and Chemistry of Advanced Materials". Palanga, Lithuania, August 27-31, (2010) 101.

11. **A. Katelnikovas**, H. Winkler, T. Jüstel. "Orange to red emitting (Ca,Sr,Ba)SiN_2:Eu^{2+} luminescent materials for phosphor converted LEDs". *ICLL-1 – First International Conference on Luminescence of Lanthanides*. Odessa, Ukraine, September 5-9, (2010) 63.
12. **A. Katelnikovas**, H. Bettentrup, A. Kareiva, T. Jüstel. "Pr^{3+} − The multitasking ion". *Phosphor Global Summit 2011*. San Antonio, Texas, USA, March 22-24, 2011.
13. **A. Katelnikovas**, A. Kareiva, H. Winkler, T. Jüstel. "On the PL efficiency and stability of (Ca,Sr,Ba)SiN_2:Eu^{2+} phosphors for solid state light sources". *ICL'11 – 16th International Conference on Luminescence*. Ann Arbor, Michigan, USA, June 26 - July 1, (2011) 60.
14. **A. Katelnikovas**, D. Dutczak, A. Kareiva, T. Jüstel. "A closer look at Pr^{3+} luminescence in garnets". *ICLA-2012 - 4th International Conference on Luminescence and its Applications*. Hyderabad, India, February 7-10, (2012) 42.
15. D. Jasaitis, A. Akelis, T. Jüstel, A. Kareiva, **A. Katelnikovas**, R. Skaudzius. "Matrix induced differences in luminescence properties of lanthanide-substituted mixed-metal L:$Y_3Al_{5-x}M_xO_{12}$ (M = In, Cr; L = Ce, Eu, Er, and Tb; $0.50 < x < 2.25$) garnets synthesized by sol-gel method". *10th CMCee – International Symposium on Ceramic Materials and Components for Energy and Environment Applications*. Dresden, Germany, May 20-23, (2012) 85.
16. S. Möller, **A. Katelnikovas**, D. Knaut, T. Jüstel. "Luminescence of Nd^{3+} in sensitized $Sr_2Si_5N_8$ powders". *REEC – 1st Rare Earth Elements and Compounds Conference*. Münster, Germany, September 4-6, (2012) 21.
17. F. Baur, **A. Katelnikovas**, H. Winkler, T. Jüstel. "A novel Eu^{2+} activated blue emitting silicate phosphor". *REEC – 1st Rare Earth*

Elements and Compounds Conference. Münster, Germany, September 4-6, (2012) 24.

12.2.3. Patents

1. H. Winkler, R. Petry, T. Vosgroene, T. Jüstel, D. Uhlich, **A. Katelnikovas**. "New compound of 1-1-2-alkaline earth silicon nitride type with europium-doping and additionally with co-dopants of e.g. manganese and magnesium, useful as a phosphor or a conversion phosphor". WO2010057572-A3
2. H. Winkler, R. Petry, T. Vosgroene, T. Jüstel, D. Uhlich, **A. Katelnikovas**. "New europium doped 6-3-6-4-alkaline earth-silicon oxynitride type compounds containing thorium, ruthenium, osmium, fluoride and/or chloride, as codopants, useful e.g. as conversion fluorescent material and for producing a molded body". WO2011006565-A1
3. H. Winkler, P. Barnekow, K. Kuehn, R. Petry, T. Vosgroene, T. Jüstel, D. Uhlich, **A. Katelnikovas**, D. Dutczak. "New europium-silicon-oxygen containing metallic compounds, useful as conversion luminescent substances for partial or complete conversion of blue or in near-UV emission of light emitting diode and in light source for lighting unit". WO2011091839-A1
4. H. Winkler, T. Jüstel, **A. Katelnikovas**, O. Darcanova. "New metal compound useful as a conversion luminescent material for partial or complete conversion of the blue or near-UV lying emission of a light emitting diode". WO2012034625-A1
5. H. Winkler, T. Jüstel, **A. Katelnikovas**, F. Baur. "Silicat-Leuchtstoff". EP application No. 12002867.5 (24th April 2012)

Chapter 13. References

[1] A. Žukauskas, M. Shur, R. Gaska, *Introduction to Solid-State Lighting*, J. Wiley, New York, 2002.

[2] V. Bachmann, *Studies on Luminescence and Quenching Mechanisms in Phosphors for Light Emitting Diodes*, Ph.D. Thesis, Utrech University, Utrecht, Netherlands, 2007.

[3] A. Katelnikovas, H. Winkler, T. Jüstel, *ICLL-1 – First International Conference on Luminescence of Lanthanides*, Odessa, Ukraine, September 5-9 (2010) 63.

[4] A. Katelnikovas, A. Kareiva, H. Winkler, T. Jüstel, *ICL'11 – 16th International Conference on Luminescence*, Ann Arbor, MI, USA, June 26 – July 1 (2011) 60.

[5] B. Johnstone, *Brilliant! Shuji Nakamura and the Revolution in Lighting Technology*, Prometheus Books, Amherst, 2007.

[6] J. Brox, *Brilliant! The Evolution of Artificial Light*, Houghton Mifflin Harcourt, Boston, 2010.

[7] T.A. Edison, U.S. patent No. 223,898 (1879).

[8] K.M. Conway, *1st Rare Earth Elements and Compounds Conference*, Münster, Germany, September 5-6 (2012) 8.

[9] R.N. Thayer, B.T. Barnes, *J. Opt. Soc. Am.* **29** (1939) 131-134.

[10] F. Meyer, H. Spanner, E. Germet, US 2 182 732 (1939).

[11] S. Nakamura, *Jpn. J. Appl. Phys.* **30** (1991) L1705-L1707.

[12] S. Nakamura, T. Mukai, M. Senoh, *Appl. Phys. Lett.* **64** (1994) 1687-1689.

[13] J.J. Wierer, D.A. Steigerwald, M.R. Krames, J.J. O'Shea, M.J. Ludowise, G. Christenson, Y.C. Shen, C. Lowery, P.S. Martin, S. Subramanya, W. Gotz, N.F. Gardner, R.S. Kern, S.A. Stockman, *Appl. Phys. Lett.* **78** (2001) 3379-3381.

[14] D.A. Zakheim, I.P. Smirnova, I.V. Roznanskii, S.A. Gurevich, M.M. Kulagina, E.M. Arakcheeva, G.A. Onushkin, A.L. Zakheim, E.D. Vasil'eva, G.V. Itkinson, *Semiconductors* **39** (2005) 851-855.

[15] N. Yukio, I. Masatsugu, S. Daisuke, S. Masahiko, M. Takashi, *J. Phys. D: Appl. Phys.* **43** (2010) 354002.

[16] G.O. Mueller, R. Mueller-Mach, *Proc. SPIE Int. Soc. Opt. Eng.* **4776** (2002) 122-130.

[17] R. Mueller-Mach, G.O. Mueller, M.R. Krames, *Proc. SPIE Int. Soc. Opt. Eng.* **5187** (2004) 115-122.

[18] S. Nakamura, G. Fasol, *The Blue Laser Diode: GaN Based Light Emitters and Lasers*, Springer, Berlin, 1997.

[19] T. Jüstel, S. Möller, H. Winkler, W. Adam, Luminescent Materials, in: *Ullmann's Encyclopedia of Industrial Chemistry*, Wiley-VCH Verlag GmbH & Co. KGaA, 2012, pp. 1-75.

[20] G. Blasse, A. Bril, *Appl. Phys. Lett.* **11** (1967) 53-55.

[21] H. Hirayama, Y. Tsukada, T. Maeda, N. Kamata, *Appl. Phys. Express* **3** (2010) 031002.

[22] H.X. Wang, H.D. Li, Y.B. Lee, H. Sato, K. Yamashita, T. Sugahara, S. Sakai, *J. Cryst. Growth* **264** (2004) 48-52.

[23] S.N. Lee, H.S. Paek, H. Kim, K.K. Kim, Y.H. Cho, T. Jang, Y. Park, *J. Cryst. Growth* **310** (2008) 3881-3883.

[24] Y. Liu, T. Egawa, H. Ishikawa, T. Jimbo, *J. Cryst. Growth* **259** (2003) 245-251.

[25] F.G. McIntosh, K.S. Boutros, J.C. Roberts, S.M. Bedair, E.L. Piner, N.A. El-Masry, *Appl. Phys. Lett.* **68** (1996) 40-42.

[26] B.K. Park, H.K. Park, J.H. Oh, J.R. Oh, Y.R. Do, *J. Electrochem. Soc.* **159** (2012) J96-J106.

[27] M. Kottaisamy, P. Thiyagarajan, J. Mishra, M.S. Ramachandra Rao, *Mater. Res. Bull.* **43** (2008) 1657-1663.

[28] S. Chang-yu, L. Ke, H. Qiang-long, F. Hua-jun, D. Xin-yong, *IEEE Photonics Technol. Lett.* **22** (2010) 884-886.

[29] Y. Uchida, T. Setomoto, T. Taguchi, Y. Nakagawa, K. Miyazaki, *SPIE* **4079** (2000) 120-126.

[30] P.F. Smet, A.B. Parmentier, D. Poelman, *J. Electrochem. Soc.* **158** (2011) R37-R54.

[31] S. Ye, F. Xiao, Y.X. Pan, Y.Y. Ma, Q.Y. Zhang, *Mater. Sci. Eng., R* **71** (2010) 1-34.

[32] C.R. Ronda, *Luminescence: from Theory to Applications*, Wiley-VCH, Weinheim, 2008.

[33] V. Bachmann, C. Ronda, O. Oeckler, W. Schnick, A. Meijerink, *Chem. Mater.* **21** (2009) 316-325.

[34] R. Yu, R. Luan, C. Wang, J. Chen, Z. Wang, B.K. Moon, J.H. Jeong, *J. Electrochem. Soc.* **159** (2012) J188-J192.

[35] M.A. Lim, J.K. Park, C.H. Kim, H.D. Park, M.W. Han, *J. Mater. Sci. Lett.* **22** (2003) 1351-1353.

[36] Y. Shimomura, T. Kurushima, M. Shigeiwa, N. Kijima, *J. Electrochem. Soc.* **155** (2008) J45-J49.

[37] R. Yu, J. Wang, J. Zhang, H. Yuan, Q. Su, *J. Solid State Chem.* **181** (2008) 658-663.

[38] A. Katelnikovas, J. Plewa, D. Dutczak, S. Möller, D. Enseling, H. Winkler, A. Kareiva, T. Jüstel, *Opt. Mater.* **34** (2012) 1195-1201.

[39] J.Y. Tang, J.H. Chen, L.Y. Hao, X. Xu, W.J. Xie, Q.X. Li, *J. Lumin.* **131** (2011) 1101-1106.

[40] Y.Q. Li, G. de With, H.T. Hintzen, *J. Alloys Compd.* **385** (2004) 1-11.

[41] R.J. Xie, N. Hirosaki, M. Mitomo, K. Uheda, T. Suehiro, X. Xu, Y. Yamamoto, T. Sekiguchi, *J. Phys. Chem. B* **109** (2005) 9490-9494.

[42] Y.Q. Li, C.M. Fang, G. de With, H.T. Hintzen, *J. Solid State Chem.* **177** (2004) 4687-4694.

[43] R. Yu, H. Li, H. Ma, C. Wang, H. Wang, B.K. Moon, J.H. Jeong, *J. Lumin.* **132** (2012) 2783-2787.

[44] A. Katelnikovas, H. Winkler, A. Kareiva, T. Jüstel, *Opt. Mater.* **33** (2011) 992-995.

[45] C.-C. Chiang, M.-S. Tsai, M.-H. Hon, *J. Electrochem. Soc.* **155** (2008) B517-B520.
[46] M.P. Saradhi, U.V. Varadaraju, *Chem. Mater.* **18** (2006) 5267-5272.
[47] X. Zhang, J. Zhang, Z. Dong, J. Shi, M. Gong, *J. Lumin.* **132** (2012) 914-918.
[48] J.K. Park, C.H. Kim, S.H. Park, H.D. Park, S.Y. Choi, *Appl. Phys. Lett.* **84** (2004) 1647-1649.
[49] X. Piao, K.-i. Machida, T. Horikawa, H. Hanzawa, *Appl. Phys. Lett.* **91** (2007) 041908.
[50] W. Bin Im, Y. Fourre, S. Brinkley, J. Sonoda, S. Nakamura, S.P. DenBaars, R. Seshadri, *Opt. Express* **17** (2009) 22673-22679.
[51] Y.Q. Li, N. Hirosaki, R.J. Xie, T. Takeda, M. Mitomo, *Chem. Mater.* **20** (2008) 6704-6714.
[52] J.A. Kechele, C. Hecht, O. Oeckler, J.S.A.D. Gunne, P.J. Schmidt, W. Schnick, *Chem. Mater.* **21** (2009) 1288-1295.
[53] A. Katelnikovas, H. Bettentrup, D. Uhlich, S. Sakirzanovas, T. Jüstel, A. Kareiva, *J. Lumin.* **129** (2009) 1356-1361.
[54] R.-J. Xie, N. Hirosaki, K. Sakuma, Y. Yamamoto, M. Mitomo, *Appl. Phys. Lett.* **84** (2004) 5404-5406.
[55] Y.Q. Li, J.E.J. van Steen, J.W.H. van Krevel, G. Botty, A.C.A. Delsing, F.J. DiSalvo, G. de With, H.T. Hintzen, *J. Alloys Compd.* **417** (2006) 273-279.
[56] D. Jia, X.-j. Wang, *Opt. Mater.* **30** (2007) 375-379.
[57] H. Watanabe, H. Yamane, N. Kijima, *J. Solid State Chem.* **181** (2008) 1848-1852.
[58] X.Q. Piao, T. Horikawa, H. Hanzawa, K. Machida, *Appl. Phys. Lett.* **88** (2006) 161908.
[59] C. Hecht, F. Stadler, P.J. Schmidt, J.S.A. der Guenne, V. Baumann, W. Schnick, *Chem. Mater.* **21** (2009) 1595-1601.
[60] X. Piao, K. Machida, T. Horikawa, H. Hanzawa, Y. Shimomura, N. Kijima, *Chem. Mater.* **19** (2007) 4592-4599.
[61] S. Adachi, H. Abe, R. Kasa, T. Arai, *J. Electrochem. Soc.* **159** (2012) J34-J37.
[62] Y. Arai, S. Adachi, *J. Lumin.* **131** (2011) 2652-2660.
[63] R. Kasa, S. Adachi, *J. Electrochem. Soc.* **159** (2012) J89-J95.
[64] Y. Arai, S. Adachi, *J. Electrochem. Soc.* **158** (2011) J179-J183.
[65] J.G. Wang, X.P. Jing, C.H. Yan, J.H. Lin, F.H. Liao, *J. Lumin.* **121** (2006) 57-61.
[66] G. Chongfeng, G. Fei, X. Yan, L. Lifang, G.S. Frank, Y. Bohan, *J. Phys. D: Appl. Phys.* **42** (2009) 095407.
[67] X. Qi, C.-M. Liu, C.-C. Kuo, *J. Alloys Compd.* **492** (2010) L61-L63.
[68] G. Ju, Y. Hu, H. Wu, Z. Yang, C. Fu, Z. Mu, F. Kang, *Opt. Mater.* **33** (2011) 1297-1301.
[69] L.Z. Yang, X.B. Yu, S.P. Yang, C.L. Zhou, P. Zhou, W.J. Gao, P. Ye, *Mater. Lett.* **62** (2008) 907-910.

[70] S. Sakirzanovas, A. Katelnikovas, D. Dutczak, A. Kareiva, T. Jüstel, *J. Lumin.* **132** (2012) 141-146.

[71] D. Uhlich, *Kristallographische und spektroskopische Untersuchungen an Eu3+-dotierten Molybdaten als potentielle Konverter für LEDs*, Ph.D. Thesis, Universität Osnabrück, Osnabrück, Germany, 2009.

[72] A. Katelnikovas, J. Plewa, S. Sakirzanovas, D. Dutczak, D. Enseling, F. Baur, H. Winkler, A. Kareiva, T. Jüstel, *J. Mater. Chem.* (2012) DOI: 10.1039/c1032jm34123a.

[73] J. Zhao, C. Guo, J. Yu, R. Yu, *Opt. Laser Technol.* (2012) DOI: 10.1016/j.optlastec.2012.1007.1032.

[74] Q. Zeng, P. He, X. Zhang, H. Liang, M. Gong, Q. Su, *Chem. Lett.* **38** (2009) 1172-1173.

[75] C.F. Guo, F. Gao, L.F. Liang, B.C. Choi, J.H. Jeong, *J. Alloys Compd.* **479** (2009) 607-612.

[76] J. Liao, H. You, D. Zhou, H.-r. Wen, R. Hong, *Opt. Mater.* **34** (2012) 1468-1472.

[77] Y.-S. Chang, Z.-R. Shi, Y.-Y. Tsai, S. Wu, H.-L. Chen, *Opt. Mater.* **33** (2011) 375-380.

[78] L.T. Francis, P.P. Rao, M. Thomas, S.K. Mahesh, V.R. Reshmi, V.D.S. Thampi, *Mater. Lett.* **81** (2012) 142-144.

[79] I.P. Roof, T.-C. Jagau, W.G. Zeier, M.D. Smith, H.-C. zur Loye, *Chem. Mater.* **21** (2009) 1955-1961.

[80] A. Zukauskas, R. Vaicekauskas, F. Ivanauskas, H. Vaitkevicius, M.S. Shur, *Appl. Phys. Lett.* **93** (2008) 051115.

[81] J.S. Kim, P.E. Jeon, Y.H. Park, J.C. Choi, H.L. Park, G.C. Kim, T.W. Kim, *Appl. Phys. Lett.* **85** (2004) 3696-3698.

[82] J.S. Kim, P.E. Jeon, J.C. Choi, H.L. Park, S.I. Mho, G.C. Kim, *Appl. Phys. Lett.* **84** (2004) 2931-2933.

[83] C.-K. Chang, T.-M. Chen, *Appl. Phys. Lett.* **90** (2007) 161901.

[84] S.H. Lee, J.H. Park, S.M. Son, J.S. Kim, H.L. Park, *Appl. Phys. Lett.* **89** (2006) 221916.

[85] B. Wang, L. Sun, H. Ju, S. Zhao, D. Deng, H. Wang, S. Xu, *Mater. Lett.* **63** (2009) 1329-1331.

[86] W.-J. Yang, L. Luo, T.-M. Chen, N.-S. Wang, *Chem. Mater.* **17** (2005) 3883-3888.

[87] F. Xiao, Y.N. Xue, Q.Y. Zhang, *Spectrochim. Acta, Part A* **74** (2009) 498-501.

[88] C.-H. Hsu, S. Das, C.-H. Lu, *J. Electrochem. Soc.* **159** (2012) J193-J199.

[89] C.-K. Chang, T.-M. Chen, *Appl. Phys. Lett.* **91** (2007) 081902.

[90] C. Guo, L. Luan, Y. Xu, F. Gao, L. Liang, *J. Electrochem. Soc.* **155** (2008) J310-J314.

[91] F. Xiao, Y.N. Xue, Y.Y. Ma, Q.Y. Zhang, *Physica B* **405** (2010) 891-895.

[92] F. Xiao, Y.N. Xue, Q.Y. Zhang, *Physica B* **404** (2009) 3743-3747.

[93] C. Guo, L. Luan, F.G. Shi, X. Ding, *J. Electrochem. Soc.* **156** (2009) J125-J128.

[94] Y. Song, G. Jia, M. Yang, Y. Huang, H. You, H. Zhang, *Appl. Phys. Lett.* **94** (2009) 091902.
[95] W.-J. Yang, T.-M. Chen, *Appl. Phys. Lett.* **88** (2006) 101903.
[96] H. Jiao, Y. Wang, *J. Electrochem. Soc.* **156** (2009) J117-J120.
[97] W.-R. Liu, Y.-C. Chiu, Y.-T. Yeh, S.-M. Jang, T.-M. Chen, *J. Electrochem. Soc.* **156** (2009) J165-J169.
[98] C.-H. Huang, T.-M. Chen, W.-R. Liu, Y.-C. Chiu, Y.-T. Yeh, S.-M. Jang, *ACS Appl. Mater. Interfaces* **2** (2010) 259-264.
[99] T.-G. Kim, Y.S. Kim, S.-J. Im, *J. Electrochem. Soc.* **156** (2009) J203-J207.
[100] N. Guo, Y.H. Zheng, Y.C. Jia, H. Qiao, H.P. You, *New J. Chem.* **36** (2012) 168-172.
[101] W. Lü, Y. Luo, Z. Hao, X. Zhang, X. Wang, J. Zhang, *Mater. Lett.* **77** (2012) 45-47.
[102] C.F. Guo, X. Ding, L. Luan, Y. Xu, *Sens. Actuators, B* **143** (2010) 712-715.
[103] P. Li, Z. Wang, Z. Yang, Q. Guo, *J. Electrochem. Soc.* **157** (2010) H504-H509.
[104] S. Cotton, *Lanthanide and Actinide Chemistry*, Wiley, Chichester, 2006.
[105] F. Szabadvary, Chapter 73. The History of the Discovery and Separation of the Rare Earths, in: K.A. Gschneidner, L. Eyring (Eds.) *Handbook on the Physics and Chemistry of Rare Earths*, Elsevier Science Publishers B.V., Amsterdam, 1988, pp. 33-80.
[106] H.G. Friedman, G.R. Choppin, D.G. Feuerbacher, *J. Chem. Educ.* **41** (1964) 354.
[107] J.E. Huheey, E.A. Keiter, R.L. Keiter, *Inorganic Chemistry: Principles of Structure and Reactivity*, 4th ed., Harper Collins College Publishers, New York, 1993.
[108] P. Peijzel, *Probing High Energy Levels of Lanthanide Ions*, Ph.D. Thesis, University of Utrecht, Utrecht, The Netherlands, 2004.
[109] D. Uhlich, *1st Rare Earth Elements and Compounds Conference*, Münster, Germany, September 5-6 (2012) 16.
[110] J.-C. Bünzli, *1st Rare Earth Elements and Compounds Conference*, Münster, Germany, September 5-6 (2012) 7.
[111] D. Dutczak, *1st Rare Earth Elements and Compounds Conference*, Münster, Germany, (2012) 9.
[112] M. Haase, *1st Rare Earth Elements and Compounds Conference* Münster, Germany, (2012) 10.
[113] A.A. Kaminskiĭ, *Laser Crystals: Their Physics and Properties*, 2nd ed., Springer-Verlag, Berlin, 1990.
[114] A.A. Kaminskii, *Laser Photonics Rev.* **1** (2007) 93-177.
[115] M.J. Weber, *Rare Earth Lasers*, North-Holland Publishing Company, Amsterdam, 1979.
[116] J.M. Ogieglo, *Luminescence and Energy Transfer in Garnet Scintillators* Ph.D. Thesis, University of Utrecht, Utrecht, The Netherlands, 2012.

[117] J.-C.G. Bünzli, S.V. Eliseeva, Basics of Lanthanide Photophysics, in: P. Hänninen, H. Härmä (Eds.) *Lanthanide Luminescence: Photophysical, Analytical and Biological Aspects*, Springer-Verlag Berlin Heidelberg, 2011, pp. 1-45.

[118] J.P. Lowe, K.A. Peterson, *Quantum Chemistry*, 3rd ed., Elsevier Academic Press, Burlington, 2006.

[119] W.M. Yen, S. Shionoya, H. Yamamoto, *Fundamentals of Phosphors*, CRC Press, Boca Raton, 2007.

[120] S. Sakirzanovas, *Novel Sm2+/3+ Phosphors as Luminescence Converter for Near UV Radiation*, Ph.D. Thesis, Vilnius University, Vilnius, Lithuania, 2011.

[121] R.B. Leighton, *Principles of Modern Physics*, McGraw-Hill, New York, 1959.

[122] B.M. Walsh, *Judd-Ofelt Theory: Principles and Practices*, Springer, Dordrecht, 2006.

[123] N. Sabbatini, M. Guardigli, J.-M. Lehn, *Coord. Chem. Rev.* **123** (1993) 201-228.

[124] J. Collins, *Luminescence Spectroscopy of Solids: Localized Systems*, Springer, Dordrecht, 2006.

[125] W.T. Carnall, Chapter 24. The Absorption and Fluorescence Spectra of Rare Earth Ions is Solution, in: K.A. Gschneidner, L. Eyring (Eds.) *Handbook on the Physics and Chemistry of Rare Earths*, North-Holland Publishing Company, Amsterdam, 1979, pp. 171-208.

[126] E. Boulma, M. Diaf, J.P. Jouart, M. Bouffard, J.L. Doualan, R. Moncorgé, *J. Phys.: Condens. Matter* **18** (2006) 6721.

[127] N. Grote, H. Venghaus, *Fibre Optic Communication Devices*, Springer, Berlin, 2001.

[128] B.G. Wybourne, L. Smentek, *Optical Spectroscopy of Lanthanides: Magnetic and Hyperfine Interactions*, CRC Press, Boca Raton, 2007.

[129] S.V. Eliseeva, J.-C.G. Bunzli, *Chem. Soc. Rev.* **39** (2010) 189-227.

[130] W.A. Runciman, *Philos. Mag.* **1** (1956) 1075-1077.

[131] W. Demtröder, *Atoms, Molecules and Photons: an Introduction to Atomic-, Molecular- and Quantum-Physics*, 2nd ed., Springer, Heidelberg, 2010.

[132] J. García Solé, L.E. Bausá, D. Jaque, *An Introduction to the Optical Spectroscopy of Inorganic Solids*, J. Wiley, Hoboken, 2005.

[133] C. Görller-Walrand, K. Binnemans, Chapter 167. Spectral Intensities of f-f Transitions, in: K.A. Gschneidner, L. Eyring (Eds.) *Handbook on the Physics and Chemistry of Rare Earths*, Elsevier Science B.V., Amsterdam, 1998, pp. 101-264.

[134] D.M. Gruen, C.W. DeKock, *J. Chem. Phys.* **45** (1966) 455-460.

[135] M. Gruen D, W. DeKock C, L. McBeth R, Chapter 8. Electronic Spectra of Lanthanide Compounds in the Vapor Phase, in: P.R. Fields, T. Moeller (Eds.) *Lanthanide/Actinide Chemistry*, American Chemical Society, 1967, pp. 102-121.

[136] C.K. Jørgensen, B.R. Judd, *Mol. Phys.* **8** (1964) 281-290.

[137] G. Blasse, B.C. Grabmaier, *Luminescent Materials*, Springer-Verlag, Berlin, 1994.

[138] G.G. Stokes, *Phil. Trans. R. Soc. London* **142** (1852) 463-562.

[139] J.R. Lakowicz, *Principles of Fluorescence Spectroscopy*, 3rd ed., Springer, New York, 2006.

[140] H. Bechtel, T. Jüstel, H. Gläser, D.U. Wiechert, *J. Soc. Inf. Display* **10** (2002) 63-67.

[141] A.K. Levine, F.C. Palilla, *Appl. Phys. Lett.* **5** (1964) 118-120.

[142] A.M. Srivastava, T.J. Sommerer, *Electrochem. Soc. Interface* **7** (1998) 28-31.

[143] H. Bettentrup, *Untersuchung der Lumineszenzeigenschaften Eu3+ und Sm3+ aktivierter Wolframatverbindungen*, Ph.D. Thesis, Universität Osnabrück, Osnabrück, Germany, 2009.

[144] ISO 21348:2007(E), *Space Environment (Natural and Artificial) — Process for Determining Solar Irradiances*, 2007, 1-20.

[145] D. Dutczak, A. Milbrat, A. Katelnikovas, A. Meijerink, C. Ronda, T. Justel, *J. Lumin.* **132** (2012) 2398-2403.

[146] B.P. Anthony, F.S. Philippe, B. Frank, C. Jürgen, P. Dirk, *J. Phys. D: Appl. Phys.* **43** (2010) 085401.

[147] H. Yu, D.G. Deng, S.Q. Xu, C.P. Yu, H.Y. Yin, Q.L. Nie, *J. Lumin.* **132** (2012) 2553-2556.

[148] R.-J. Xie, Y.Q. Li, N. Hirosaki, H. Yamamoto, *Nitride Phosphors and Solid-State Lighting*, CRC/Taylor & Francis, Boca Raton, 2011.

[149] L.G. van Uitert, *J. Lumin.* **29** (1984) 1-9.

[150] V.N. Makhov, M. Kirm, G. Stryganyuk, S. Vielhauer, G. Zimmerer, B.Z. Malkin, O.V. Solovyev, S.L. Korableva, *J. Lumin.* **132** (2012) 418-424.

[151] M.S. Kishore, N.P. Kumar, R.G. Chandran, A.A. Setlur, *Electrochem. Solid-State Lett.* **13** (2010) J77-J80.

[152] J. Ziqiang, W. Yuhua, W. Linshui, *J. Electrochem. Soc.* **157** (2010) J155-J158.

[153] M.C. Maniquiz, K.Y. Jung, S.M. Jeong, *J. Electrochem. Soc.* **157** (2010) H1135-H1139.

[154] M. Maniquiz, K.Y. Jung, *ECS Trans.* **28** (2010) 175-182.

[155] A.A. Setlur, W.J. Heward, Y. Gao, A.M. Srivastava, R.G. Chandran, M.V. Shankar, *Chem. Mater.* **18** (2006) 3314-3322.

[156] C.K. Jørgensen, Vol. 22. Partly Filled Shells Constituting Anti-bonding Orbitals with Higher Ionization Energy than Their Bonding Counterparts Rare Earths, in: J.D. Dunitz, P. Hemmerich, R.H. Holm, J.A. Ibers, C.K. Jørgensen, J.B. Neilands, D. Reinen, R.P.J. Williams (Eds.) *Structure & Bonding*, Springer-Verlag, New York, 1975, pp. 49-81.

[157] R. Masse, A. Durif, *C. R. Seances Acad. Sci. (Ser. C)* **276** (1973) 1029-1031.

[158] R.D. Shannon, *Acta Crystallogr.* **A32** (1976) 751-767.

[159] R.F. Klevtsova, A.D. Vasiliev, L.A. Glinskaya, A.I. Kruglik, N.M. Kozhevnikova, V.P. Korsun, *Zh. Strukt. Khim.* **33** (1992) 126-130.

[160] G. Menzer, *Z. Kristallogr.* **63** (1926) 157-158.

[161] A. Beltran, J. Andres, J.A. Igualada, J. Carda, *J. Phys. Chem.* **99** (1995) 6493-6501.

[162] A.F. Wells, *Structural Inorganic Chemistry*, 4th ed., Oxford University Press, London, 1975.

[163] A. Katelnikovas, H. Bettentrup, D. Dutczak, A. Kareiva, T. Jüstel, *J. Lumin.* **131** (2011) 2754-2761.

[164] R.C. Ropp, *Luminescence and the Solid State*, 2nd ed., Elsevier, Amsterdam, 2004.

[165] J. Aguiar, P. Carpena, J.A. Molina-Bolívar, C. Carnero Ruiz, *J. Colloid Interface Sci.* **258** (2003) 116-122.

[166] A.R. West, *Solid State Chemistry and its Applications*, John Wiley & Sons, Chichester, 1984.

[167] V. Tomkute, A. Katelnikovas, H. Bettentrup, A. Kareiva, T. Jüstel, *Opt. Mater.* **33** (2011) 1272-1277.

[168] W.J. Schipper, J.J. Piet, H.J. de Jager, G. Blasse, *Mater. Res. Bull.* **29** (1994) 23-30.

[169] S.H.M. Poort, A. Meyerink, G. Blasse, *J. Phys. Chem. Solids* **58** (1997) 1451-1456.

[170] A. Einstein, *Phys.Z.* **18** (1917) 121.

[171] W.M. Yen, S. Shionoya, H. Yamamoto, *Phosphor handbook*, 2nd ed., CRC Press/Taylor and Francis, Boca Raton, 2007.

[172] M. Zeuner, F. Hintze, W. Schnick, *Chem. Mater.* **21** (2009) 336-342.

[173] P. Pasierb, R. Gajerski, M. Rokita, M. Rekas, *Physica B* **304** (2001) 463-476.

[174] M.J. Song, L.T. Wang, M.L. Zhao, L.Z. Zhang, G.F. Wang, *Opt. Mater.* **33** (2010) 36-41.

[175] U. Schubert, N. Hüsing, *Synthesis of Inorganic Materials*, 2nd ed., Wiley-VCH, Weinheim, 2005.

[176] C.N.R. Rao, A. Müller, A.K. Cheetham, *The Chemistry of Nanomaterials: Synthesis, Properties and Applications*, Wiley-VCH, Weinheim, 2004.

[177] M.J. Song, W. Zhao, G.F. Wang, M.L. Zhao, L.T. Wang, *J. Alloys Compd.* **509** (2011) 2164-2169.

[178] Y.C. Chang, C.H. Liang, S.A. Yan, Y.S. Chang, *J. Phys. Chem. C* **114** (2010) 3645-3652.

[179] J.Y. Cho, Y.R. Do, Y.D. Huh, *Appl. Phys. Lett.* **89** (2006) 131915.

[180] L.H. Yi, X.P. He, L.L. Zhou, F.Z. Gong, R.F. Wang, J.H. Sun, *J. Lumin.* **130** (2010) 1113-1117.

[181] G.H. Lee, S. Kang, *J. Lumin.* **131** (2011) 2606-2611.

[182] E.Y. Lee, Y.J. Kim, *J. Kor. Electrochem. Soc.* **12** (2009) 234-238.

[183] W.T. Carnall, H. Crosswhite, H.M. Crosswhite, *Argonne National Laboratory Report* (1977) Unnumbered.

[184] A. Dulda, D.S. Jo, L.S. Pu, T. Masaki, D.H. Yoon, *J. Ceram. Soc. Jpn.* **118** (2010) 568-570.

[185] B.-S. Tsai, Y.-H. Chang, Y.-C. Chen, *Electrochem. Solid-State Lett.* **8** (2005) H55-H57.

[186] C.-H. Liang, Y.-C. Chang, Y.-S. Chang, *J. Electrochem. Soc.* **156** (2009) J303-J307.

[187] N. Rakov, F.E. Ramos, G. Hirata, M. Xiao, *Appl. Phys. Lett.* **83** (2003) 272-274.

[188] C.H. Liang, Y.C. Chang, Y.S. Chang, *Appl. Phys. Lett.* **93** (2008) 211902.

[189] A. Bril, H.A. Klassens, *Philips Res. Rept.* **10** (1955).

[190] P. Melnikov, V.A. Nascimento, L.Z.Z. Consolo, A.F. Silva, *J. Therm. Anal. Calorim.* (2012).

[191] R. Ianoş, I. Lazău, C. Păcurariu, *J. Mater. Sci.* **44** (2009) 1016-1023.

[192] A. Katelnikovas, J. Ogiegło, H. Winkler, A. Kareiva, T. Jüstel, *J. Sol-Gel Sci. Technol.* **59** (2011) 311-314.

[193] A. Katelnikovas, T. Bareika, P. Vitta, T. Jüstel, H. Winkler, A. Kareiva, A. Zukauskas, G. Tamulaitis, *Opt. Mater.* **32** (2010) 1261-1265.

[194] V. Bachmann, C. Ronda, A. Meijerink, *Chem. Mater.* **21** (2009) 2077-2084.

[195] A.A. Setlur, A.M. Srivastava, *Opt. Mater.* **29** (2007) 1647-1652.

[196] R.D. Shannon, C.T. Prewitt, *Acta Crystallogr.* **B25** (1969) 925-946.

[197] K. Blazek, A. Krasnikov, K. Nejezchleb, M. Nikl, T. Savikhina, S. Zazubovich, *Phys. Status Solidi B* **241** (2004) 1134-1140.

[198] V. Babin, V.V. Laguta, A. Makhov, K. Nejezchleb, M. Nikl, S. Zazubovich, *IEEE Trans. Nucl. Sci.* **55** (2008) 1156-1159.

[199] N.Y. Konstantinov, L.G. Karaseva, V.V. Gromov, A.V. Yakovlev, *Phys. Status Solidi A* **83** (1984) K153-K157.

Acknowledgements

Finally, I came to the part where I can say thanks to a number of people who helped me throughout this long scientific journey.

First of all I would like to thank my supervisors Prof. Aivaras Kareiva and Prof. Thomas Jüstel who answered endless amount of questions, taught me a lot on the synthesis, luminescence and so many more things during the period of this thesis.

I am also grateful to Merck company for financial support.

I am thankful to TOM group at Münster University of Applied Sciences for creating wonderful working atmosphere and various help with spectrometers and other equipment. So, Helga, Beni, Dominik, Linda, Andre, David, Sebastian, Thomas, Florian, Matthias, Viktoria, Claudia, Christian, Tobias thanks a lot for that again.

My separate thanks go to Stephanie Möller, who always helped me whether it was some crazy math stuff, broken car or something else.

I am thankful to Dr. Julian Plewa for TG/DTA measurements, Dr. Simas Sakirzanovas and PhD student Martynas Misevičius for taking SEM pictures and performing XRD analysis for some of my samples.

I would also like to say thanks to Olga Darčanova, Skirmantė Butkutė, Viktorija Tomkutė, Audronė Jankevičiūtė, Kristina Klemkaitė-Ramanauskė Andrius Stanulis, Danas Sakalauskas and other members of “Sol-Gel Chemistry Group” at Vilnius University. I felt always welcome there whenever I was visiting them.

During my stay in Steinfurt I was always surrounded by a bunch of great people from Poland, who made me feel like at home and pulled me out from the lab every now and then. Ewelina, Michal, Joanna O., Wojciech, Joanna M., Beata, Anna, Gosia, Kasia, Grzegorz, Krzysztof and others thanks a lot for the great time, wonderful parties and help when necessary.

I would also like say thanks to the colleagues from Physics Department of Vilnius University for collaboration in writing several papers.

I am grateful to my dear friends Dana and Szymon for all the time spent together, laughter, trips to amusement parks and for many more things we did together.

I would also like to thank my wonderful friends Aušra and Julija, who were always interested in the things that were happening in my life during this long and complex period.

Whenever I needed the place to sleep in Vilnius I was always welcome in the place of my good friends Julius, Vilma, Evaldas and Ingrida. I am very grateful for that, and also for all the fishing trips and the other funny things we did together.

Last but not least the most special thanks go to my family, who always supported me in good and bad times. I cannot express my thanks and loves for them in words. *Ačiū Jums už visą paramą ir meilę.*